Modelling and Prediction of Tire-Rim Slip with Finite Element Analysis

by

William Collings

A thesis submitted to the
School of Graduate and Postdoctoral Studies in partial
fulfillment of the requirements for the degree of

Master of Applied Science in Automotive Engineering

Department of Automotive and Mechatronics Engineering

Faculty of Engineering and Applied Science

University of Ontario Institute of Technology (Ontario Tech University)

Oshawa, Ontario, Canada

July 2023

Thesis Examination Information

Submitted by: **William Collings**

Master of Applied Science in **Automotive Engineering**

Thesis title: Modelling and Prediction of Tire-Rim Slip with Finite Element Analysis

An oral defense of this thesis took place on July 11, 2023 in front of the following examining committee:

Examining Committee:

Chair of Examining Committee	Dr. Amirkianoosh Kiani
Research Supervisor	Dr. Moustafa El-Gindy
Research Co-supervisor	Dr. Jing Ren
Examining Committee Member	Dr. Zeinab El-Sayegh
Thesis Examiner	Dr. Jaho Seo, Ontario Tech University

The above committee determined that the thesis is acceptable in form and content and that a satisfactory knowledge of the field covered by the thesis was demonstrated by the candidate during an oral examination. A signed copy of the Certificate of Approval is available from the School of Graduate and Postdoctoral Studies.

Abstract

In this thesis, tire-rim slip was simulated with a FEA model of a RHD truck tire. Multiple simulations were conducted to validate the model and investigate the effects of different parameters such as terrain type, tire-rim friction coefficient, drawbar load, vertical load, inflation pressure, and longitudinal wheel speed. Two terrain types were used: a high-friction hard surface and a soft SPH soil calibrated to represent upland sandy loam. An additional step was the design and training of a neural network-based virtual sensor for the prediction of tire-rim slip based on the parameters with significant effects. Two important findings were that tire-rim slip was higher on the soft soil than on the hard surface, and that the longitudinal wheel speed had negligible effect. Finally, a neural network with 31 neurons was trained using Bayesian regularization to predict the tire-rim slip with a correlation coefficient of 0.99431.

Keywords: FEA; tire-rim slip; terramechanics; virtual sensor; neural network

Author's Declaration

I hereby declare that this thesis consists of original work of which I have authored. This is a true copy of the thesis, including any required final revisions, as accepted by my examiners.

I authorize the University of Ontario Institute of Technology (Ontario Tech University) to lend this thesis to other institutions or individuals for the purpose of scholarly research. I further authorize University of Ontario Institute of Technology (Ontario Tech University) to reproduce this thesis by photocopying or by other means, in total or in part, at the request of other institutions or individuals for the purpose of scholarly research. I understand that my thesis will be made electronically available to the public.

WILLIAM COLLINGS

Statement of Contributions

The work described in Chapter 2 will be submitted as:

W. Collings, Z. El-Sayegh, J. Ren, and M. El-Gindy, “Literature survey for the development of a virtual tire-rim slip sensor," *Int. J. Vehicle Systems Modelling and Testing*, 2023.

Part of the work described in Chapters 3 and 5 has been published as:

W. Collings, Z. El-Sayegh, J. Ren, and M. El-Gindy, "Modelling of off-road truck tire-rim slip using finite element analysis," *SAE Int. J. Adv. & Curr. Prac. in Mobility*, vol. 4, no. 6, pp. 2335-2341, 2022, https://doi.org/10.4271/2022-01-0882. All content from this publication [107] has been reprinted with permission. © SAE International.

Part of the work described in Chapters 4 and 5 has been presented as:

W. Collings, Z. El-Sayegh, J. Ren, and M. El-Gindy, "Modelling of FEA truck tire-rim slip on SPH sandy loam," presented at the ISTVS Americas Symposium, Oct. 5-7, 2022, Montréal, Québec, Canada.

I performed the majority of the research and writing for these publications and presentation.

Acknowledgements

I am extremely grateful to all of my friends, family, colleagues, and supervisors who have supported me throughout the years of working on my thesis. My name appears alone on it as the author, but it was certainly not something that was done alone. Special thanks to my wonderful and wise supervisors and teachers, Dr. Moustafa El-Gindy, Dr. Jing Ren, and also Dr. Zeinab El-Sayegh. They introduced me to the fascinating world of modern tire research, and offered much guidance and support as I wrote papers, attended conferences, solved problems, did research, and learned new things. My thesis wouldn't be half as good without them.

Thanks also to the engineers at Volvo Group Trucks Technology and the NSERC Discovery Grant for partially funding this research. In addition, I greatly appreciate the conversations and advice shared with my fellow graduate students. You made my work a joy rather than a chore. You know who you are. Thanks to my family and other friends for always encouraging me and providing for me throughout the many hours of intense work that was my first graduate degree. Last, but not least, thanks to my God and Saviour for giving me the strength and wisdom to do all this work. I hope it will not be in vain, but instead a way to give back to everyone who has helped me finish my thesis.

Table of Contents

List of Figures

CHAPTER 2

CHAPTER 3

CHAPTER 4

CHAPTER 5

CHAPTER 6

List of Tables

List of Abbreviations and Symbols

Abbreviation	Description
ASTM	American Society for Testing and Materials
BR	Bayesian Regularization
COG	Center of Gravity
CNN	Convolutional Neural Network
DBN	Deep Belief Network
DEM	Discrete Element Method
DNN	Deep Neural Network
FEA	Finite Element Analysis
KF	Kalman Filter
L-M	Levenberg-Marquadt
LO	Linear or Luenberger Observer
LSTM	Long Short-Term Memory
MSE	Mean-Squared Error
MSW	Mean-Squared Weights
NLO	Non-Linear Observer
RHD	Regional Haul Drive
RLS	Recursive Least Squares
RNN	Recurrent Neural Network
SMO	Sliding Mode Observer
SPH	Smoothed Particle Hydrodynamics

Symbol	Unit	Description
α	degrees	Tire slip angle
β	degrees	Vehicle sideslip angle
γ	kN/m^3	Soil bulk unit weight
θ_{rim}	radians	Angle of rim rotation
θ_{tire}	radians	Angle of tire rotation
λ	none	BR training function parameter
μ	none	Tire-rim friction coefficient
ρ	g/cm^3	Density of SPH material
σ_y	MPa	Yield strength of SPH material
τ_{max}	kPa	Maximum soil shear stress
ϕ	degrees	Soil friction angle
ω_{drum}	rad/s	Angular velocity of drum in drum-cleat test
ω_{rim}	rad/s	Angular velocity of rim
ω_{tire}	rad/s	Angular velocity of tire
A_{cont}	m^2	Tire-rim contact area
b	m	Size of plate in pressure-sinkage equation
c	kPa	Soil cohesion

C_1	MPa	Bulk modulus of SPH material
C_{10}, C_{01}	MPa	Mooney-Rivlin equation coefficients
D_i	m^2/MN	Strain energy material parameter
E_t	MPa	Elastic modulus of SPH material
ETA	none	Anti-crossing force parameter
F_D	%	Drawbar load
F_x	kN	Contact patch longitudinal force, tire frame
F_X	kN	Contact patch longitudinal force, global frame
F_y	kN	Contact patch lateral or cornering force, tire frame
F_Y	kN	Contact patch lateral or cornering force, global frame
F_z	kN	Contact patch vertical force or tire vertical load
G	MPa	Shear modulus of SPH material
h	mm	Smoothing length for SPH particle
h_{cont}	mm	Contact thickness
$Hmax$	none	Maximum smoothing length ratio
$Hmin$	none	Minimum smoothing length ratio
I_1, I_2	none	First and second deviatoric strain invariants
i_{rim}	%	Rim-slip, relative rate of angular tire-rim slip
J^{el}	none	Elastic volume ratio
k_c	kN/m^{n+1}	Pressure-sinkage equation parameter
k_ϕ	kN/m^{n+2}	Pressure-sinkage equation parameter
n	none	Pressure-sinkage equation exponent
p_{inf}	kPa	Tire inflation pressure
p_{cont}	kPa	Tire-rim contact pressure
p_{soil}	kPa	Normal pressure applied to soil
r	m	Radial distance from tire center
r_0	m	Nominal tire radius
r_{roll}	m	Rolling tire radius
R	none	Pearson's correlation coefficient
R^2	none	Statistical goodness of curve fit metric
$RATIO$	none	Ratio of particle smoothing length to radius
T	kNm	Tire drive torque
T_f	kNm	Frictional torque between tire and rim
U	J	Strain energy
V_x	km/h	Longitudinal wheel speed
w_i	none	Weights for neural network connections
z	m	Soil sinkage

Chapter 1. Introduction

1.1 Motivation

The tire is an important area of research in automotive engineering, since the tire is the main point of contact between the vehicle and the ground. The complex construction and nonlinearity of modern radial tires means that it is also a challenging area of research, but this has been partially mitigated by the development of advanced finite element analysis (FEA) techniques and associated improvements in computer processing capabilities.

Previous FEA-based tire research has focused on topics such as cornering forces, rolling resistance, tire-terrain interaction, thermal properties, vibration and internal stresses [1]-[6]. One topic on which less research has been done is the tire-rim interface [7], [8]. However, it is still an important topic since the small contact area between the tire and rim is responsible for reliably transmitting forces and torques between the tire and rim during all operating conditions, in order to allow the tire-wheel system to function as intended. This shortage of tire-rim research created an opportunity for increasing the amount of knowledge of tire-rim behavior available in the literature. Therefore, this thesis was done on a tire-rim related topic, namely the modelling and prediction of tire-rim slip using FEA.

Tire-rim slip is generally defined as relative rotational motion between the tire and rim. The presence of tire-rim slip is detrimental to tire operation as it reduces the efficiency of the power transfer between the rim and tire, and can also lead to unwanted wheel vibration, as noted by several manufacturers [9], [10]. Therefore, it is in the interest of tire and rim manufacturers to understand which operating conditions lead to undesirable tire-rim slip, and which do not. Since many of the operating conditions which theoretically lead to tire-rim slip, such as high drive torques and low tire pressures, typically occur in off-road driving conditions, both hard surface and soft soil terrains were included in the investigation.

Furthermore, there has been much recent advancement in the areas of smart tires, vehicle state estimation, and virtual vehicle modelling and prediction for autonomous

control [11]-[13]. Hence, it was reasonable to use the data collected on tire-rim slip and vehicle operating conditions to develop a prototype virtual sensor for predicting tire-rim slip using advanced computer learning methods. Such a sensor could be further developed in the future, and integrated into an advanced predictive control system for an entire vehicle. These considerations of past, present, and future research were the foundation for the objectives laid out next.

1.2 Objectives

The main objective of this thesis was to investigate the operating conditions causing tire-rim slip using an FEA model, and then predict tire-rim slip with a neural network, for the particular case of a regional haul drive (RHD) truck tire on both a hard surface and a soft soil. This main objective was broken down into several intermediate objectives:

1. Modify an existing RHD truck tire FEA model in order to allow for the simulation of tire-rim slip.
2. Calibrate a smoothed-particle hydrodynamics (SPH) soil model for a new type of soft soil.
3. Investigate the effects of different operating conditions and terrains on tire-rim slip to determine which parameters are significant, what their effects are, and the underlying mechanisms.
4. Design and train a simple neural network-based virtual sensor to predict the tire-rim slip based on the parameters found to have a significant effect.

1.3 Thesis Outline

To achieve these objectives, the remainder of the thesis will be organized into Chapters 2-7 as follows:

Chapter 2 – Literature Review: A summary of past and present efforts on analytical and numerical tire models, modelling and studying of the tire-rim interface, modelling and calibration of FEA soils, and virtual sensor design for automotive applications, including neural networks.

Chapter 3 – Tire-Rim Slip Modelling and Validation: A description of the FEA truck tire model construction and modification, method for simulating tire-rim slip, validation against the previous FEA truck tire model and manufacturer data, and frictional torque estimation.

Chapter 4 – Soil Modelling: A description of the SPH soil model, determination of soil and model characteristics, and the soil calibration process.

Chapter 5 – Tire-Rim Slip Results and Analysis: A summary of the effects of different operating conditions such as tire-rim friction, drawbar load, inflation pressure, vertical load, and longitudinal wheel speed on the tire-rim slip, and a comparison of those effects for both hard surface and soft soil terrains.

Chapter 6 – Tire-Rim Slip Prediction: A description of the architecture of the neural network designed for predicting tire-rim slip, the data collection and training process, and an evaluation of the performance and applications of the developed neural network.

Chapter 7 – Conclusions and Future Work: A summary of the major results, contributions, and limitations of this thesis, as well as potential applications and directions for future research based on this work.

Chapter 2. Literature Review

2.1 Introduction

Over the past 50 years, research efforts into the characteristics and performance of tires have been continually expanding, utilizing advanced experimental and analytical tools in order to improve our understanding of tire behaviour and enable better tire designs. A more recent trend is the application of artificial intelligence techniques such as neural networks and virtual sensing to different parts of the tire industry. This literature survey will cover diverse topics including tire modelling, the tire-rim interaction, tire-terrain modelling or terramechanics, and virtual sensing, with the goal of laying the ground work for modelling and predicting tire-rim slip on different terrains using virtual sensors.

2.2 Tire Modelling

Tire modelling is a very active field of automotive research. Multiple different types of models have been developed including analytical, empirical, numerical, and various combinations of these. Some specific examples include the Magic Formula model, the string model, the rigid ring model, the brush model, and the shell model [14]-[16]. With the rapid increase in computing capability in recent times, numerical or finite element analysis (FEA) models have become prevalent due to the high degree of accuracy they can provide [5], [17]-[21]. The type of tire model chosen depends on the research purpose, such as representation of frictional effects [22], vibration analysis [5], [23], [24], tire-terrain interaction [2], [3], crash simulations [17], [19], impact tests [25], or large multibody simulations [26]. This section will first review the tire dynamics involved in modelling, and then describe some trends and examples of analytical, FEA, and rubber models.

2.2.1 Tire Dynamics

A tire is a complex physical structure designed to transmit forces and moments from the ground to the rim, and ultimately to the wheel hub. These forces and moments then influence the motion and acceleration of the entire vehicle, which means that having a good tire model is critical for having a good model of vehicle dynamics.

Standardized methods have been developed to describe these forces and moments, such as the system shown in Figure 2.1.

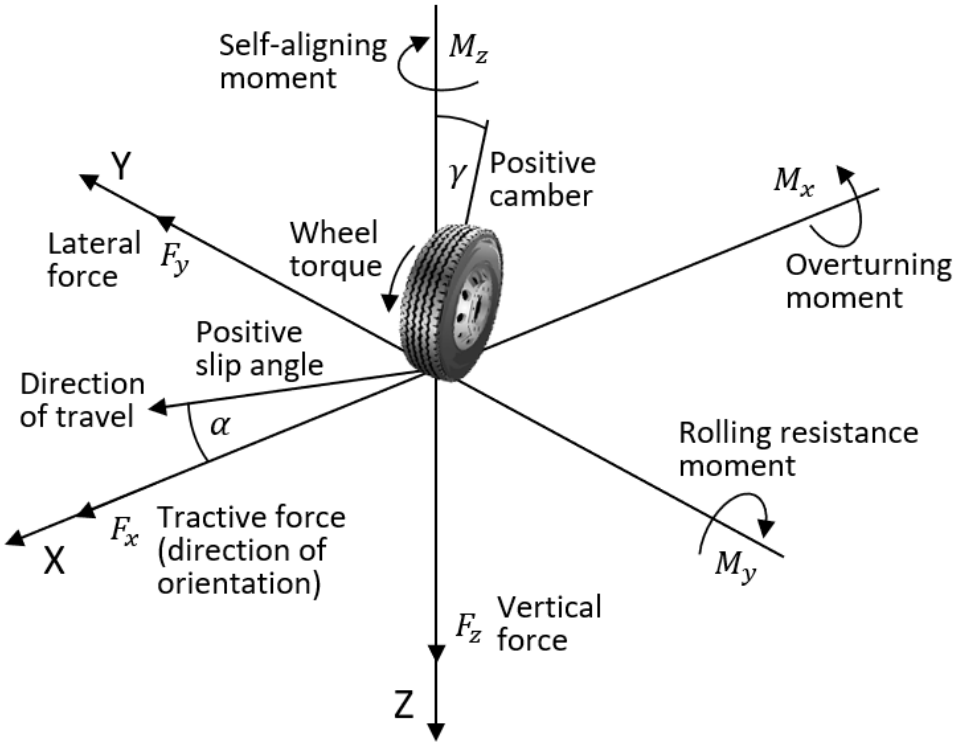

Figure 2.1: Tire forces and moments (adapted from [27]).

The three forces applied to the tire-road contact patch are a longitudinal tractive force F_x, a lateral cornering force F_y (for a non-zero slip angle), and a vertical force F_z due to the weight of the vehicle. The three moments involved – the overturning moment M_x, the rolling resistance moment M_y, and the self-aligning moment M_z – are mainly due to off-center forces in the contact patch [27]. Finally, there is the torque applied to the rolling wheel, which must balance the rolling resistance and tractive forces. The magnitudes and directions of these forces and moments depend on many factors, such as the camber angle γ, the tire inflation pressure, the wheel speed, and road surface qualities. The forces can also vary with time under transient conditions.

The main goal of tire modelling is to develop mathematical relationships between the tire properties and the applied and resultant forces. For example, the lateral force

F_y can be related to the slip angle α and other variables such as the vertical load, inflation pressure, etc. Some variables such as the tire-road friction coefficient, tire stiffness, or inflation pressure are usually assumed to be constant, while the rest of the variables are treated as inputs or outputs to the model. Some advanced models, however, have taken into account the variability of tire properties due to thermal effects and local variation [28]. The different types of models described next are different ways that researchers have invented to express the mathematical relationships between tire properties and forces.

2.2.2 Analytical Models

Analytical models are abstract representations or simplified versions of the tire with similar physical behaviour. For example, Pacejka's Magic Formula model (Eq. 2.1) uses the so-called magic formula to model the relationships between longitudinal slip and rolling resistance, and between slip angle and cornering force, using empirically determined coefficients [29].

$$y = D\sin[C\arctan\{Bx - E(Bx - \arctan[Bx])\}] \tag{2.1}$$

In Eq. 2.1, y is the output variable (e.g. F_x), x is the input variable (e.g. longitudinal slip), and B, C, D, and E are empirical coefficients. The Magic Formula model provides an input-output relationship that correlates very well with test data, but has drawbacks in that it can only model the relationship between two variables, and extensive tests need to be carried out to determine the coefficients for different loading and operating conditions.

Alternatively, more complex models like the rigid ring model represent the tire as a rigid ring connected to the hub by various springs and dampers [30]. One spring and damper is included for each degree of freedom, including translational, rotational, in-plane, and out-of-plane motions, as well as tread and terrain deflection as applicable. Instead of using a rigid ring, the string model represents the tire as a string under tension from circumferential and radial loads [15]. However, this simple model only considers 2D forces and ignores the anisotropic construction of the tire carcass.

In general, the greater the complexity of the model, the more numerous, in-depth, and expensive tests are required to determine all of the necessary model parameters. Examples of the physical experiments required include destructive tire tests [6], [31], [32], deflection tests [19], [21], [33], vibration tests [5], [24], [34], rolling resistance tests [22], [34], [35] and cornering tests [21], [22], [28]. For some of the simpler tests, the measured parameters such as tread depth or rubber stiffness can be directly input into the model. For other more complicated tests, especially when terramechanics are involved, the model parameters are tuned until the results of the virtual tests achieve good agreement with the physical tests [36], [37], [38]. Analytical models are thus relatively simple and efficient, but are limited in their application and depend strongly on performing the appropriate physical experiments.

2.2.3 FEA Models

FEA modelling is a flexible and popular approach, and multiple solver environments are available including ABACUS [5], [31], [33], [39]-[41], LS-DYNA [17]-[20], ADINA [42], and PAM-CRASH [2], [3], [21], [43], [44]. Since FEA tire models have a complex structure with many parameters, they are typically used when high accuracy is more important than runtime or computational cost. The tire is represented by a 3D geometric entity composed of many elements of different types, such as springs, beams, shells, membranes, and solids (Figure 2.2). Each main type of element also has different subtypes, mathematical formulations, and material models. Therefore, a large quantity of physical information about the tire is required in order to design a FEA model with behaviour and material properties matching the real tire. This can be obtained from the tire manufacturer or from destructive analysis of the tire [32]. The amount of information available greatly affects the accuracy of the FEA model. For example, in crash simulations using LS-DYNA, it was a common practice to model the tire as a simple pressurized membrane in order to minimize the overall model complexity since the tire was usually not involved in the crash [17], [18]. However, this simplified model led to unrealistic behaviour in different situations [17], [18] and was likely to cause poor results if used to simulate the front tire of a motorcycle impacting in a crash [19]. Therefore, it is beneficial to

have more complex FEA tire models involving multiple types of elements to improve the simulation accuracy under deformation conditions.

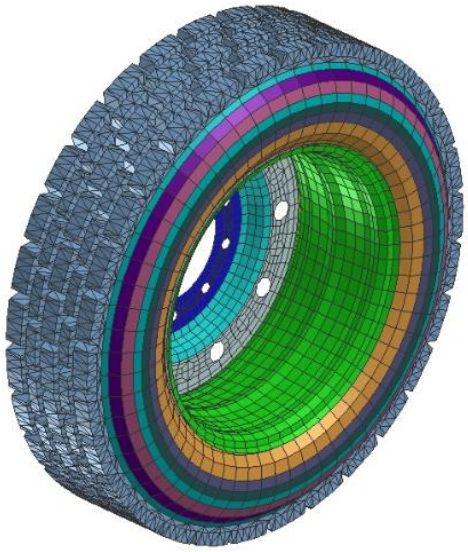

Figure 2.2: FEA model of a Goodyear 315/80R22.5 regional haul drive (RHD) truck tire. Different colours represent different parts.

Due to the flexibility of FEA, different tire modelling approaches have been used, including mixtures of shell, solid, and beam elements, [17], [18], mostly solid models [25], embedded rebar [6], [33], [39], [40], [45], and multilayer composite membranes incorporating fibres to represent the tire plies and belts [21]. Several areas of concern when modelling tires are reducing unwanted vibration [18], mesh entanglement [17], [18], realistic contact algorithms between the tire and rim and tire and ground [17], [21], [33], [40], [46], and modelling the internal tire pressure. The tire pressure can be modelled as an airbag for maximum realism, but this leads to issues with ensuring a closed surface within the tire, since the rim is a separate part [17], [18]. The other option is to apply a constant pressure to the inside surface of the tire, which is commonly done [17], [21], [25], [39] and allows for easy modification of the tire pressure during the simulation, such as when modelling tire blowout [17]. FEA is therefore a flexible and accurate method for tire modelling, but care must be taken to ensure accurate material information and component sub-models are used.

2.2.4 Rubber Models

A large portion of the tire volume is made of rubber, therefore the rubber sub-model used is critical for modelling overall behaviour of the tire. Rubbers are complex materials made of cross-linked chains of different polymers, and do not have linear-elastic or elastic-plastic stress-strain behaviour like metals. Instead, rubbers exhibit hyperelasticity, viscoelasticity, and hysteresis [47], [48]. Hyperelasticity means that rubbers can undergo large strains in excess of 100% before reaching yield or failure, as in stretching a rubber band. Viscoelasticity means that the stress in the rubber depends not only on the amount of strain, but also the strain rate. For example, a tire rolling at high speed will experience greater levels of stress due to viscous effects of the rubber. Finally, hysteresis means that the process of unloading rubber follows a different stress-strain curve than the loading process, and it may not fully return to its undeformed state. All of these different factors need to be considered when designing rubber sub-models.

The main technique for designing rubber models is the use of a polynomial strain energy equation (Eq. 2.2), which defines the shape of the stress-strain curve [48].

$$U = \sum_{i+j=1}^{N} C_{ij}(I_1 - 3)^i (I_2 - 3)^j + \sum_{i=1}^{N} \frac{1}{D_i}(J^{el} - 1)^{2i} \tag{2.2}$$

Where C_{ij} and D_i are material parameters, I_1 and I_2 are the first and second deviatoric strain invariants, and J^{el} is the elastic volume ratio. Making different assumptions, such as the value of N, lead to different models such as the Mooney-Rivlin, Yeoh, and Neo-Hookean models [48]. Each one has different strengths, weaknesses, and ranges of applicability depending on the assumptions used to make it. Examples of these models being used for FEA models include [2], [19], [21], [30], [39] (Mooney-Rivlin), [28], [31], [33] (Yeoh), and [6], [48] (Neo-Hookean).

Additional variables and formulas can be added to the rubber model to account for viscoelastic effects, such as kinematic or time-dependent strain variables [47], and external mass-proportional nodal damping [49]. Furthermore, rubber modelling under fatigue conditions has been explored using continuum damage mechanics

theory [50]. Thus, there are a variety of sophisticated material models available for modelling the hyperelastic, viscoelastic, and hysteresis behaviour of tire rubber, and it is important to select one that is accurate throughout the range of simulated conditions and can be characterized from available physical data or experiments.

2.3 Tire-Rim Interface

In the interest of simplification, vehicle models often assume that the wheel is a single unified entity transferring forces and moments internally from the wheel center to the tire tread and road interface. This is not completely accurate, since in reality the wheel is composed of two separate components, the tire and the rim, with forces and moments transferred through a contact interface between them. In most cases, there is little relative motion or significant energy loss at the interface, therefore it is reasonable for simulation purposes to assume that the two components are fixed together. However, there are well-known problems associated with the tire-rim interface, and particular cases such as tire mounting, tire-rim friction analysis, rim stress analysis, and tire-rim slip where the interface between the tire and rim is highly significant and cannot be ignored. This section will explain these situations and the techniques used to model and quantify the tire-rim interface.

2.3.1 Tire-Rim Interface Problems

It is well known by tire manufacturers that operational problems occur at the tire rim interface. At least two companies, General Motors and Nitto, have released service bulletins on potential slip at the tire-rim interface [9], [10]. The main cause of tire-rim slip is improper or excess use of lubricant during the tire mounting procedure, which reduces the holding friction between the tire and rim and allows slip to occur. In addition, during mounting, the tire-rim combination is carefully balanced to ensure there are no unbalanced forces causing vibration during rotation. Tire-rim slip misaligns these components and unbalances the tire, potentially causing unwanted vibrations during the operation of the vehicle. The manufacturers recommend careful adherence to tire mounting and bead lubrication procedures in order to prevent this from happening [9], [10]. Another possible cause of tire-rim slip is the presence of irregularities on the rim seat or tire bead causing improper seating. One tire company,

Michelin, has sponsored research into the occurrence of tire-rim slip, this time for low-pressure agricultural tires used in construction equipment [8]. This work focused on determining the minimum coefficient of friction required to prevent the onset of slip under different operating conditions, as well as experimentally measuring the coefficient of friction for different rubbers and lubricants. Thus, it is apparent that tire-rim interface problems are well-known in the industry and are the subject of both research and maintenance efforts.

2.3.2 Tire Mounting

As mentioned above, the tire mounting process is key in determining the quality of the tire-rim connection and the potential for tire-rim slip. This mounting process is often an initial step in setting up FEA tire models [28], [33], and has also been studied on its own. Figure 2.3 shows the details of the tire-rim interface involved in the tire mounting process.

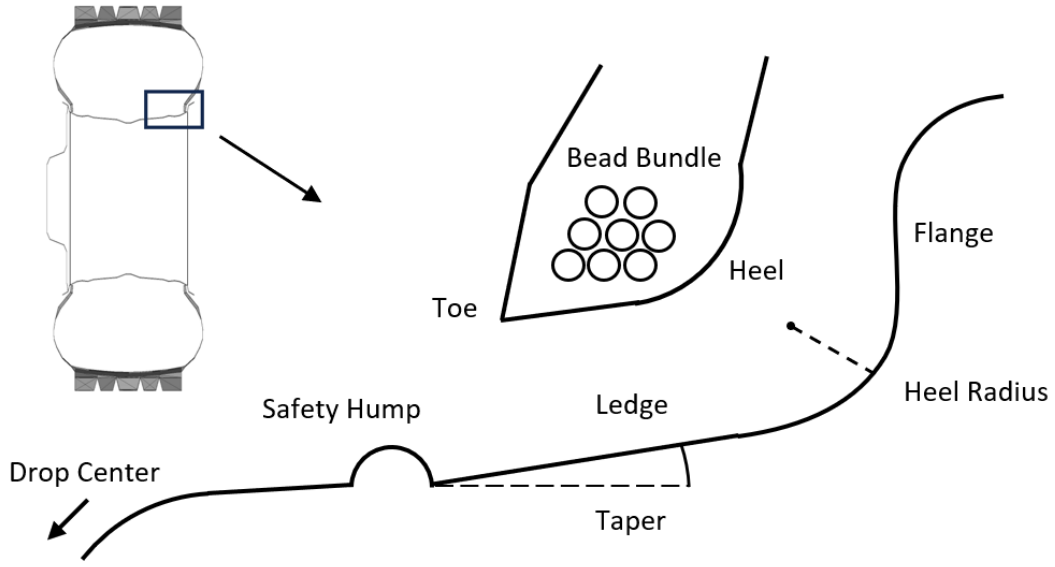

Figure 2.3: Parts of the tire and rim involved in the tire-rim interface. The inset shows their location relative to the wheel's cross-section. The bead seat refers to the entire area between the safety hump and the flange.

In 2006, Lee studied the effect of the rim profile on the tire-rim contact pressure distribution as well as design methods for maximizing the tire-rim frictional torque [7]. He found that frictional torque T_f was determined by an integral equation, Eq.

2.3, where r is the radial distance from the tire center, μ is the tire-rim friction coefficient, and p_{cont} is the tire-rim contact pressure. When the friction coefficient was assumed to be constant over the tire rotation and the flange size was neglected, the frictional torque was approximately equal to the area under the contact pressure curve.

$$T_f = \int r\mu p_{cont} 2\pi r ds \approx \mu \int p_{cont} 2\pi r^2 ds \quad (2.3)\ [7]$$

The contact pressure curve has also been studied by others [8], [25], [31], and the shape depends on the tire design. Race tires with high interference and low pressures have a higher contact pressure peak on the ledge compared to the flange, while passenger tires have low interferences and higher pressures have higher flange pressures [7]. Truck tires, with even higher inflation pressures, likely have even higher contact pressures on the flange. The general shape of the contact pressure distribution is similar for all tire types, however, with one peak on the ledge under the center of the bead bundle, and another on the flange due to the inflation pressure (Figure 2.4).

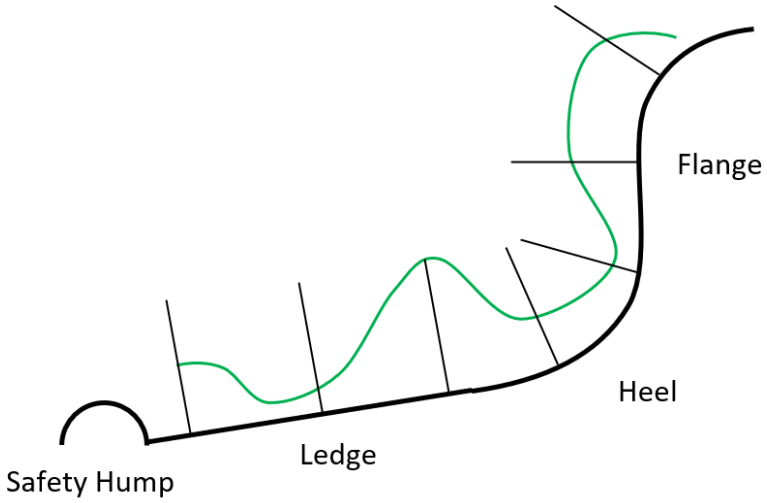

Figure 2.4: Representative tire-rim contact pressure distribution (green line) for a passenger car tire (adapted from [7]). The perpendicular lines give a relative scale.

Lee found that tapering the ledge with two different angles to reduce the interference underneath the bead bundle resulted in a flatter contact pressure curve in that region,

and therefore a higher area under the curve and a higher frictional torque [7]. This is one way to increase the tire-rim friction and reduce tire-rim slip. Another way is to add knurling to the ledge section of the rim profile to increase the surface roughness and local friction coefficient [8].

This leads to an important point in designing the tire-rim interface and bead profile. In theory, more friction is better, as long as the bead wires are not unduly prestressed. That means that a rougher surface along the rim and greater tire-rim interference are desirable. However, in real life, the tire is a separate component that must be stretched and mounted on the rim. To be mounted, the tire is located in the center of the rim, and then slowly inflated until it slides along the ledge and then is seated fully against the flange. This is often accompanied by an audible popping sound. The rim profile also will also include a hump just inside the ledge to reduce the chance of the tire unseating under lateral load. This requirement for the tire to slide into place along the ledge places an upper limit on the amount of friction allowable. If there is too much friction, the tire cannot be inflated into place without exceeding its safe pressure limit. This is why lubrication is usually applied during the mounting procedure to reduce the friction on the ledge. Additionally, a high interference fit would require the bead to stretch excessively in order to fit over the safety hump. Furthermore, friction on the ledge during the mounting process can also cause the tire bead to rotate a few degrees, putting it out of alignment with the seat and resulting in less contact [7]. Thus, there are multiple practical factors that must be considered in rim profile design in addition to simply maximizing the tire-rim friction.

2.3.3 Tire-Rim Friction Analysis

In an extensive research thesis, Reina analyzed and modelled the friction at the tire-rim interface [8]. Reina used multiple analytical models (unilateral, bilateral, shakedown) as well as FEA simulations to determine the minimum friction coefficients required to avoid tire-rim slip due to friction law violation. The analytical and FEA models showed good agreement, and it was found that rotating the tire had little on the minimum required friction coefficients compared to the static loading case. In addition, measurements were made of the friction coefficient between tire

rubber and rim specimens with three different surface treatments. Specifically, adding a lubricant reduced the friction coefficient range from 0.8-1.4 down to 0.2-0.5 [8]. The friction coefficient of rubber on tires is also known to vary under different load/pressure and sliding speed conditions [22], [111]. All of these factors should be taken into consideration when modelling the tire-rim interface.

Different studies have used different approaches for FEA modelling of the tire-rim interface and tire-rim friction. Some researchers have used gap elements or manual convergences [25], others a contact surface using simple friction [7], [31], [40], or a variable constraint height approach [46]. Alternatively, the tire bead can be assumed to be fixed to the rim [45] or the tire center [5], [21], [31], [39]. Furthermore, the friction coefficient is difficult to quantify. Due to the large number of influencing variables, such as interference, rim material, lubrication, contact pressure, sliding speed, and rim irregularities, most researchers have either assumed single values appropriate to their investigation [7], [40] or investigated the effect of varying the friction coefficient through an arbitrary range [8], [33]. Other options include advanced Cullen friction and exponential decay friction models [33], as well as a custom multivariate friction model [28]. It is important to choose friction and contact modelling methods that satisfy both the research goals and the computer resources available.

2.3.4 Rim Stress Analysis

An alternate approach to the tire-rim interface problem is from the rim side. When performing stress and impact analyses on the rim, it is important to understand how forces are transferred from the tire to the rim. Not only the axial torque, but also vertical and lateral loads are transferred through this interface. Traditionally, the force transfer is assumed to have an analytical distribution, such as the cosine model (Figure 2.5), eyelet model or Stearns [51]. Such theoretical distributions and other models have also been compared against strain sensor measurements on a physical tire [45], [51], [52].

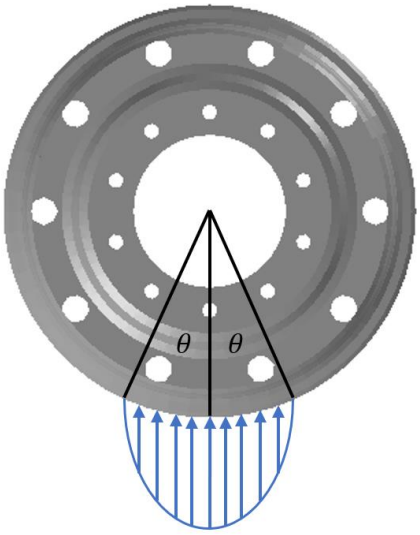

Figure 2.5: Cosine model for rim loading (based on [53]).

Due to the difficulty in directly measuring the distribution of forces at the tire-rim interface, different methods have been proposed to simplify the measurement and prediction process. Ballo et al. [45] developed a simplified semi-analytical tire model, which gave good results considering the small computational requirements when compared to strain measurements from an experiment and a full FEA model. Other researchers attempted to predict the contact pressure based on the external displacement of the loaded tire, using an FEA model of an aircraft tire for validation [42]. Thus, there has been some progress on developing theoretical and empirical methods of modelling the tire-rim interaction from the rim side.

2.3.5 Tire-Rim Slip

A final area of interest for the tire-rim interaction is the qualification of tire rim-slip performance under low-pressure driving conditions. For example, military vehicles may operate with lowered tire pressures for off-road driving, have damaged tires, or use run-flat tires, therefore qualifying the performance of tires under these non-standard circumstances is important [54]. A standard test method, ASTM F2803, for evaluating the rim-slip performance of tires was adopted by the ASTM in 2015 [55]. This standard used markings on the rim and tire sidewall to measure the relative circumferential slip between the tire and rim. Tests were done at the tire's maximum load rating with a high tractive effort of 60%. This slip measurement method is very

similar to that recommended by passenger car tire manufacturers [9], [10]. Tire-rim slip is therefore a research area of interest to both civilian and military organizations.

2.4 Terramechanics

The interactions between tires and different kinds of off-road terrain such as soft soils have been of interest to researchers for many years [56]. This is because the off-road behaviour of a tire is substantially different than its on-road behaviour. On a hard, flat surface such as pavement or concrete, the main factor to consider in characterizing the tire-road interaction is the coefficient of friction, which varies depending on the wetness of the surface, for example [27]. On off-road terrain, however, there are multiple other factors to consider such as the soil sinkage and cohesion characteristics, which affect the tire due to its vertical load [27]. In fact, the negative relationship between inflation pressure and rolling resistance for hard surfaces is reversed on off-road terrain, where the rolling resistance increases with inflation pressure due to a combined sinkage and bulldozing effect [27]. Therefore, the characterization and modelling of the tire-terrain interaction is an important area in tire dynamics, as well as a challenging one due to the number of soil types and variables to quantify.

2.4.1 Soil Characterization

Soil properties relevant to the tire-terrain interaction have been measured in different ways using different measurement tools [57]. Soils are mainly classified by their texture or particulate content, which is the relative amount of the different solid particles they contain (Figure 2.6) [58]. The particulate content affects other soil properties such as bulk unit weight, cohesion, friction angle, and moisture saturation limit. Combined with moisture content, these properties result in a wide variety of soils ranging from dry, dense soils such as fine sand, to less dense sandy loams, and to heavy, wet clays. There are also specialized soils such as peats [27]. Some representative values of soil properties are shown in Table 2.1. Typically, adding moisture increases soil density, but once the saturation limit is reached, part of the soil becomes liquid and the soil becomes muddy and soft [57], [59]. This has been demonstrated by lab shear tests showing that the friction angle reaches a maximum

at a particular moisture level, and then decreases afterwards [60]. Furthermore, additional factors such as soil depth, compaction, tillage, and fertilization can change the soil properties [61]-[63].

Table 2.1: Representative soil properties [64]

Property	**Symbol**	**Units**	**Min Value**	**Soil Type**	**Max Value**	**Soil Type**
Bulk Unit Weight	γ	kN/m^3	11	dry soil	18	dense, wet soil
Cohesion	c	kN/m^2	~0	dry, loose sand	>100	hard, dry clay
Friction Angle	ϕ	degrees	0	pure clay	40	compact sandy loam

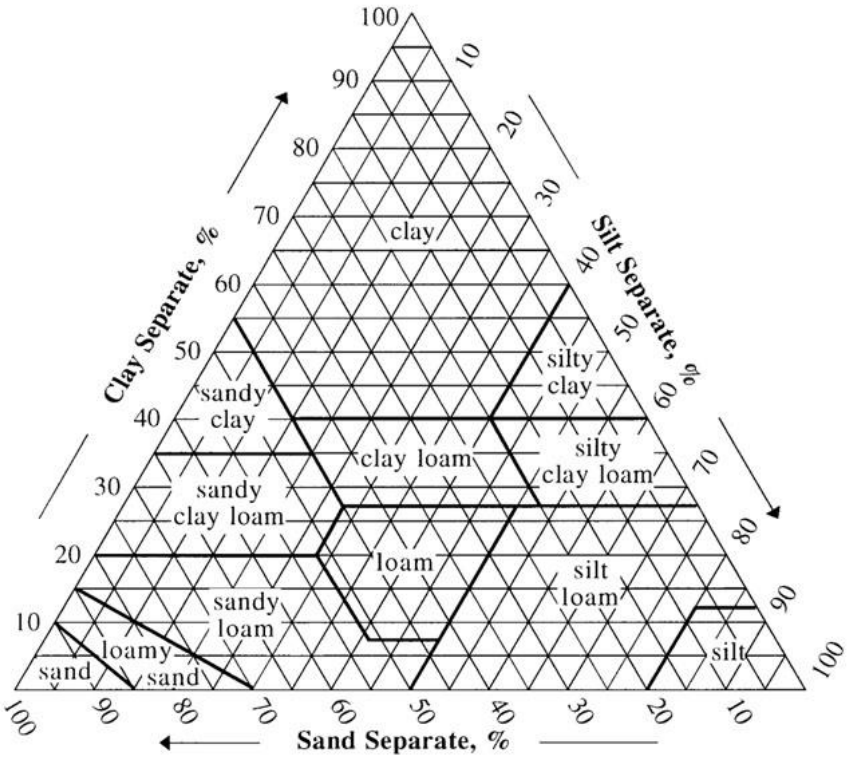

Figure 2.6: Soil composition classification chart [58].

Of the most interest to the study of terramechanics, however, are the soil's sinkage and shear characteristics. Soil sinkage was first investigated by Bekker [65], and he developed the following well-known relationship (Eq. 2.4) between soil sinkage (z)

and applied pressure (p_{soil}), where b is the size of the plate and n, k_c, and k_ϕ are empirically determined parameters.

$$p_{soil} = (\frac{k_c}{b} + k_\phi)z^n \tag{2.4}$$

Other researchers such as Reece have developed modified versions of the Bekker equation with additional parameters and improved applicability. Reece's version used the dimensionless ratio z/b and had better agreement with bearing capacity theory [56]. Bekker's equation, however, remains the simplest and easiest for determining the empirical coefficients.

Bekker developed another equation for the shear characteristics of the soil (Eq. 2.5), where p_{soil} is the applied normal pressure, j is the horizontal displacement, τ is the shear stress and c, ϕ, and K are empirically determined coefficients [65].

$$\tau = (c + p_{soil}\tan\phi)(1 - e^{-\frac{K}{j}}) \tag{2.5}$$

The basis of Bekker's shear equation was an equation for the maximum shear stress τ_{max} (Eq. 2.6), which was first proposed by Coulomb for materials such as soils that undergo compressive loads [66]. This Coulomb relationship has also been popularized in the well-known Coulomb-Mohr material failure criterion.

$$\tau_{max} = c + p_{soil}\tan\phi \tag{2.6}$$

In order to determine the characteristics of the soil, field or lab tests are usually carried out on the desired soil mixture using devices such as the cone penetrometer, bevameter with shear annulus, as well as vane, triaxial, and direct shear tests, [27], [57], [67]. The cone penetrometer is shown in Figure 2.7. It consists of a cone-shaped probe with standardized dimensions (e.g. 30°, 0.5 in^2 [27], [57]) attached to a force measuring device, which in this example is an analog gauge. The penetrometer is inserted into the soil to a specified depth and with a specified sinkage rate and the average force measured divided by the cone area is taken as the cone index of the soil [27], [57]. Usually, an average value is taken during penetration to the depth expected for a wheeled or tracked vehicle to sink, and is used as a rough measure of

the strength of the soil. However, the cone index is known to vary with depth [57] and does not directly correlate with complex soil parameters such as shear strength and friction angle. The cone index is useful as a quick and standard measure, but other methods are needed for more detailed soil analysis.

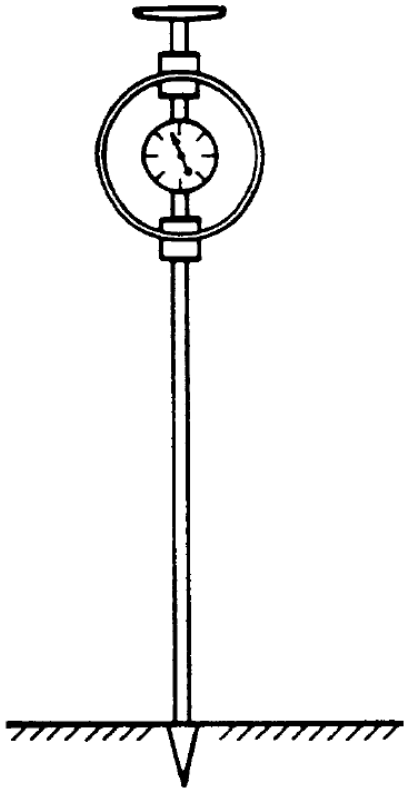

Figure 2.7: Cone penetrometer device for measuring soil cone index (reproduced from [27]).

The bevameter is a multicomponent device popularized by Bekker for use in determining the empirical coefficients of his characteristic soil equations [65], [67]. Figure 2.8 shows a schematic of some of the main components of a bevameter, the physical layout may vary. There is one section (on the right) that pushes plates of different sizes with different pressures into the soil in order to measure the pressure-sinkage characteristics (p-z plot). A second section rotates a shear plate (annulus) under different vertical pressures and measures the torque required to rotate a given angle (M-θ plot), from which the shear characteristics of the soil can be determined [27], [57]. The bevameter improves upon the cone penetrometer in that it can

measure both pressure-sinkage and shear characteristics at the same time in a field setting, but at the cost of substantially more complicated equipment. Alternatives to the annulus method of shear measurement used in the bevameter include rotating vanes, a triaxial test rig, and a direct shear box [57].

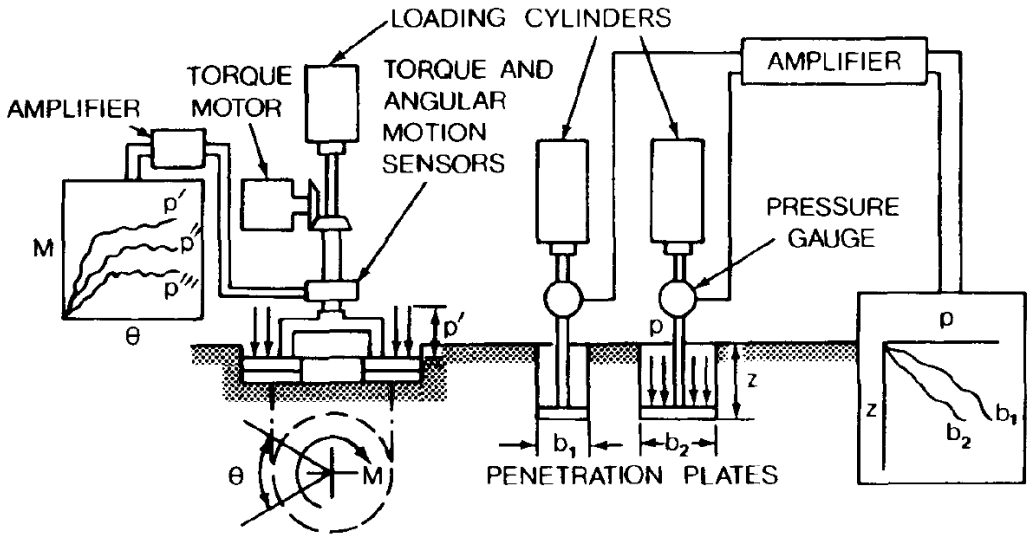

Figure 2.8: Schematic of a bevameter device for measuring Bekker equation parameters (from [67] as reproduced in [27]).

It is important that the soil characterization is done over an appropriate range of loadings. For example, Chuan et al. measured the pressure-sinkage characteristics of a very soft, oversaturated silty soil using a narrow range of pressures from 0.4 to 0.9 kPa [59]. This resulted in Bekker equation parameters with a negative k_ϕ value, which the authors acknowledged was unrealistic and demonstrated the limits of the equation in predicting real-life behaviour of a wide variety of soils and conditions. Due to the narrow range of input pressures, the determined parameters would not be very useful for modelling the behaviour of a soil subject to pressures in the neighbourhood of 100 kPa from a loaded tire. Therefore, it is important to conduct soil measurements over a load range that is preferably wide and similar to that experienced from wheel traffic in order to use the resulting data for terramechanics modelling.

2.4.2 Soil Modelling

Once a soil has been characterized, the next step in modelling the tire-terrain interaction is to develop a virtual soil model. FEA techniques are a desirable approach due their accuracy and flexibility. Early FEA terrain models treated the soil as an elastic-plastic solid [40], [41], [43], a large, smooth continuous domain whose deformation and developed surface forces matched that of the desired soil. This method had several drawbacks, including poor modelling of compaction, penetration and associated shear forces [3], [68].

An alternative approach to a continuum soil model is a particle model. Different particle models include the discrete element method (DEM) and smoothed particle hydrodynamics (SPH). These particle models are significantly more accurate than the continuum models in simulating soil behaviour, since real soils are composed of many small particles. However, they are computationally very intensive and require a large number of parameters to be set [43], [69], [37].

2.4.3 DEM

DEM was originally developed by Cundall in the 1970s as a numerical model for systems of round objects in contact [70]. It has subsequently seen multiple improvements and modifications and is often used for modelling the behaviour of granular materials such as rocks and soils [71]. DEM treats the entire environment, especially the soil particles, as a set of rigid bodies of various sizes and geometries interacting via contact forces. The governing equations are discretized which results in a quadratic optimization problem being solved for each time step, which can be implemented in a sufficiently advanced multibody physics simulator such as Chrono [72]. This is generally a computationally intensive process and multiple avenues are being researched for improving the computational efficiency [73]. Figure 2.9 below shows different methods of force transfer between the particles, including normal forces, tangential friction forces, and rotational forces. A rolling resistance parameter has also been added to capture the effect of the rotational motion of individual soil particles on the behaviour of the surrounding soil [74].

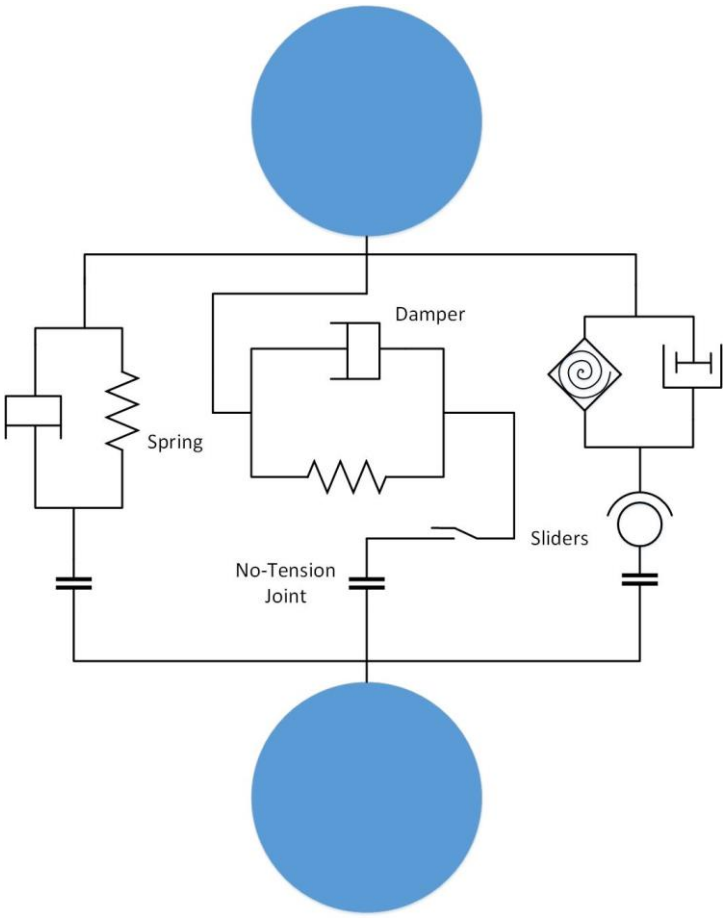

Figure 2.9 Particle interaction model for normal, tangential, and rotational forces (adapted from [74]).

A key strength of the DEM method is its flexibility in terms of the particle parameters. The particles can be modelled as spheres of different sizes, with the size range and distribution chosen to balance accuracy and computational cost. The particles can also take on irregular polyhedral shapes, which better matches the rough, interlocking surfaces of real soil particles, but this adds to the computational cost [38]. The DEM method has been experimentally compared with older empirical terramechanics/wheel models originated by Bekker and has shown substantially improved accuracy and flexibility, albeit at an increased computational cost. The calibration of the DEM model is also a challenge, due to the high number of parameters that must be determined by trial and error to arrive at a good approximation of the soil behaviour [38]. Despite these drawbacks, DEM has been

used to form the basis of a next-generation comprehensive military mobility simulator [75], as well as other projects [71], [76].

2.4.4 SPH Method

Gingold and Monaghan developed the smoothed particle hydrodynamics or SPH technique as simple particle-based way to model asymmetric astrophysical phenomena, such as gas clouds [77], [78], and it has subsequently been extended and modified to be capable of simulating diverse phenomena such as explosions, multiphase flow, and soil mechanics [79], [80]. Instead of treating a material as a connected series of nodes and elements, such as in traditional FEA, SPH treats the material as a collection of separate particles without fixed connections. Each particle is defined by a center of mass, radius, and domain of influence [80]. The domain of influence is located at a certain radial distance from the particle's center of mass, called the smoothing length h (Figure 2.10). This smoothing length can either be fixed, set as a multiple of the particle radius, or dynamically change according to the particle density between maximum and minimum values [80]. For soil simulations, Lescoe found that the optimum value of the smoothing length was 1.3 to 2.1 times the particle radius, with minimum and maximum values of 1 and 100, respectively [81]. A kernel function is used to weigh the interactions between particles in the domain of influence and the current particle. This means that the conservation equations become a set of ordinary differential equations which can be solved without discretization, providing an advantage over FEA [78]. Different formulations are available for the specific conservation and state equations, depending on the physics and constraints of the materials modelled [79], [80].

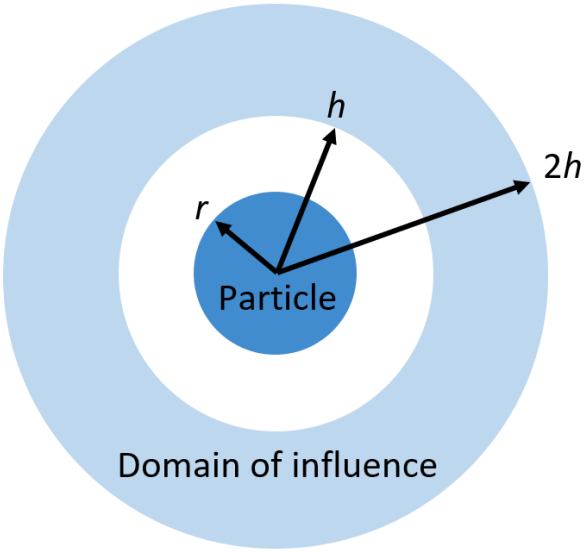

Figure 2.10: SPH particle domain of influence extends from the smoothing length h to a distance of $2h$ (adapted from [80]).

In addition to the particle properties, the complete simulation of an SPH soil requires an associated material model. Two possible models are the elastic-plastic hydrodynamic and Murnaghan material models, shown in equations 2.7 and 2.8 [80]. The elastic-plastic model tends to give better results for firm soils such as clay and sand [37], while the Murnaghan model is more accurate for the behaviour of extremely soft terrains such as flooded surfaces [82]. The symbols used in each equation are explained in Table 2.2. While the elastic-plastic hydrodynamic model (equation 2.7) has 6 coefficients, in practice all them were set to zero except C_1, which then corresponded to the bulk modulus of a standard elastic-plastic solid material [81].

$$p = C_0 + C_1\mu + C_2\mu^2 + C_3\mu^3 + E_i(C_4 + C_5\mu + C_6\mu^2) \tag{2.7}$$

$$p = p_0 + B\left(\left(\frac{\rho}{\rho_0}\right)^{\gamma} - 1\right) \tag{2.8}$$

Table 2.2: Parameters for SPH material equations of state

Symbol	Description
p	Internal pressure at particle
$C_0 - C_1$	Calibrated material constants
μ	$\mu = \rho/\rho_0 - 1$
E_i	Current internal energy
p_0	Reference pressure
B	Bulk coefficient, determines speed of sound in material
ρ	Current mass density
ρ_0	Initial mass density
γ	Equation exponent, typical value is 7

One challenge in modelling the tire-terrain interaction is that the SPH soil models are generally defined by a different set of parameters than the ones used to characterize the behaviour of the physical soil, such as the ones in Bekker's equations [65]. A trial-and-error method can be used to find a set of SPH model parameters that accurately represent the soil characteristics by matching pressure-sinkage and shear stress curves, as done by Zeinab et al. [37]. This parameter tuning allows the SPH models to quantitatively match the behaviour of multiple soils [2], [37]. Furthermore, SPH accurately models the qualitative shear, deformation, and compression of real soils [3], [68], [81]. To conclude, SPH represents a promising technique for modelling tire-terrain interactions, although care must be taken when measuring soil characteristics and calibrating the model parameters.

2.5 Virtual Sensing

Virtual sensing is a recent field of research at the intersection of system modelling and state measurement techniques. The basic idea is that in many situations, there are certain parameters of a system that are too difficult to measure directly, either due to physical access, equipment cost, or physical abstraction. The solution to this problem is to create a state-space model of the system that can be used to predict unknown parameters from measured ones using knowledge about the physical laws governing the system [83]. There are a wide variety of mathematical techniques that have been

developed, ranging from state-space observers to advanced neural networks [12], [84]-[87]. The algorithm added to the system model, regardless of its specific formulation, is called a soft or virtual sensor because it is able to measure state parameters without any physical device required. Virtual sensors were first developed for industrial process applications [85], [88], [89], and are starting to spread to other areas where state measurement is important, such as automobile control systems and wind tunnel testing [84], [90]. In this section, four different soft sensor categories will be described – first-principle models, filters, observers, and neural networks – followed by examples of their application to automotive systems.

2.5.1 First-Principle Models

First-principle models are a typical theoretical estimation method that uses the basic physics of vehicle motion to create a mathematical model for soft sensing. There are two kinds of first-principle models commonly applied to vehicle state sensing, kinematics-based and dynamics based [84], [86]. Other kinds of first-principle models such as those based on chemical reactions and conservation laws exist, but they are typically used in the process industry [85]. The difference between kinematics- and dynamics-based models is that the kinematic-based models include only kinematic variables (displacement, speed, acceleration, etc.) and ignore the effect of forces, while dynamics-based models include appropriate selections of the forces affecting the vehicle (longitudinal, lateral, vertical, etc.) [84], [86].

A simple kinematics-based model considering only the longitudinal motion of the vehicle (Eqs. 2.9 and 2.10) could be implemented by measuring the longitudinal acceleration a_x with a vehicle-mounted accelerometer and then performing integration to estimate velocity and displacement. Unfortunately, the simplicity and lack of multiple corroborating variables in kinematics-based models makes them vulnerable to accumulated sensor error, and consequently more sophisticated and accurate dynamics-based models are preferred. [84].

$$v_x = \int a_x dt \tag{2.9}$$

$$d_x = \int v_x dt \tag{2.10}$$

Dynamics-based models, on the other hand, use some form of the basic equation $\sum \vec{F} = m\vec{a}$, with multiple terms added to include forces from different sources. These dynamics-based models can then use multiple coordinate systems and vectorial combination to create a state-space model describing the vehicle's behaviour to the degree of fidelity desired. The exact form the equations take depends greatly on the behaviour to be modelled. For example, rollover behaviour would be modelled with an equation including roll angle and vertical force variables [84], [91], while lateral dynamics are often estimated with a 2 degrees of freedom (DOF) bicycle model (Figure 2.11, Eqs. 2.11 and 2.12) where the yaw rate r and steering angle δ are the key variables to be considered [27], [84], [86]. In Eqs. 2.11 and 2.12, m represents the vehicle's mass, I represents the moment of inertia, and v_x and v_y represent the longitudinal and lateral velocities. Additional wheels and vertical DOF can be added to make models with 8 or more DOF that have improved accuracy and can model more behaviours [86].

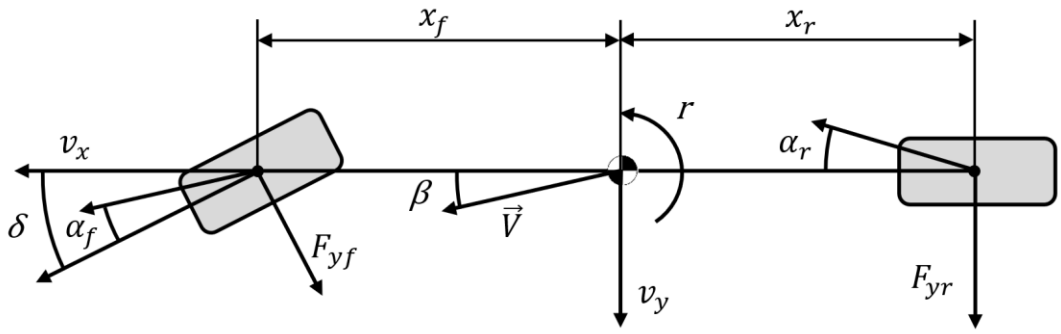

Figure 2.11: 2 DOF bicycle model for vehicle dynamics modelling (based on [86]). α_f and α_r are the front and rear slip angles, $\vec{V}$ is the vehicle's net velocity, and β is the vehicle's sideslip angle.

$$m(\dot{v}_y + rv_x) = F_{yf} + F_{yr} \tag{2.11}$$

$$I\dot{r} = F_{yf}x_f - F_{yr}x_r \tag{2.12}$$

In theory, there is no limit to the DOF that can be added to a model, especially with the availability of computer algorithms and powerful FEA methods. However, there are practical problems with implementing high-fidelity first-principle models. First, there are a large number of model parameters to be determined, such as stiffnesses and damping coefficients, that are time-consuming and expensive to measure for the real-life vehicle systems. Second, a deep and accurate understating of the physical phenomena involved is required to build the models [89], [90], which may not be possible to obtain for complex nonlinear components such as tires. The first-principle models developed for tires in the past are presently being replaced by more accurate nonlinear and data-driven models, as described in the following sections. Finally, first-principle models are limited in their applicability because their calibrated parameters are only valid for the measured real-life system, and any changes to the system (e.g. swapping tires) requires a recalibration of the model parameters. This inflexibility causes real challenges when attempting vehicle state estimation under dynamic conditions, which is one of the reasons why more advanced filters and state observers were developed as described in the next section.

2.5.2 Filters and Observers

A filter is an additional algorithm added to the vehicle model that predicts state parameters based on statistical analysis. The most common kind of filter is a Kalman filter (KF), which assumes a Gaussian measurement noise distribution. Other kinds that use a different noise distribution exist as well, such as particle filters [84]. The basic Kalman filter, also known as a linear quadratic estimator, estimates the current system state based on the previous system state and the uncertainty associated with the previous state measurement [86], [92]. This is done in two steps, the prediction step and the update step. In the prediction step, the Kalman filter estimates the value for the current state $\widehat{\boldsymbol{x}}_k$ using Eq. 2.13. This prediction depends only on the value for the previous state $\widehat{\boldsymbol{x}}_{k-1}$ and the state matrices $\boldsymbol{A}$ and $\boldsymbol{B}$. In the update step (Eq. 2.14), the estimated output $\boldsymbol{H}\widehat{\boldsymbol{x}}_{k|k-1}$ is compared with the measured output $\boldsymbol{y}_k$ and an error quantity is generated. This error is assumed to have a purely Gaussian distribution with zero mean and known variance. The current state value is then updated based

the measurement error multiplied by the optimal Kalman gain $\boldsymbol{K}_k$. Over time, the estimated output converges to the measured output with minimal error.

$$\hat{\boldsymbol{x}}_{k|k-1} = \boldsymbol{A}\hat{\boldsymbol{x}}_{k-1|k-1} + \boldsymbol{B}\boldsymbol{u}_k \tag{2.13}$$

$$\hat{\boldsymbol{x}}_{k|k} = \hat{\boldsymbol{x}}_{k|k-1} + \boldsymbol{K}_k(\boldsymbol{y}_k - \boldsymbol{H}\hat{\boldsymbol{x}}_{k|k-1}) \tag{2.14}$$

The Kalman filter method is optimal because the Kalman gain $\boldsymbol{K}_k$ is calculated at each step from the estimated covariance matrix to estimate a new state value with the minimum possible mean-squared error given the Gaussian distribution. This allows the highest degree of accuracy possible with a linear estimator in the presence of measurement uncertainty [86], [92]. Basic Kalman filters have broad applicability, but due to their linear nature, they are only good for vehicle models with small slip angles. For larger slip angles, Kalman filters with nonlinear capability are required, such as extended Kalman filters (EKF), unscented Kalman filters (UKF), cubature Kalman filters (CKF), and many other variants, with different levels and types of complexity [12], [84], [86], [87], [92].

A state observer, on the other hand, is similar to a Kalman filter in that an additional equation is computed in parallel with the state space equations, but differs in that it does not explicitly address noise in the state variable to be estimated, and instead focuses on the stability and linearity of the observer. The most common types included a linear or Luenberger observer (LO), a sliding mode observer (SMO), and a nonlinear observer (NLO) [84], [87]. Recursive least-squares (RLS) is often classified as an observer as well [84], [87]. These different types of observers are frequently modified, cascaded, and combined in various ways with other methods such as a Kalman filter to obtain an effective and robust estimator for the system under observation [84], [87]. Next, each type of observer will be described in more detail.

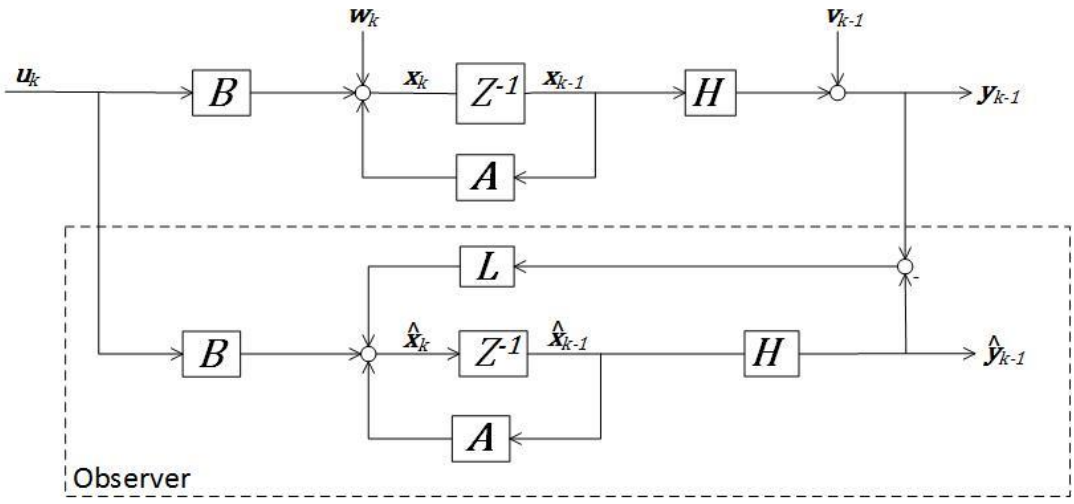

Figure 2.12: Block diagram of discrete and time invariant linear system with LO.

A general linear system to be observed is described by Eqs. 2.15 and 2.16, where $\boldsymbol{A}$ is the state transition matrix, $\boldsymbol{B}\boldsymbol{u}_k$ is the input term, $\boldsymbol{w}_k$ and $\boldsymbol{v}_k$ are plant and measurement noises. An LO to observe this system is described by Eq. 2.17 [87] and shown graphically in Figure 2.12. In these equations, bold variables ($\boldsymbol{w}_k$) are vectors, bold capitals ($\boldsymbol{A}$) are matrices, and ˆ denotes an estimated quantity.

$$\boldsymbol{x}_k = \boldsymbol{A}\boldsymbol{x}_{k-1} + \boldsymbol{B}\boldsymbol{u}_k + \boldsymbol{w}_k \tag{2.15}$$

$$\boldsymbol{y}_{k-1} = \boldsymbol{H}\boldsymbol{x}_{k-1} + \boldsymbol{v}_{k-1} \tag{2.16}$$

$$\hat{\boldsymbol{x}}_k = \boldsymbol{A}\hat{\boldsymbol{x}}_{k-1} + \boldsymbol{B}\boldsymbol{u}_k + \boldsymbol{L}(\boldsymbol{y}_{k-1} - \hat{\boldsymbol{y}}_{k-1}) \tag{2.17}$$

The key parameter is the gain matrix $\boldsymbol{L}$, which is used to multiply the output estimation error ($\boldsymbol{y}_{k-1} - \hat{\boldsymbol{y}}_{k-1}$) to obtain the estimated state vector $\boldsymbol{x}_t$. For an LO, $\boldsymbol{L}$ is constant, hence the observer equation is linear. $\boldsymbol{L}$ is chosen such that the closed-loop stability criterion for $\boldsymbol{A} - \boldsymbol{L}\boldsymbol{H}$ is met. If such an $\boldsymbol{L}$ does not exist, the system is not observable [87]. In simple terms, for an observable system with a properly selected $\boldsymbol{L}$, the estimated state $\hat{\boldsymbol{x}}_t$ will converge to the actual state $\boldsymbol{x}$ under steady-state conditions [91].

Another type of observer, the sliding mode observer, has been thoroughly described in a survey by Spurgeon [93]. An SMO is closely related to sliding mode controllers, a type of variable structure control system, in which a function switches between a

set of different controllers (or controllers with different parameters) in order to find the optimum controller for each system state. A sliding variable $s(t)$ depending on the discontinuous input signal is selected such that the estimation error is zero when $s(t) = 0$. In a first-order SMO, the input signal affects $\dot{s}(t)$, while for second order SMOs the input signal can affect $\ddot{s}(t)$ as well. The higher order effect is applied to ensure $s(t)$ is stable for the full range of the input signal, since the discontinuous nature of and uncertainties in the input signal can cause instability in the SMO.

The SMO design problem has already been solved for linear systems, with the benefit that observability is no longer essential [93]. In addition, SMOs have the advantage that they converge to the ideal sliding variable range within a finite amount of time. Work has also been done to design SMOs for nonlinear systems, building on the concepts and designs for linear systems [93].

In reality, accurate state-space models for many systems are non-linear, hence NLOs need to be designed that retain stability when applied to nonlinear systems. Substantial effort has been spent on linearizing nonlinear systems in order to allow for the use of stable LOs [94], but this reduces the accuracy and performance of the estimator with respect to the real-life system. The formulation of an NLO depends highly on the nonlinear stability theory used to develop it [84], such as input-to-state stability theory [95] and the Lyapunov criteria [96]. In order to account for nonlinearities, the observer design is different, with an estimate of the state rate of change $\dot{\boldsymbol{x}}$ instead of the state vector $\boldsymbol{x}$, and a time-varying gain $\boldsymbol{L}(t)$ [94]. Extensive design testing is also required to ensure the NLO remains stable in the event of measurement uncertainties and noise in sub-models [94].

Finally, the recursive least squares (RLS) method is a simple, efficient algorithm for identifying a linear parametric equation that fits a set of $(\boldsymbol{x}, y)$ input/output data with the minimum squared error [97]. For example, in the linear equation Eq. 2.18, $a_0 \dots a_n$ are the set of parameters optimized, while $f_1(\boldsymbol{x}) \dots f_n(\boldsymbol{x})$ are the set of variables or simple functions used to build the least-squares approximation.

$$y = a_0 + a_1 f_1(\boldsymbol{x}) + a_2 f_2(\boldsymbol{x}) + \cdots + a_n f_n(\boldsymbol{x}) \tag{2.18}$$

RLS is a fast recursive algorithm, well-suited for real-time signal processing, but it struggles to capture complex, nonlinear variable interaction. Advanced, nonlinear, artificial intelligence methods are better for these types of problems.

2.5.3 Neural Networks

Neural networks are an alternative virtual sensing method that has proven to be highly versatile and is used in many fields of research, such as computer vision and speech recognition [98], [99]. The first neural networks were proposed by McCulloch and Pitts in 1943 as a way of mathematically imitating the behaviour of neurons in the human brain [100]. A basic neural network (Figure 2.13) consists of three sections: an input layer, one or more hidden layers, and an output layer. The values in the input layer are multiplied by weights and summed at each neuron in the hidden layer. This sum is then compared to the neuron's activation threshold by an activation function, which determines the output value of the neuron. The output of each neuron is then fed forward, multiplied by more weights and summed at the next layer of neurons. This feedforward process continues until the values at the output layer are calculated and then sent out from the network. Training is done by iteratively modifying the values of the weights until the values of the output layer are sufficiently close to those in the training input/output dataset. New methods of constructing and training neural networks such as the multi-layer perceptron and backpropagation were subsequently developed [101], [102].

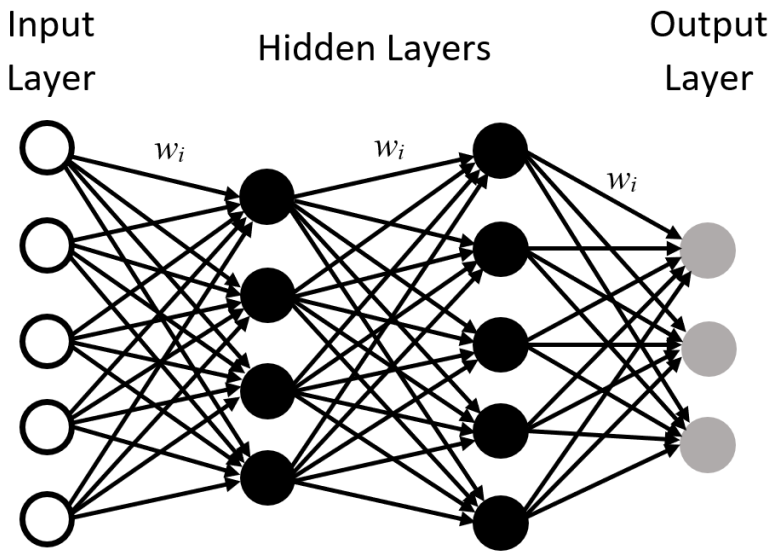

Figure 2.13: A double-layer feedforward neural network with nine neurons. Each layer is fully connected to neighbouring layers with one weight (w_i) per connection for a total of 55 weights.

A more recent development, enabled by readily available high-power computing, is the use of deep neural networks (DNNs). A DNN is characterized by the large number of hidden layers it has, sometimes with millions of weights. Schmidhuber roughly classified a DNN as a network with more than 10 weights applied to an input before it reaches the output layer [101]. DNNs can be further distinguished by the construction of the hidden layers. Convolutional neural networks (CNNs) use convolution and pooling layers, recurrent neural networks (RNNs) use neurons with self-connections, and deep belief networks (DBNs) use restricted Boltzmann machines [101]. As can be imagined, complex DNNs of many types can be created by mixing and matching layers of different types with different settings and training methods to create networks tailored to specific tasks.

An important distinction when working with neural networks is the type of task they are designed to perform. First, there is the classification task, in which the network is designed to take an input dataset, such as a collection of images, and assign each image to one of a finite number of discrete bins or classes. This tends to be a relatively simple, offline task. On the other hand, there is the regression task. In this case, the network is given a multivariate input stream sliced into windows of time, and is

required to estimate one or more continuous output variables that it has been trained to relate to the input stream. In this case both the inputs and outputs are functions of time, and the regression is usually done in an online, real-time basis, therefore computational efficiency is important [103]. Virtual sensing usually requires this kind of regression or continuous modelling task.

In the case of virtual sensing, a neural network provides a data-driven black-box approach where a variety of measured inputs about a system's state can be directly correlated with one or more unmeasured parameters. This works by first training the neural network in a situation where both the measured and unmeasured parameters are known. Then, once the training is complete, the neural network acts as a virtual sensor since it represents a black-box relationship between the measured values and the virtually measured ones. This is a data-driven method since large quantities of measured data are used to create the neural network rather than physical laws governing the system. Thus, neural networks provide a viable framework for virtual sensing with some advantages over other methods.

2.5.4 Automotive Applications

According to several literature surveys on vehicle dynamic state estimation [12], [84], [86], the most common parameters estimated with virtual sensors are the sideslip angle (β), the tire-road friction coefficient (μ), the roll angle (ϕ) and various tire forces. The sideslip and roll angles are shown in Figure 2.14, while the tire force system is shown in Figure 2.1. Following is a selection of papers in which each of these parameters is estimated using different methods.

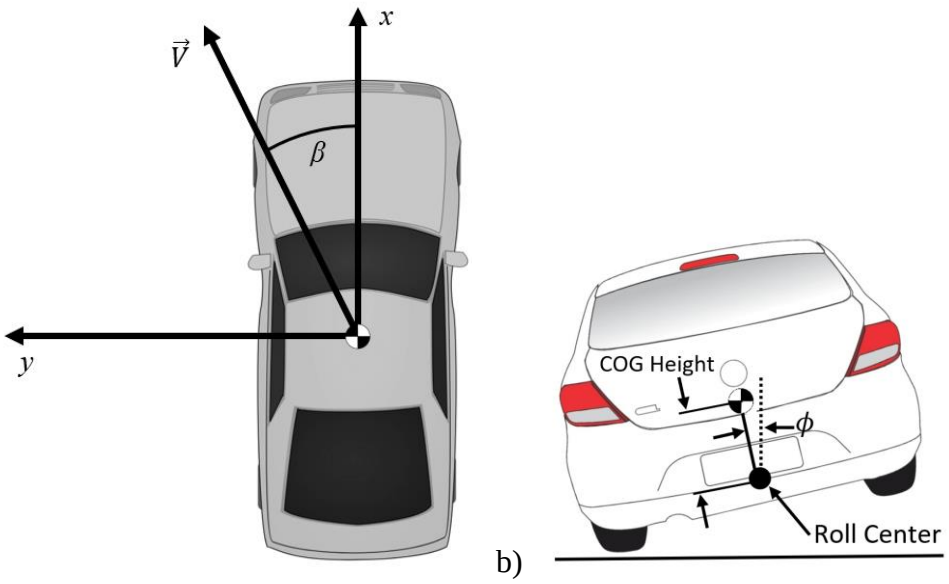

Figure 2.14: Schematics showing a) sideslip angle β and b) roll angle ϕ.

The vehicle sideslip angle is an important state parameter for different active control systems, but cannot be measured directly without using expensive and specialized sensors, therefore it is a prime candidate for virtual sensing techniques [86]. First principle, filter, and observer-based methods can be limited in accuracy, especially for extreme conditions, therefore Ghosh et al. chose a neural network estimation method for estimating the sideslip angle of a high-speed, all-wheel-drive prototype vehicle [104]. They used an 8-layer long short-term memory (LSTM) neural network with multiple directly measured inputs such as the wheel speeds and 3-axis accelerations. The results were impressively accurate, even for conditions such as drifting with up to 80% longitudinal wheel slip and slow steering, where other estimation methods usually have trouble.

In 2007 Svendenius used a relatively simple first principles-type brush model method to estimate the tire-road friction coefficient on asphalt, snow and ice [105]. The brush model (Eqn. 2.19) expresses the longitudinal contact patch force F_x as a function of the longitudinal slip σ_x and the tire vertical load F_z, with two free parameters, tire-road friction coefficient μ and braking stiffness C_x determined by best-fit optimization.

$$F_x = \begin{cases} -C_x\sigma_x + \dfrac{C_x^2\sigma_x|\sigma_x|}{3\mu F_z} - \dfrac{(C_x\sigma_x)^3}{27(\mu F_z)^2} & if\ |\sigma_x| < \dfrac{3\mu F_z}{C_x} \\ -\mu F_z sign(\sigma_x) & else \end{cases} \quad (2.19)\ [105]$$

This relationship means that the coefficient of friction can be back-estimated from measured slip and tire forces. The simplicity of the brush model limits the accuracy of the estimate and additional equations are needed to account for the effect of other factors such as tire pressure. Furthermore, a significant fraction of the available friction must be utilized during the driving sequence in order to have a sufficient data spread to accurately estimate μ. Despite these limitations, Svendenius found that his estimator was at least able to distinguish between different types of surfaces such as asphalt, snow, and ice [105]. In summary, first principle-based methods can struggle to capture all of the relevant nonlinearities in tire-road friction estimation and require sufficient excitation of the input variables in order provide a usable estimate.

A future automotive safety system under development, active rollover prevention, requires the determination of a rollover index [91]. This index indicates the threat level of rollover in the current vehicle state and requires several state variables such as the height of the vehicle's center of gravity (COG) and the roll angle ϕ, which cannot be easily measured in real time. To address this, Rajamani et al. proposed advanced sensing methods for the roll angle and COG height using a dynamic observer and sensor fusion [91]. The roll angle was estimated both by combining the measurements from tilt angle and gyroscopic sensors and by combining the gyroscopic sensor with a dynamic observer. Using the dynamic observer reduced the sensor cost requirements, but increased the complexity of the algorithm and required additional knowledge of the suspension dynamics parameters. The COG was estimated using a recursive least-squares method to fit the roll dynamics equation, although a nonzero lateral acceleration was required. Reasonable estimates were provided with both algorithms, but there was room for improving both the accuracy and cost of the systems.

Acosta et al. comprehensively reviewed a large variety of methods for estimating tire longitudinal, lateral, vertical, and grip forces, including a comparison of their

different strengths and weaknesses [87]. Tire force estimation with virtual sensors is necessary since tire forces are critical for vehicle dynamics models and they cannot be measured economically with current technology. Various methods – first-principle, filters, observers, and neural networks – can be applied to estimate tire forces, and one of the key considerations is the applicable range and robustness of the method chosen. For example, under normal on-road driving conditions, lateral tire forces can be estimated by simple linear models, while in extreme driving conditions on loose surfaces, filters capable of handling uncertain data are more effective. Additionally, dynamic methods capable of capturing transient effects are required for vertical force estimation on rough surfaces [87]. Neural networks and data-driven approaches show promise in their ability to estimate tire behaviour in complex and nonlinear situations, although they require further development to compensate for training data limitations.

2.6 Chapter Summary

There is clearly a diverse array of techniques for modelling tire dynamics, tire-rim and tire-terrain interactions, and virtual sensing present in the literature, and they are continually being refined and improved upon in their efficiency, flexibility, accuracy, and robustness. A major trend that is visible is the shift in the type of models used and their relationship to measured data. At first, simple equations with few parameters, such as Bekker's terrain model, were used to model tire forces, terrains, and vehicle dynamics, and these were calibrated with relatively easy measurement methods. As time went on, the original equations were refined and replaced by more complex models with more parameters, such as Pacejka's Magic Formula, and the experiments required to calibrate the models became correspondingly more complicated. With the availability of high-power computers, numerical models of varying fidelity became popular, such as FEA tire models, enabling higher accuracy and flexibility, but also requiring even more data to build and calibrate, such as detailed tire material properties and dimensions. Furthermore, vehicle dynamics models used in virtual sensing became "smarter," using data-driven neural networks in addition to first-principle models. These networks could capture nonlinear

behaviour without needing physical parameters, but at the cost of higher computational requirements.

Therefore, to develop an effective virtual sensor for tire-rim slip on different terrains, three things are needed: a highly detailed and accurate tire model incorporating a tire-rim contact algorithm, a realistic and well-calibrated particle-based soil model, and a flexible but accurate data-driven virtual sensor. The development and integration of these models and algorithms will be the subject of future research.

Chapter 3. Tire-Rim Slip Modelling and Validation

In this chapter the development and validation of the FEA tire model for simulating tire-rim slip is presented. First, the structure of the existing RHD tire FEA model is described in section 3.1, followed by the modifications to the tire model and simulation settings to allow tire-rim slip in section 3.2. Next, the modified tire model is validated by comparing its static and dynamic behaviour against the original tire model and the manufacturer data for the RHD tire in section 3.3. Subsequently, the simulated frictional torque of the tire is compared with theoretical estimates in section 3.4. The results of the modelling and validation task are summarized in section 3.5.

3.1 FEA Tire Model

The majority of the FEA tire model used in the present research was originally created by Slade [43], who built on the work of Chae [21]. Many of the model details presented in this section (3.1) are sourced from Slade's Master's thesis. Figure 3.1 shows Slade's original tire model (a) and the present modified tire model (b). Visually, there is little to distinguish the two models except that the original tire has a gap in the rim, which was filled, and the slightly different position of the tire bead area under inflation. All of the material properties, element sizes, types, and numbers in the rest of the tire were unchanged for the modified tire model.

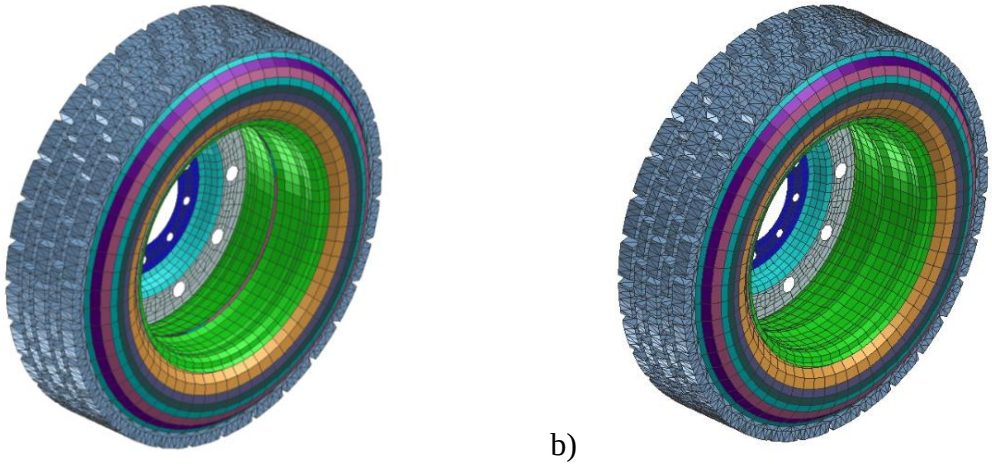

a) b)

Figure 3.1: Original and modified RHD tire FEA models. Different colours represent different parts.

3.1.1 Elements and Materials

The RHD tire model consisted of 13,820 elements, including solid, shell, multilayer membrane, and beam types. The dimensions and material properties were selected and calibrated using ESI Group's PAM-CRASH FEA software to match manufacturer data for a Goodyear RHD 315/80R22.5 radial truck tire [43]. Table 3.1 shows some basic specifications for the Goodyear tire.

Table 3.1: Specifications for Goodyear RHD 315/80R22.5 truck tire [43], [106]

Tread depth	27 mm	**Static loaded radius**	500 mm
Rim width	229 mm	**Minimum dual spacing**	351 mm
Rim mass	34.8 kg	**Speed rating**	120 km/h
Tire mass	72 kg	**Single inflation pressure**	850 kPa
Total wheel mass	106.8 kg	**Single max load**	39.2 kN
Section width	312 – 319 mm	**Dual inflation pressure**	800 kPa
Outer diameter	1076 – 1096 mm	**Dual max load**	32.9 kN

The tire was modelled by rotating a single-element-wide section through 60 6-degree increments to create an approximately round geometry, and the rim was created in a similar manner. Figure 3.2 shows a cross-section of the tire with the different parts and element types labelled. These parts are discussed in more detail in the following paragraphs.

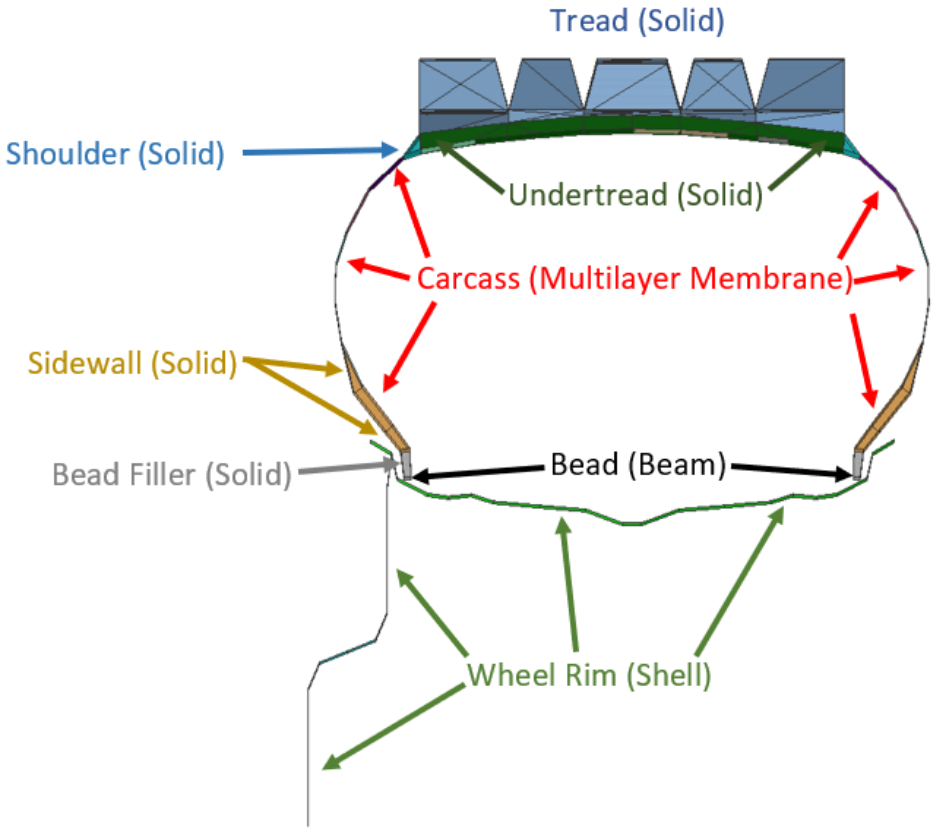

Figure 3.2: Cross-section of FEA tire model showing different parts and elements [107].

Carcass

The key design technique in the original RHD tire model was the tire carcass representation. In real life, the carcass consists of a flexible rubber matrix with a complex embedded network of stiff cords running in different angles and directions. In order to efficiently model this composite structure, a multilayer membrane material (type 150 in PAM-CRASH) was used [21]. Originally intended for woven components like seatbelts, the multilayer membrane is a thin shell element that behaves like a composite material with multiple layers that have different orthotropic directions, and stiffnesses. This type of material therefore allows efficient modelling of a rubber matrix with cords of different materials embedded at different angles. There are 14 different multilayer membrane parts, mirrored across the cross-section, with a total of 30 multilayer membrane elements appearing in Figure 3.2. Among

other differences, the thickness of the layers varies from a maximum of 27 mm near the bead to a minimum of 7 mm, in order to imitate the changing properties of the carcass throughout the tire in real life. The carcass elements create a continuous curved surface between the tire beads to which an inflation pressure load is later applied.

Bead

In a physical tire, the bead is a bundle of mostly continuous, stiff, high-tensile wires, usually made of steel. Due to this construction, they tend to undergo mainly tensile and twisting loads, rather than shear loads. Therefore, it was chosen to use a set of stiff beam elements to model the bead, which consumes minimal computation resources compared to using solid elements as some other more detailed bead studies have done [25], [31], [33], [39]. It is important to note that the nodes on the bead elements are coincident with the nodes on the innermost edges of both the carcass membrane elements and the bead filler elements, hence there is a single sharp edge of nodes at the inside of the bead. This has implications for modelling the tire-rim contact, as discussed later on.

Wheel Rim

The main contribution of the wheel rim is transferring forces and torques from the wheel hub – in this case represented by a rigid body center of gravity (COG) node – to the tire-rim contact. Since the wheel rim was subjected to a rigid body constraint, the deformation and specific behaviour of the wheel rim was not important, therefore null shell elements were used with a generic steel stiffness of 200 GPa, and a density of 7.77 g/cm^3 was chosen to match the weight of the real-life rim. All elements in the rim had the same type and material properties, and were part of the same rigid body constraint.

Solid Element Areas

Since a real-life tire has substantially thick parts of the carcass, such as the tread, that do not deform as easily as a thin membrane or shell, thick, solid tetrahedral and hexahedral elements were used in 5 key areas – bead filler, sidewall, shoulder,

undertread, and tread – to ensure the tire model behaved realistically. Hexahedral solid elements were mainly used, except for the tread, where tetrahedral elements were necessary to achieve the more complex geometry. All of the solid elements used a Mooney-Rivlin hyperelastic material model to capture the hyperelastic deformation behaviour of rubber. The Mooney-Rivlin rubber model is presented in Eq. 3.1 [48], and the coefficient values used are summarized in Table 3.2. The rubber was assumed to be nearly incompressible, thus the elastic volume ratio J^{el} was approximated as 1, and the third term in Eq. 3.1 went to zero [108]. Density and Poisson's ratio information was also needed to complete the material model.

$$U = C_{10}(I_1 - 3) + C_{01}(I_2 - 3) + \frac{1}{D_1}(J^{el} - 1)^2 \tag{3.1}$$

Table 3.2: Material model parameters for solid elements

	Parameter	C_{10}	C_{01}	ρ	Poisson's ratio
Part	**Unit**	MPa	MPa	g/cm^3	none
Bead filler	Material #21	0.392	1.268	0.882	0.49
Sidewall	Material #22	0.392	1.268	0.881	0.499
Shoulder	Material #25	0.67	2.46	0.6933	0.49
Undertread	Material #26	0.51	1.86	0.5962	0.49
Tread	Material #27	0.67	2.46	0.6933	0.49

Road

In order to run a complete simulation, a surface was also needed for the tire to roll on. For the hard surface simulations, a road of null shell elements was used. Since the road was treated as a rigid body and fixed in place, its deformation behaviour was unimportant and default material values were used. The same type of null shell elements and material were used to create the soil boxes for the soil calibration and tire-rim slip on soil simulations.

3.1.2 Loads and Constraints

A variety of loads and constraints were applied to the simulation to limit and control the motion of the tire for realistic results. Figure 3.3 shows some of the key loads and constraints.

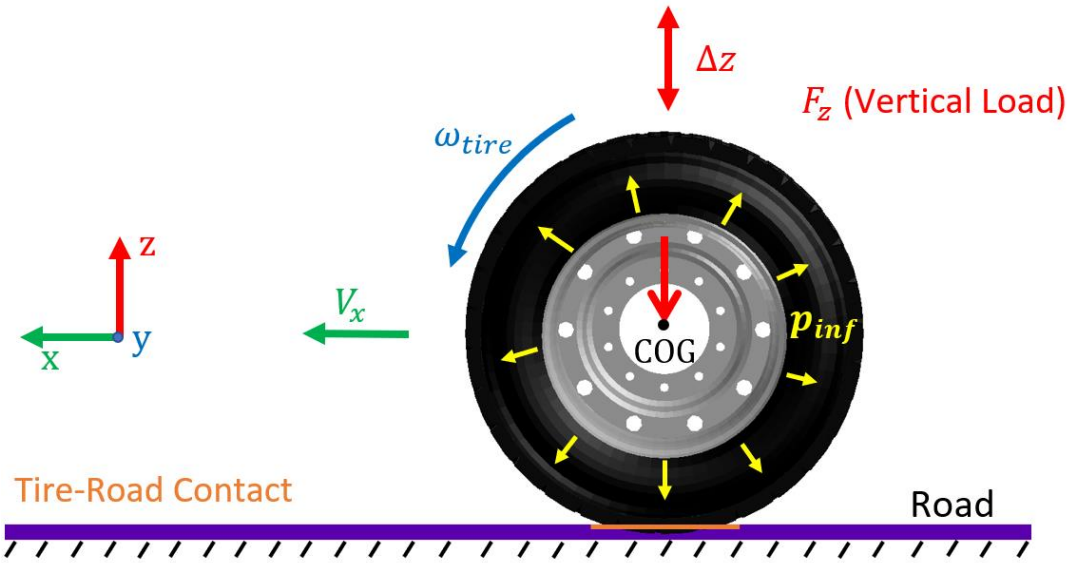

Figure 3.3: Key loads and constraints for FEA tire model [107].

In a typical dual configuration, the Goodyear RHD 315/80R22.5 truck tire is rated for 32.9 kN of vertical load at a cold inflation pressure of 800 kPa and a maximum speed of 120 km/h. At lower speeds typical for off-road use, the load rating increases to 41.1 kN at an inflation pressure of 904 kPa and a maximum speed of 30 km/h. These ratings set the approximate limits of the FEA model loads.

Rigid Body Constraints

The wheel rim, including all 4 parts, was treated as a rigid body with a COG node at the center. This COG node had the following loads (vertical load, displacement constraints, longitudinal wheel speed) applied to it, and was used to track the motion of the wheel. The original tire model included the nodes at the bead as part of the rigid body in order to create a rigid tire-rim connection, while the modified tire model removed them from the rigid body definition to allow for slip at the tire-rim contact. The road and soil boxes were also treated as rigid bodies.

Displacement Constraints

The wheel COG was restricted from translation in the y-direction, and rotation about the x- and z-axes, while being allowed to translate in the x-and z-directions and rotate about the y-axis (Figure 3.3). The constraints were slightly different for the validation tests described in Chapter 4. The roads and soil boxes were completely fixed with zero degrees of freedom.

Gravity

All parts in the simulation were subject to a gravitational field of 9.81 m/s^2 in the negative z-direction during the entire simulation.

Damping

Due to the large forces and accelerations applied in the initial time steps, a global mass-proportional nodal damping factor of 100 was applied to all nodes in the simulation until 0.1 seconds. This damping reduced unwanted oscillation in the results as well as the steady state settling time.

Tire rubber also has viscous damping behaviour, which causes internal speed-dependent friction forces. This behaviour was modelled by applying additional mass-proportional nodal damping to 4 sections of the carcass in the sidewall area, where the tire deformation would be greatest. The sidewall damping was applied after the global damping stopped, and had a significant effect on the tire behaviour only at higher speeds. The magnitude of the sidewall nodal damping factor was estimated from the tire model's first vertical mode of vibration, after Chae [21]. Table 3.3 lists the sidewall nodal damping factors for each inflation pressure used in the present research. These values were based on previous research [109], they were not based on the drum-cleat tests performed during this thesis. As a side note, the particular values for inflation pressure and vertical load used in this thesis were chosen by converting from round U.S. units. For example, 55 psi became 276 kPa, and 9000 lbs became 41 kN. SI and SI-derived units are used throughout the thesis for consistency.

Table 3.3: Sidewall nodal damping factors

Inflation Pressure (kPa)	276	379	482	586	758	896
Nodal Damping Factor	2.67	2.90	3.10	3.30	3.60	3.74

Inflation Pressure

A constant surface pressure load was applied to the inside of the carcass elements to imitate the air pressure in a pneumatic tire. The surface pressure load was applied at the same time as the vertical load, 0.095 seconds before the longitudinal wheel speed load in order to give the tire time to inflate against the rim and settle. The bead parts were inside the rim at the start of the simulation, therefore only an inflation pressure was required to mount the tire.

The interior of a real pneumatic tire is a sealed volume, which means the air pressure also depends on the tire volume and temperature. However, the effect of a volume change is minimal since the tire carcass rubber is relatively stiff, and temperature effects were ignored since they were not part of the scope of the research. The air pressure also applies a load to the surface of the rim within the tire volume, but since the rim was treated as a rigid body due to its high stiffness and its stress levels were not of interest, the air pressure effect was simplified to a constant surface pressure load on the inside of the carcass. A range of different inflation pressures were used (see Table 3.3), with a maximum of 896 kPa following the manufacturer's guidelines, as well as values as low as 276 kPa representing a very low operating pressure possible for off-road driving.

Vertical Load

To simulate the vertical load transferred from the truck to the tire-wheel assembly, a concentrated force was applied to the wheel COG node in the negative z-direction. The magnitudes of the vertical load — 13 kN, 27 kN, or 41 kN — were selected within the manufacturer guidelines following previous research [1], [110], and they were applied after the inflation pressure, remaining constant for the rest of the simulation.

Longitudinal Wheel Speed

Since the RHD tire is a driven-axle truck tire, the longitudinal wheel speed in the x-direction was controlled via a fixed angular velocity constraint (ω_{tire}) applied to the wheel's COG node. This boundary condition resulted in a varying torque applied about the y-axis to ensure the constant angular velocity, the same as a real truck applies torque to the drive wheels to maintain a constant speed. The required angular velocity was computed using Eq. 3.2 below:

$$\omega_{tire} = \frac{V_x}{3.6 r_0} \tag{3.2}$$

Where ω_{tire} is the required angular velocity in rad/s, V_x is the desired longitudinal wheel speed in km/h, and r_0 is the nominal radius of the tire in m. r_0 has a value of 0.546 m for the Goodyear RHD 315/80R22.5 truck tire [43], [106]. For example, a longitudinal wheel speed of 10 km/h requires an angular velocity of 5.0875 rad/s to be applied to the wheel COG node as shown by the calculation below.

$$\omega_{tire} = \frac{V_x}{3.6 r_0} = \frac{10}{3.6(0.546)} = 5.0875\ rad/s$$

Longitudinal wheel speeds used in the tire-rim slip simulations ranged from a low of 5 km/h for slow off-road driving to a maximum speed of 60 km/h. The actual longitudinal speed of the simulated tire depended on the rolling radius (r_{roll}) of the tire, a dynamic variable influenced by the inflation pressure and vertical load.

Tire-Road Contact

The final key component of the basic FEA tire model was the tire-road contact definition, which prevented the tire nodes from passing through the road and allowed normal and tangential forces to be transmitted between them. There are a wide variety of contact algorithms that have been developed for FEA simulations, however the present research was limited to the types available in PAM-CRASH.

A common type of contact algorithm is the penalty method [110]. The basic idea behind the penalty method is that the magnitude of the contact forces depends on the

distance between the contacting nodes and elements, and a smaller distance results in a higher penalty factor and contact forces. This usually prevents the surfaces from passing through each other, as long as the surfaces are not too coarse and the time-step is small enough relative to the speed of the contacting bodies.

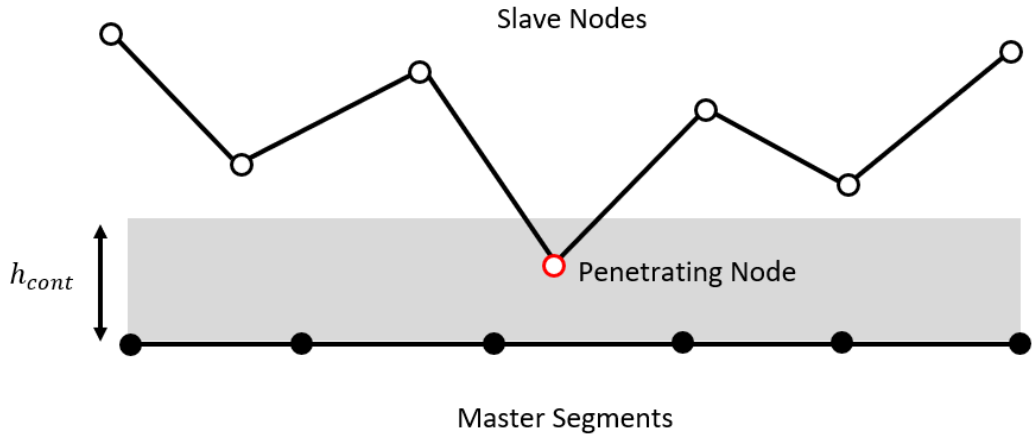

Figure 3.4: Example of penalty-based contact with slave nodes and master segments.

The type of contact definition used in PAM-CRASH for the tire-road contact was a type 34 non-symmetric node-to-segment contact with edge treatment [110]. This contact type performs a bucket search between the nodes in the slave entity definition and the segments (lines/surfaces between nodes) in the master entity definition. Any slave node that falls within the contact thickness h_{cont} of the master segments is considered to be penetrating, and a normal force F_n is applied proportional to the depth of penetration. Particularly important for the tire-road interaction is the frictional contact force. A tangential frictional force F_t is thus applied to penetrating slave nodes using a simple Coulomb friction model (Eq. 3.3) with coefficient of friction μ.

$$F_t = \mu F_n \tag{3.3}$$

The edge treatment description means that the algorithm uses a reduced radius search space around free edges instead of an unrealistically protruding constant radius one. The non-symmetric designation means that the slave and master entities are treated differently, since the algorithm searches for slave *nodes* penetrating master *segments*, not the other way around. This works best if the slave surface is pointier than the

master surface. Another contact type, type-33, is a symmetric type of contact, which means it searches for both slave node penetration *and* master node penetration. This method is more reliable at preventing surfaces from passing through each other, but requires almost twice the computation time. Therefore, the type 34 contact was the preferred contact type because of the available friction force, edge treatment, and reduced computational requirements.

Figure 3.5 shows the two entities involved the type 34 tire-road contact definition. On a hard surface, only the outermost tread elements come into contact with the road, therefore the rest of the tire and wheel parts were excluded from the contact definition to reduce the computational load. The tread was defined as the slave entity, and the road as the master entity, which meant the algorithm searched for tire nodes penetrating the road segments. Key parameters were a contact thickness h_{cont} of 5 mm and a coefficient of friction of 0.8 for a rubber tire on hard asphalt or concrete following previous research [21], [43]. Note that the tire-road coefficient of friction was artificially increased to 1.0 for the tire-rim slip simulations.

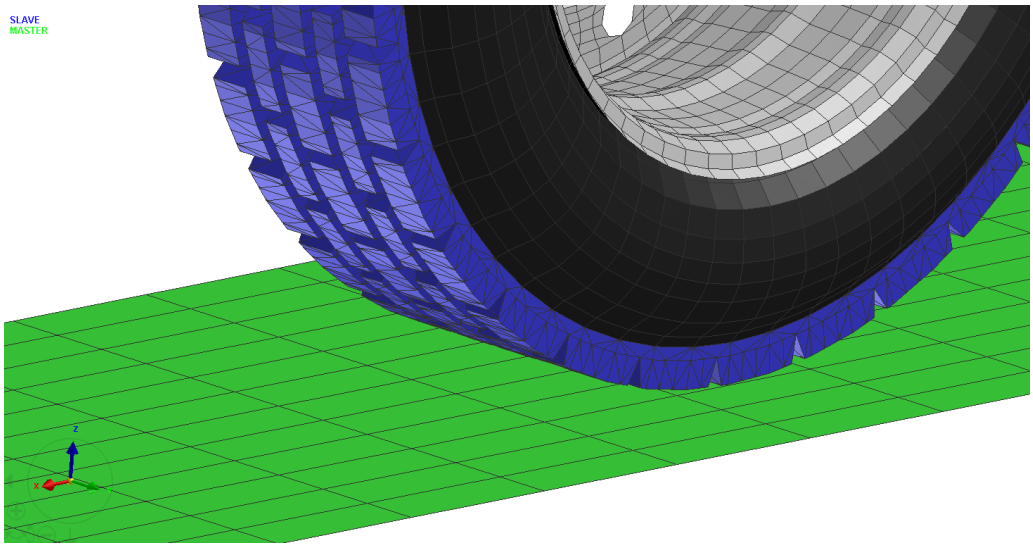

Figure 3.5: Tire-road contact definition showing slave (blue) and master (green) entities.

3.1.3 General Simulation Methods

There are many options and general parameters for running simulations, some of which are described in this section. The 2013 version of the 64-bit PAM-CRASH

explicit solver was used with single precision accuracy and shared-memory parallel processing. The unit system was metric, using mm, ton, second, and Kelvin as the base units. Often the units were converted to more convenient values such as kNm or km/h for presenting the results.

Processing was done at different times on computers with different hardware. This was not expected to significantly effect the results, because running the same simulation on different computers produced negligible differences between the results in the vast majority of cases, and all of the simulations in a particular category (e.g. tire-rim slip on a hard surface) were run on the same computer. The simulations were run for 1.5-2.0 seconds with an initial time-step of 1e-6 seconds for simulations involving SPH elements and 0.001 seconds for every other simulation to reduce the computational time required. Subsequently, the time-step was changed dynamically by the solver. Nodal and element output data was collected every 0.0001 to 0.01 seconds depending on the time-step size. After the simulations were complete, the results data was exported to Excel and averaged over the length of time that each results variable (e.g. nodal velocity) was approximately at steady-state. This means that the results of the research apply generally to steady-state behaviour, not transient conditions. Adaptation to transient conditions could be an area for future research.

3.2 Tire-Rim Slip Measurement

This section describes the tire-rim slip measurement process for a hard surface simulation as presented in Chapter 5.1. The process was virtually identical for the tire rim-slip simulations on soil, except that the tire contacted the soil SPH elements instead, and the tire speed sensor was attached to back edge of the fixed soil box. Some time-step values and load times were also changed to allow for accurate SPH computations.

3.2.1 Tire Model Modification

The first modification done to the original RHD truck tire model (Figure 3.1a) was to fill in the gap in the rim as shown in Figure 3.6. After adding the new elements, the density of the rim material was decreased slightly to maintain the same total mass. The rim was filled in order to facilitate the new tire-rim contact definition and prevent

any carcass elements from slipping through the previous gap in the rim. The nodes at the bead were also removed from the rim's rigid body definition to allow the relative motion and rotation required for tire-rim slip.

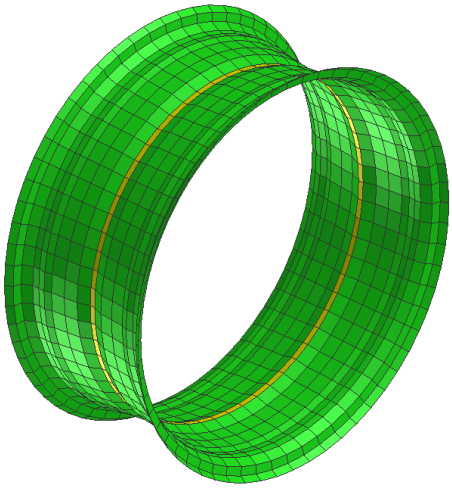

Figure 3.6: Modified RHD tire rim with gap-filling elements shown in yellow.

Next, a new contact definition was created between the carcass elements and the wheel rim. Figure 3.7 shows a single-element wide section of the tire and rim with the major contacting elements identified. The tire side of the contact included the bead beam elements, the two carcass membrane elements closest to the bead, and two solid rubber bead filler (gray) and the sidewall (blue) parts. The entire outside part of the rim (green) was included as the other side of the contact definition to ensure the tire did not pass through the rim.

Different parameters of the contact definition such as the type, contact thickness h_{cont}, and inflation time were varied to find a combination that inflated the tire in the shortest amount of time without causing the tire elements to pass through the rim at the tire-rim contact. It was found that a type-33 symmetric node-to-segment contact with a contact thickness of 0.5 mm and an inflation time of 0.095 seconds (95 time-steps) provided good performance.

As described in Chapter 2, there are multiple ways to model the friction between the tire and rim. The same constant friction Coulomb model was used as for the tire-road contact, but this time μ was treated as a parameter varied from 0.05 to 0.9. This was

done because it is difficult to obtain a representative friction value due to the large number of influencing factors such as bead lubrication, rim material, rubber material, temperature, inflation pressure, tire-rim interference, and manufacturing/installation defects [8], [22], [111].

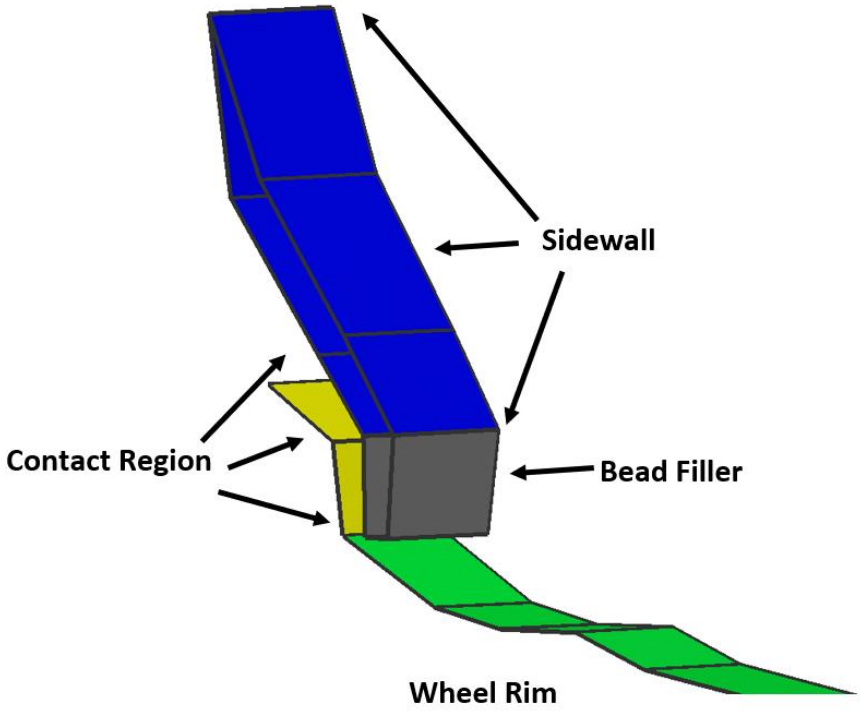

Figure 3.7: Cross-sectional view of major elements involved in the tire-rim contact. The main contact region is highlighted in yellow [107].

3.2.2 Tire-Rim Slip Test Simulation

Now that the tire model was modified to allow relative motion between the tire and rim, the next step was to set up simulation conditions where tire-rim slip would occur. These were based on an accepted standard for tire-rim slip measurement, ASTM F2803 [55]. In ASTM F2803, the vehicle's tires are inflated to their nominal cold inflation pressure and loaded at their corresponding maximum vertical load. For the Goodyear RHD tire used in this research, that equates to an inflation pressure of 896 kPa and a vertical load of 41 kN.

The vehicle is attached to a weighted trailer dynamometer designed to apply a specified backwards drawbar load to the vehicle's hitch [112]. The drawbar load

should be equal to 60% tractive effort, or 60% of the total weight of the vehicle. For example, a 100 kN truck would have a 60% tractive effort drawbar load of 60 kN. If the truck had 6 driven tires and the weight was evenly distributed, there would be a drawbar force of 10 kN per tire. Once the trailer is attached, the vehicle is driven for 15 minutes, and the circumferential distance the tire being tested has slipped around the rim is measured. This test only applies to driven tires, like the RHD tire, since a free-rolling tire has negligible torque transmitted between the tire and rim that could cause tire-rim slip.

There are several reasons, explained in this and following sections, that ASTM F2803 could not be replicated exactly, but it was used as a reference point for simulating tire-rim slip for a single tire. Figure 3.8 shows the loads and entities additional to those described in section 3.1 that were applied to the tire and wheel for the tire-rim slip simulation. These included the drawbar load, wheel speed sensor, tire-rim contact, and the rigid body for measuring ω_{tire}. The drawbar load was a concentrated load applied in the negative x-direction to the COG of the rim with a magnitude proportional to the vertical load on the tire. In most of the test cases, these two loads were set to default values of 41 kN for the vertical load and 60% or 24.6 kN for the drawbar load based on the loads used in ASTM F2803.

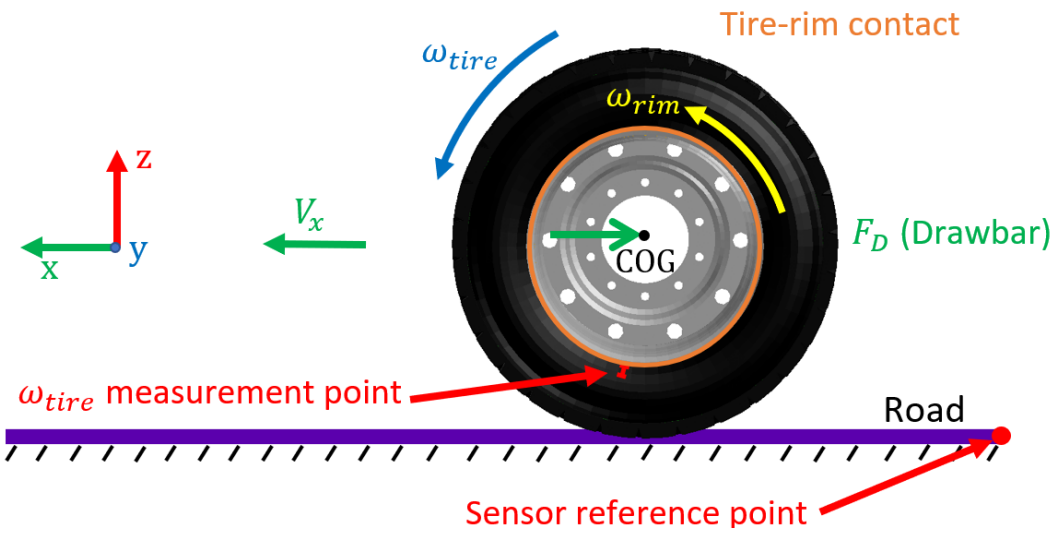

Figure 3.8: Drawbar load and ω_{tire} measurement for tire-rim slip simulation [107].

Another change to the model was the addition of a wheel speed sensor, to ensure realistic application of the drawbar load. In real-life, the resistance of friction-based loads, such as those generated by pulling a weighted trailer, drops to zero when the speed of the vehicle goes to zero. To make the concentrated drawbar load in the simulation behave this way, a sensor connected to the wheel COG and a reference point on the road was used to measure the relative linear speed of the wheel (V_x) within the simulation. Once this speed dropped below a specified threshold of 10 mm/s or 0.036 km/h, the drawbar load was turned off by the sensor. A non-zero threshold was used to avoid measurement precision errors and overshoot. This caused a simple control effect on the drawbar load, where the load was turned off when the wheel speed became very small and then turned on again when the wheel speed increased. The resulting behaviour of the wheel was that its speed dropped nearly to zero when the tire steadily slipped on the rim, just as would happen in real life.

3.2.3 Quantification of Tire-Rim Slip

Additions were also made to the basic tire model to quantify the tire-rim slip. In physical tests, such as ASTM F2803, the tire-rim slip is measured by making parallel marks on the tire and rim before the test and measuring the circumferential distance between them after driving for a specified length of time of 15 minutes. Some drawbacks of this method are that the circumferential distance depends on the radius of the tire and on how long the tire was driven. Since it was desirable to have a more generalizable method of measuring tire-rim slip that could be done with a simulation time of only a few seconds, a measurement method based on the relative angular velocity of the tire and rim was developed.

There is a well-known quantity called the longitudinal slip i for driven tires which has the following formulation [27]:

$$i = \left(1 - \frac{V_x}{r_{roll}\omega_{tire}}\right) \times 100\% \tag{3.4}$$

A similar quantity called rim-slip i_{rim} measuring the relative rate of angular tire-rim slip is proposed in Eqs. 3.5 and 3.6 below, where ω_{tire} and ω_{rim} are the angular velocities of the tire and rim about the wheel center.

accelerating $$i_{rim} = \left(1 - \frac{\omega_{tire}}{\omega_{rim}}\right) \times 100\% \tag{3.5}$$

braking $$i_{rim} = \left(1 - \frac{\omega_{rim}}{\omega_{tire}}\right) \times 100\% \tag{3.6}$$

With this definition, i_{rim} has a value of 0% when the tire and rim are both stationary or are both rotating in the same direction with the same angular velocity. A value of 100% occurs when the rim is rotating but the tire is stationary (accelerating), or when the rim is stationary while the tire is rotating (braking). This measurement of tire-rim slip is independent of the diameter of the wheel, the speed at which the whole wheel is travelling, and the length of time that it rotates. This allows slip rates to be compared easily between different wheels and driving conditions, and may also allow estimation of the power dissipated by friction at the tire-rim interface.

Measuring the angular velocity of the rim was straightforward, since ω_{rim} was an input to the simulation. In order to measure ω_{tire}, a small 2-node rigid body was added to part of the sidewall as shown in Figure 3.8 to provide a point of reference for self-rotation of the tire. Then, the angle of rotation time histories of both the rim COG (θ_{rim}) and the tire reference point (θ_{tire}) were extracted and imported into Excel (Figure 3.9). Excel's built-in function was used to find a first-order line of best fit to calculate the slope of the θ_{tire} time history between 0.5 and 1.5 seconds, after the wheel reached its full rotation speed. This slope was the angular velocity of the tire. In a very few simulations, the steady-state condition was lost as the mesh near the bead crumpled and re-engaged with the rim (Figure 3.9). In this case, the slope was only calculated for the steady-state portion of the results and the tire was assumed to have slipped fully. Then, i_{rim} was calculated using Eq. 3.4, since the drive torque was applied to accelerate the rim in the simulation. i_{rim} was calculated for each set of simulation parameters in the testing described in later chapters and used as the comparison data point.

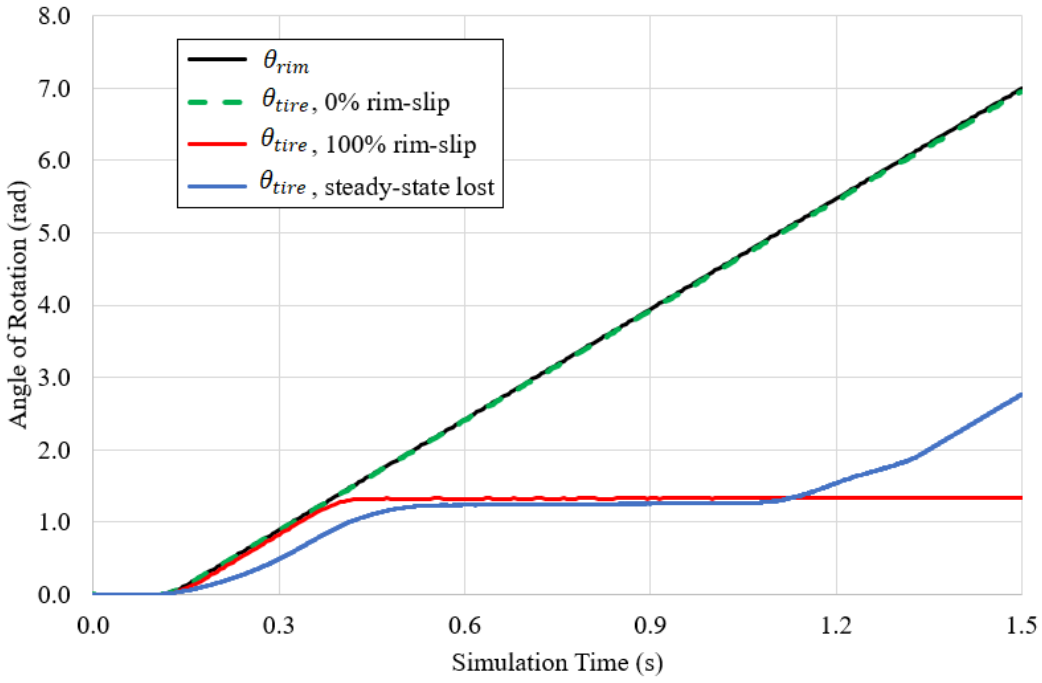

Figure 3.9: Calculation of i_{rim} from sample θ_{rim} and θ_{tire} time histories with 0% rim-slip, 100% rim-slip, and with a loss of steady-state. Note that the time-history with the loss of steady-state was scaled down from a 60 km/h simulation.

3.3 Tire Model Validation

Once the modifications to the RHD tire FEA model for simulating tire-rim slip were completed, a series of static and dynamic simulated tests were conducted to ensure the modifications did not affect the basic accuracy of the tire model compared to the original tire model and the real RHD tire. The modified tire model was subjected to two static (footprint and vertical stiffness) and two dynamic (drum-cleat and cornering) simulated tests, and the results were compared against both the original tire model and Goodyear's test data. This set of tests was based on previous research [1], [2], [21], [43] for validating tire FEA models.

3.3.1 Footprint Test

The first validation test was a static footprint test. In this test, the tire was inflated to 759 kPa and 3 different loads were applied (13, 27, and 41 kN) to bring the tire into contact with the hard road surface. Once the simulation reached a steady state, the footprint area was estimated based on a contour plot of the nodal displacement of the

tire (Figure 3.10). Nodes that were sufficiently close to the road (located at -520 mm) were included in the footprint area. This simulation and estimation process was repeated for all 3 loads for both the original and modified FEA tire models and the results are listed in Table 3.4.

Figure 3.10: Estimation of footprint area (yellow rectangle) for modified tire model at 13 kN vertical load.

Table 3.4: Estimated footprint areas (cm^2) for RHD tire and FEA models.

Vertical Load (kN)	Original FEA	Modified FEA	Goodyear Data
13	292.47	291.79	284.82
27	408.96	409.77	439.06
41	533.91	533.18	600.04

A comparison of the footprint areas in Table 3.4 shows that there is less than 1 cm^2 difference between the two FEA models, therefore we can conclude that adding the tire-rim contact had negligible effect on the static footprint area. Table 3.4 also includes data from the tire manufacturer Goodyear for a similar 3-Groove 295/75R22.5 truck tire [43]. This measured data, compared visually against the simulated footprint areas in Figure 3.11, shows a steeper slope, which is likely due to the difference in tread design between the 3-Groove and RHD tires. However,

based on the similar values and increasing trend, it can be concluded that the modified FEA model for tire-rim slip simulations is a good representation of the static footprint characteristics of the RHD tire.

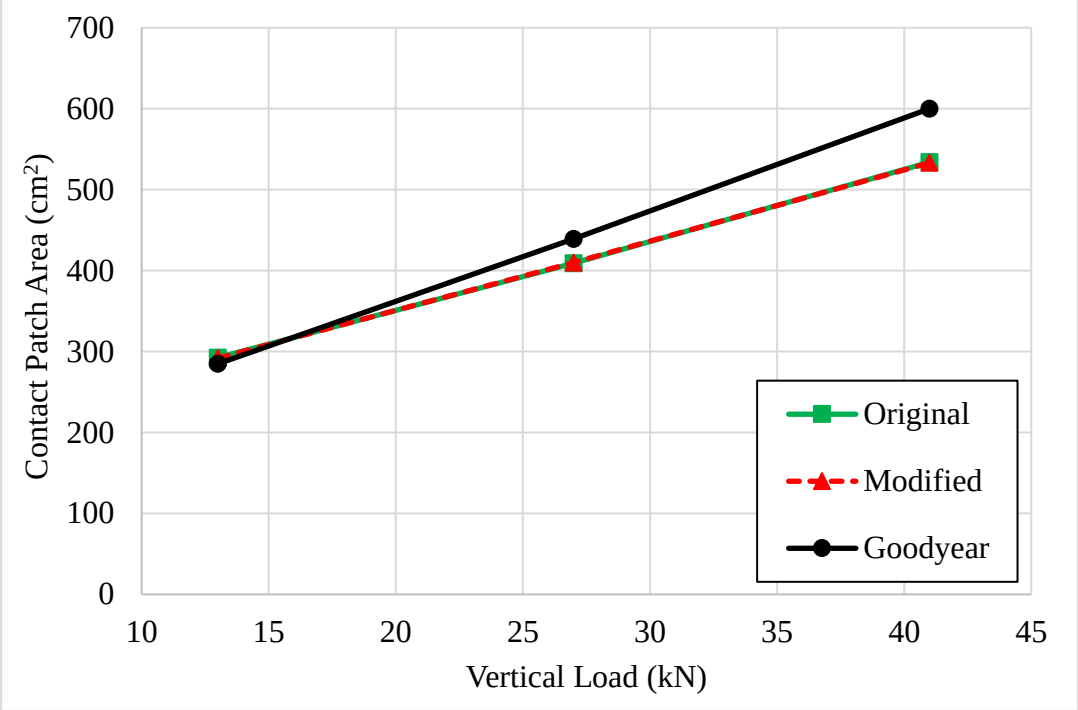

Figure 3.11: Comparison of footprint area between FEA tire models and Goodyear data [107].

3.3.2 Vertical Stiffness Test

The second static validation test performed was a vertical stiffness test to measure the deflection of the tire carcass under load (Figure 3.12). Vertical stiffness tests are usually performed by either compressing the tire carcass directly with an actuator [113], or using an actuator to apply a controlled load to the rim [17], [45]. Since the tests were performed in a simulated environment, the tire models had a ramp vertical load applied to their COG node, and then the vertical displacement of that COG node was measured over time. The vertical load was increased slowly from 0 to 41 kN over a period of 2.0 seconds to minimize acceleration and oscillation effects. Tests were done at two inflation pressures, 586 kPa and 896 kPa, for both the original and the modified FEA models, and the resulting load-deflection curves are compared in

Figure 3.13 with tire deflection data from Goodyear for a representative 315/80R22.5 truck tire [43].

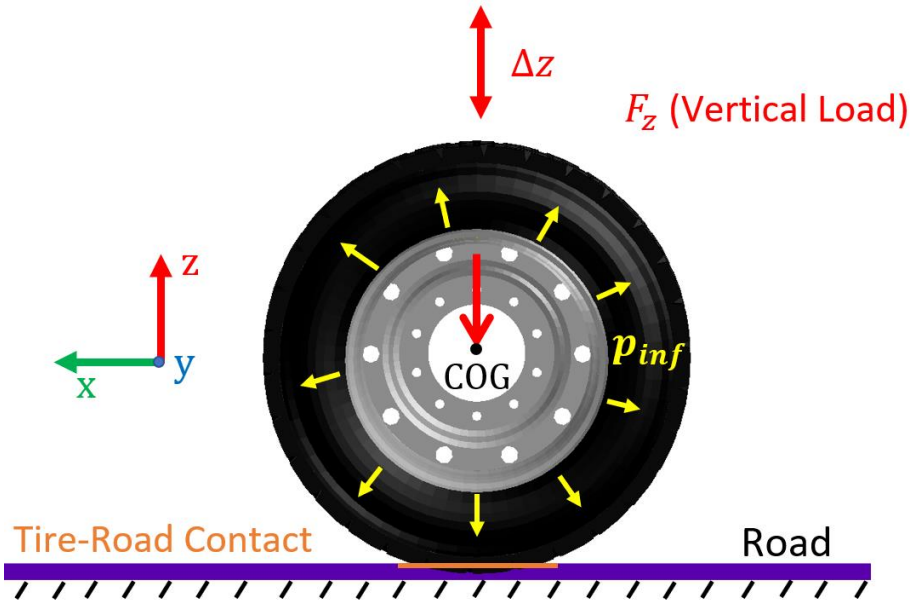

Figure 3.12: Simulated tire vertical stiffness test.

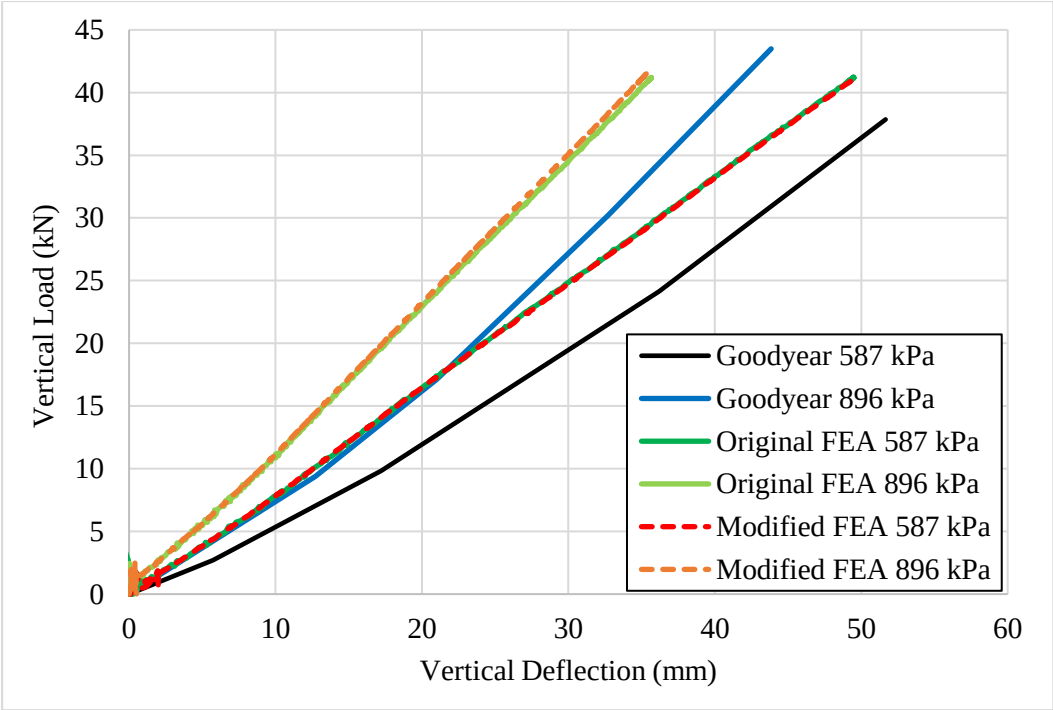

Figure 3.13: Load-deflection curves for modified FEA model (dashed), original FEA model, and Goodyear truck tire at 587 kPa and 896 kPa inflation pressures [107].

There is a high degree of agreement in Figure 3.13 between the original and modified FEA tire models, as the two curves are almost superimposed. This indicates that adding the tire-rim contact did not affect the components of the tire that influence its vertical stiffness characteristics. However, there appears to be a significant difference in that the Goodyear data shows a curving trend with a generally shallower slope compared to the FEA results. This likely occurs due to linear simplifications within the FEA model and limitations of the Mooney-Rivlin rubber material, while the physical tests can capture the full nonlinearity of the real tire.

In addition, calculating the average vertical stiffness (slope of the curves in Figure 3.13) shows a much higher degree of similarity between the FEA results and Goodyear data, with a relative difference of less than 10% (Table 3.5). Based on this average vertical stiffness comparison, it was concluded that the original and modified FEA models provided acceptable stand-ins for the physical RHD tire, as long as nonlinear tire deflection is not important.

Table 3.5: Comparison of average vertical tire stiffnesses [107]

Inflation Pressure (kPa)	**Average Stiffness (10^6 N/m)**		**% Difference**
	Goodyear Data	Modified FEA Tire	
587	778.49	836.78	7.49
896	1079.8	1170.4	8.39

3.3.3 Drum-Cleat Test

The third validation test done was a dynamic drum-cleat test to characterize the vibratory behaviour of the FEA tire model. The drum-cleat test simulation shown in Figure 3.14 was based on previous work [21]. Both the original and the modified FEA tire models were put through the drum-cleat simulations at a range of inflation pressures, and their resulting horizontal and vertical vibration modes were compared to determine if the modifications had any effect. Tire vibration analyses from the literature were also benchmarked.

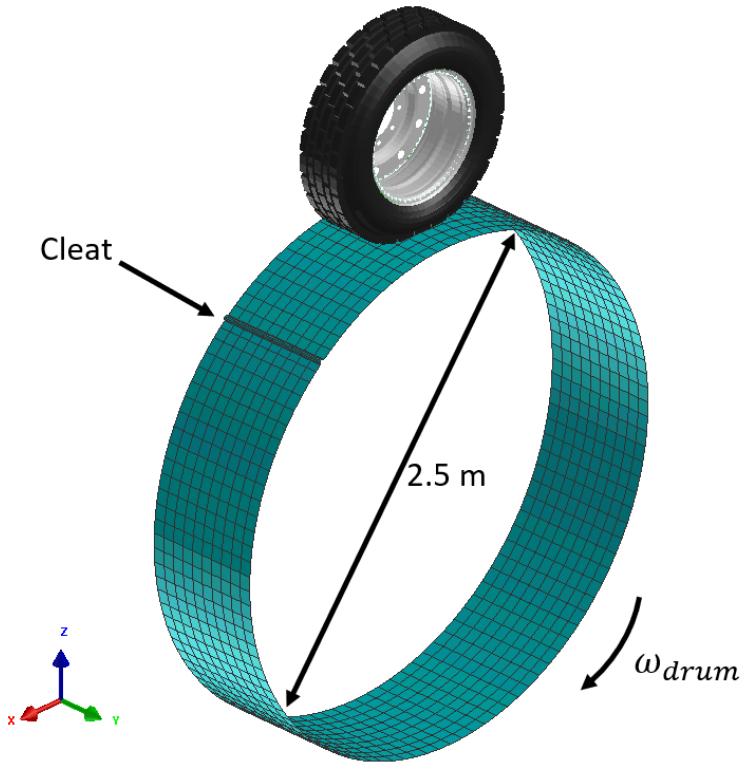

Figure 3.14: Drum-cleat simulation setup for FEA tire model.

The tire was placed on a 2.5 m diameter drum made of null shell elements with single 15 mm radius cleat. The drum was treated as a rigid body, and was only allowed to rotate about its y-axis with a specified angular velocity ω_{drum} of 11.1 rad/s, equivalent to a 50 km/h longitudinal speed for the tire. This angular speed resulted in an excitation frequency for the tire of 1.77 Hz, for a total of 3 complete excitations during the 2.0 seconds of simulation time. The original and modified FEA tire models used for the drum-cleat test were mostly identical to those described previously in sections 3.1 and 3.2. However, a smoothed node-to-segment contact definition (type 44 in PAM-CRASH), with a friction coefficient of 0.6 was applied between the tire and drum to minimize any vibratory effect from the roughness of the discretized drum.

Another important change for the drum-cleat test was in the application of the displacement constraints to the tire COG node. Initially, during the first 0.1 seconds of the simulation time when the 41 kN vertical load, inflation pressure, and other initial loads were applied, the constraints on the COG node were the same as those

described in section 3.1. This allowed the tire to settle vertically. After the first 0.1 seconds, however, a time-triggered sensor switched to a second set of boundary conditions that prevent the tire COG node from translating in the vertical z-direction. This ensured that the excitation of the cleat only resulted in local vibration of the tire carcass, not vertical bouncing of the whole tire.

The vibration behaviour was characterized by the first vertical and horizontal vibratory modes of the tire (Figure 3.15). These modes were determined by extracting the vertical and horizontal reaction forces at the constrained tire COG node and then performing an amplitude-based Fast Fourier Transform (FFT) to determine the approximate magnitudes of the different frequencies contained within the reaction force signals (Figure 3.16).

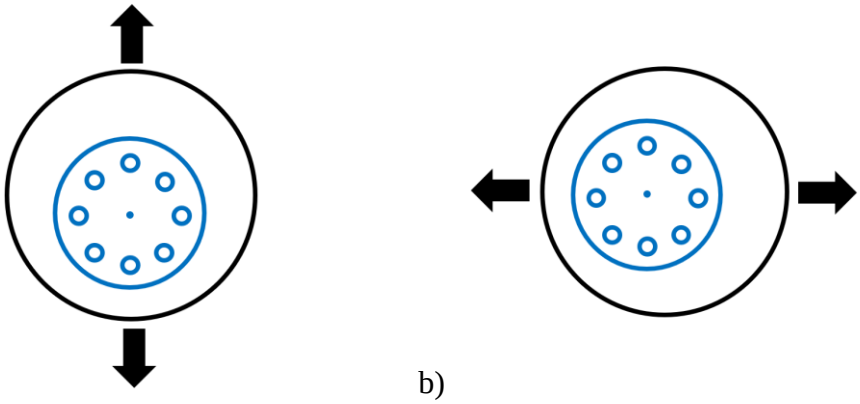

a) b)

Figure 3.15: 1st vibration modes of a tire: a) vertical and b) horizontal.

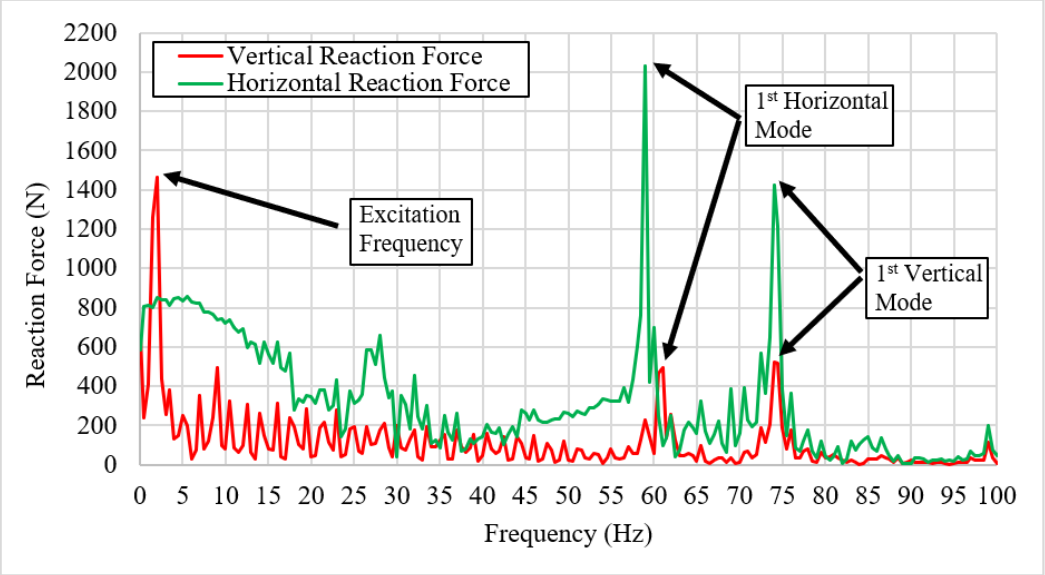

Figure 3.16: Sample FFT results for the modified FEA tire model at 758 kPa inflation pressure, including both vertical (red) and longitudinal (green) reaction forces.

The range of frequencies analyzed was limited to 100 Hz, since only the first modes of vibration were of interest. Higher-frequency modes are of little practical interest, since after the first vibration mode is reached, tires are usually destroyed by standing waves [27]. The low-frequency peak in Figure 3.16 around 2 Hz is caused by the 1.77 Hz excitation frequency applied to the tire. Interestingly, the FFTs of both the vertical and horizontal reaction forces showed two peaks, around 60 Hz and 74 Hz. The similarity of the peak frequencies can be explained by the similarity of the vertical and horizontal modal shapes (Figure 3.15), as the type of vibration is the same, and it is only the direction that differs [113]. Since it is well-known in the literature that the vertical mode of the tire is at a higher frequency than the horizontal mode [49], it was assumed that the higher pair of peaks in Figure 3.16 represented the vertical mode, while the lower pair represented the horizontal mode. The lower two peaks differed by up to 3 Hz at 896 kPa, in those cases an average between the two peaks was used.

Figure 3.17 shows the estimated first vertical and horizontal vibration modes for the original and modified FEA tire models, for a range of inflation pressures from 276 kPa to 896 kPa. Other commonly varied simulation parameters such as vertical load

and longitudinal wheel speed are known to have negligible influence on the vibration modes [109] and were not considered.

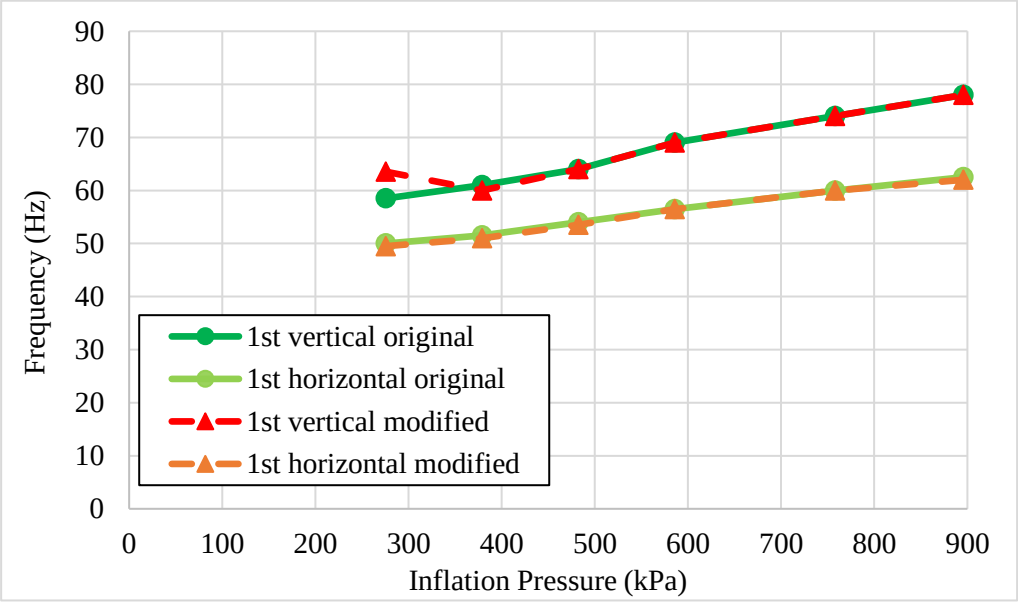

Figure 3.17: Comparison of vibration modes for original and modified FEA tire models.

Generally, the determined vibration modes were as expected, similar to previous research on the same tire model [1], [2], [43], [109]. There is a small, but consistent increasing effect of inflation pressure on the vibration mode across all the curves in Figure 3.17, and the vertical mode is consistently higher than the horizontal mode. However, there was one outlier for the modified FEA tire model's vertical mode at 276 kPa, which was larger than expected at about 63.5 Hz. The horizontal reaction force FFT was atypical, with a series of low-magnitude peaks and a single high magnitude peak at 63.5 Hz, none of which was close to the 45-50 Hz peaks on the vertical reaction force FFT. The simulation was repeated several times to check for computation errors, with similar results. It is possible that the combination of low tire pressure and the added tire-rim contact was responsible for this outlier, since adding the tire-rim contact gave more degrees of freedom to the nodes at the bead. The low tire pressure then allowed higher amplitudes of vibration for these nodes, resulting in more vibrational noise that obscured the modes of the modified FEA tire.

Other research on tire vibrational modes has produced a wide variety of results depending on the characteristics of tire studied (passenger/truck/agricultural type, size, ply type, inflation pressure, load), excitation method (drum-cleat, road cleats, indenter), and the experiment type (physical, FEA, or both) [5], [24], [34], [48], [49], [109]. The modes obtained from natural frequency analyses on unloaded, often analytical tire models, are also not necessarily the same thing as modes from force transmissibility tests on real, rotating and loaded tires. However, the first modes generally fall within a range of 20 Hz to 100 Hz [49], and truck tires are at the higher end of that range [5], [24], [34], [48], thus in this respect the values for the modified RHD tire model are realistic. Without physical test data on a closely related tire, it is impossible to be more conclusive about the drum-cleat test results.

3.3.4 Cornering Test

The fourth validation test done was a dynamic cornering test. In this test, the lateral or cornering force (F_y) experienced by the tire was determined at different slip angles and vertical loads. In order to validate the modified FEA tire model, its cornering force vs. slip angle curves were compared with those of the unmodified FEA tire model and experimental data from a similar 3-groove truck tire [21].

The cornering test simulation was based on the work of previous researchers [1], [21], [109] and is shown in Figure 3.18. Each tire was steered to a different slip angle α between 0 and 12 degrees, and then a constant longitudinal speed of 10 km/h was applied to the wheel COG node to force the tire to move forward at the specified angle to its direction of rotation. Vertical loads of 18, 27, and 36 kN, and an inflation pressure of 759 kPa were applied, as well as constraints in the local tire reference frame to prevent undesired lateral translation or rotation. The tires rolled on a hard road surface of null shell elements with a friction coefficient of 0.8, while the modified FEA tire model used a default tire-rim friction coefficient of 0.2, since a low value was more likely to cause different results from the original FEA tire model with the fixed tire-rim interface.

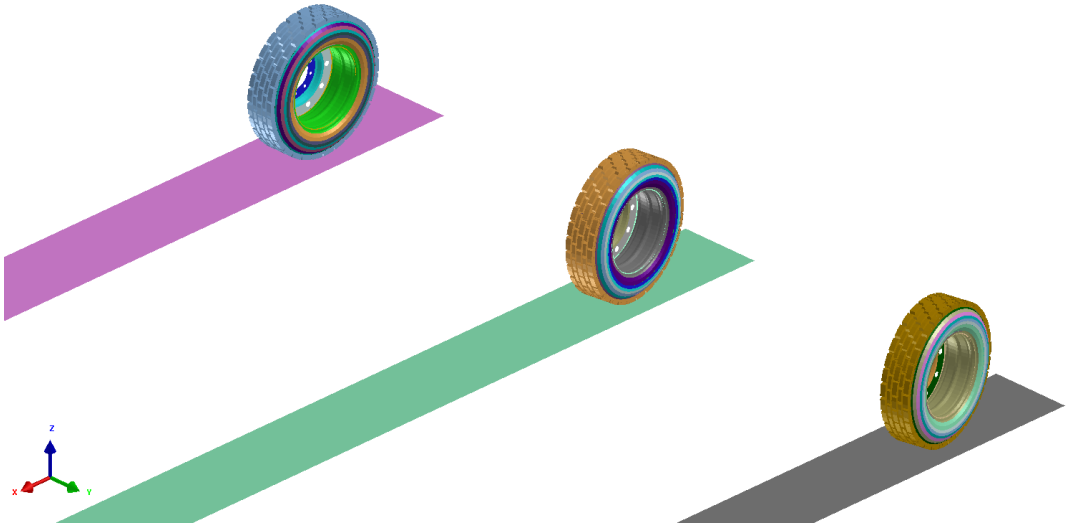

Figure 3.18: Cornering test simulation for modified FEA tire model with slip angles of 0, 8, and 12 degrees.

In order to calculate the cornering force F_y, the global F_X and F_Y forces were extracted from the tire-road contact patch, averaged over the steady state period of the simulation (0.6 to 1.5 seconds), and transformed to the tire reference frame using Eq. 3.7. Figure 3.19 shows the relationship between the contact forces in the global reference frame, the tire reference frame, and the slip angle α.

$$F_y = F_Y \cos\alpha + F_X \sin\alpha \tag{3.7}$$

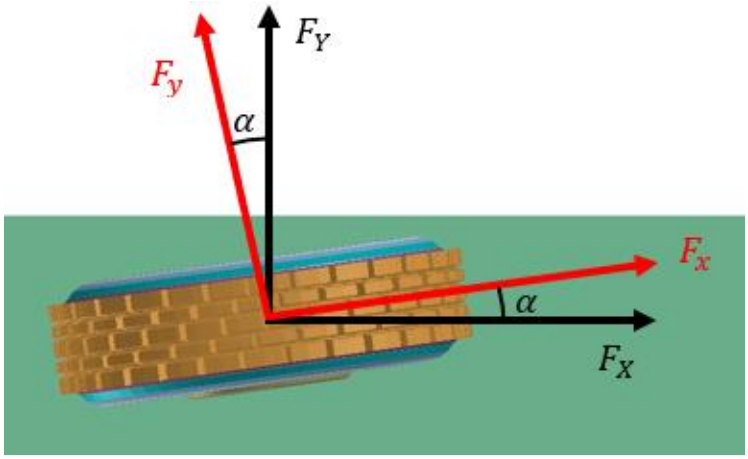

Figure 3.19: Contact forces for cornering test in global and tire reference frames.

The cornering forces for the original and modified FEA tire models were determined over a range of slip angles and at three vertical loads (18, 27, and 36 kN), and the resulting curves are compared in Figure 3.20. All of the curves show a similar trend where the cornering force increases quickly at lower slip angles, and then plateaus at higher slip angles. This is consistent with typical cornering behaviour [27]. However, there are a number of differences. The measured cornering forces (black lines), both increase and plateau more slowly than the original and modified FEA cornering forces, resulting in lower measured values below about 5 degrees and significantly higher measured values above 5 degrees. Thus, there is about 30% difference between the measured and FEA cornering forces by the time a 12-degree slip angle is reached. This trend is consistent across all of the vertical loads, and may be partially explained by the fact that the measured data comes from a 3-groove truck tire [21] instead of an RHD truck tire with 4-grooves.

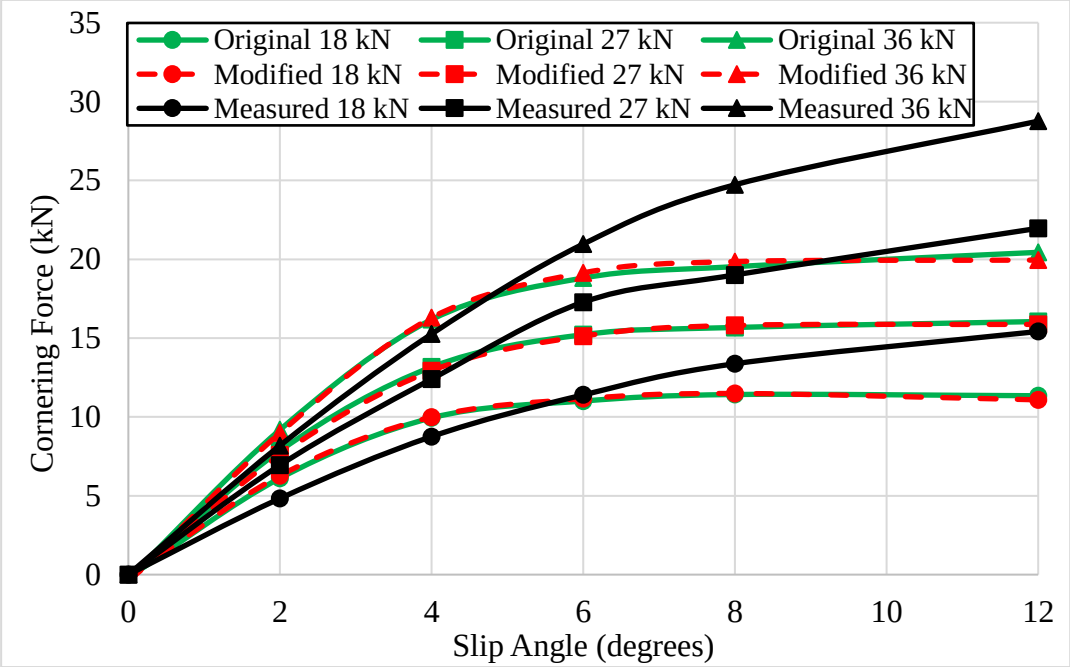

Figure 3.20: Cornering force comparison for FEA tire models. Measured data from [21].

With regards to the FEA cornering forces, both the original and modified FEA tire models had nearly identical results, with an average difference of 1.6%. This difference is acceptably small, demonstrating that adding the new tire-rim contact

did not significantly change the tire model's cornering behaviour, especially at low slip angles. The general trend of the FEA cornering force vs. slip angle is in fairly good agreement with the measured results, but a less sharp curvature would be more realistic. Further conclusions about the FEA model's real-life accuracy cannot be made without measured data specifically for a Goodyear RHD 315/80R22.5 truck tire. However, the modified FEA tire model with the tire-rim contact is sufficiently similar in its cornering behaviour to the original FEA model to be considered valid.

3.4 Frictional Torque Estimation

After the static and dynamic behaviour of the tire model was validated, additional tests were performed to assess the accuracy of the newly added tire-rim contact for representing the tire-rim interaction, specifically in estimating the frictional torque (T_f) required to cause tire-rim slip.

An equation was developed by Lee to estimate the total frictional torque by integrating the torques exerted by differential elements of the tire-rim contact [7]. The integral can be approximated by averaging the parameters across the tire-rim contact area, as shown in the below version of Lee's equation (Eq. 3.8). The equation's parameters and their ranges are listed in Table 3.6.

$$T_f = \int r\mu p_{cont} dA_{cont} \approx r\mu p_{cont} A_{cont} \tag{3.8}$$

Table 3.6: Parameters for Frictional Torque Equation

Parameter	**Symbol**	**Unit**	**Range/Value**
Frictional Torque	T_f	kNm	variable*
Radial Distance from Tire Center	r	m	0.3177
Tire-Rim Friction Coefficient	μ	none	0.05 – 0.9
Tire-Rim Contact Pressure	p_{cont}	kPa	variable*
Tire-Rim Contact Area	A_{cont}	m^2	variable*

*Extracted from FEA simulation.

There is inherently some error in Eq. 3.8 due to the use of averages and assuming that μ and r are constant throughout the contact area. In addition, it is important to note that the tire-rim contact pressure is different from the inflation pressure. PAM-

CRASH does not provide a results variable for the contact pressure, therefore the pressure stress on the solid elements involved in the tire-rim contact were used as a proxy.

In order to measure the accuracy of the tire-rim representation, static rim-slip tests were performed at a range of friction coefficients (0.05 – 0.9), a range of inflation pressures (276 – 896 kPa), with gravity, and with a constant vertical load of 41 kN. The general simulation parameters were the same as those described in section 3.1.2. However, the wheel was also constrained in the x-direction and the tread was fixed in place to represent a locked tire condition. A constant angular velocity of 0.50875 rad/s equivalent to a 1 km/h longitudinal wheel speed was applied to the rim, and the drive torque T required to sustain that angular velocity was extracted from the simulation. The maximum value of the drive torque T after the angular velocity was applied was taken as the simulated frictional torque for that combination of tire-rim friction coefficient and inflation pressure. Next, the contact pressure and contact area were extracted and then Eq. 3.8 was used to calculate the corresponding theoretical frictional torque. The simulated and theoretical frictional torques are compared in Figure 3.21.

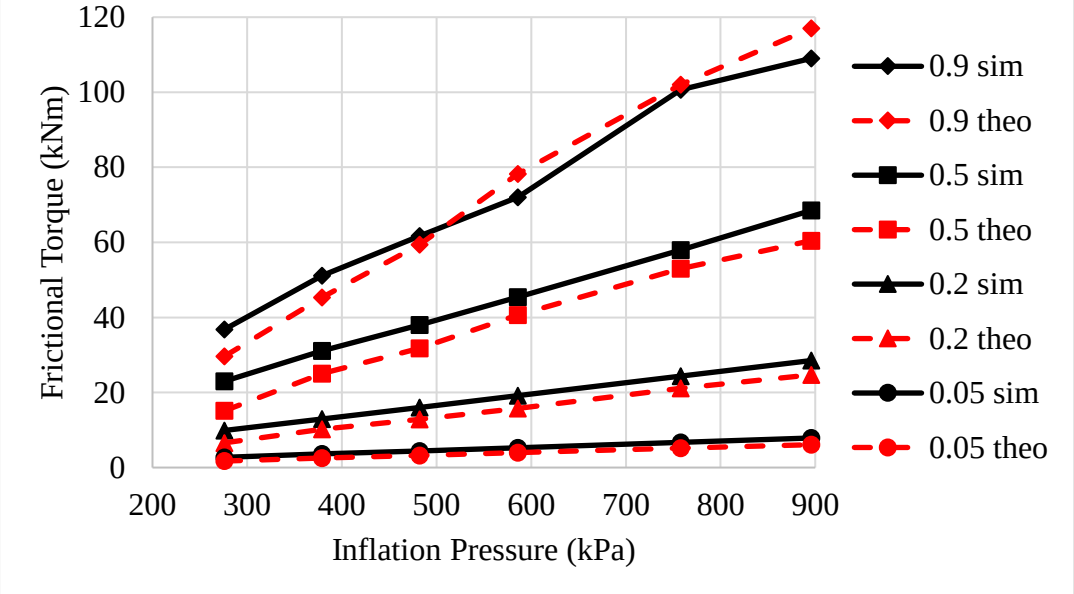

Figure 3.21: Simulated and theoretical frictional torques for static rim-slip tests with different inflation pressures and tire-rim friction coefficients.

In general, the results show that the frictional torque increases with both the inflation pressure and the tire-rim friction coefficient, which is inline with the proportional relationship of the parameters in Eq. 3.8. There is also fairly good agreement between the simulated and theoretical frictional torques, since the trends are the same and there is an average difference of 16.7% between the two data sets, with the simulated results consistently being higher.

When viewing the simulation results, there was a noticeable "stick-slip" phenomenon for the higher inflation pressures and tire-rim friction coefficients. In stick-slip, the rim stuck to the tire bead, with the applied torque increasing and twisting the tire carcass until the frictional torque was exceeded. Then, the rim slipped and the bead jumped back to its untwisted position, with the drive torque dropping as well. This behaviour resulted in a choppy output, with the drive torque and contact pressure changing rapidly. The transient nature of the simulated stick-slip phenomenon also made it difficult to estimate the correct time-step from which to use the contact pressure values, hence the atypical position of the theoretical frictional torque line relative to the simulated frictional torque line at 896 kPa. The frictional torque results were much more consistent at lower tire-rim friction coefficients where the contact pressures were almost constant. In summary, although there was some difference between the simulated and theoretical frictional torques, this was likely due to the difficulty in accurately measuring the contact pressure, and otherwise the FEA tire-rim contact model was appreciably similar to the results calculated from theory. As long as the difficulty in accurately modelling transient stick-slip phenomena is taken into account, the modified FEA tire model was sufficiently accurate in estimating the frictional torque.

3.5 Chapter Summary

This chapter described properties of a previously developed FEA model of an RHD truck tire, as well as the modification of the FEA model for simulating tire-rim slip. The tire-rim slip quantification and measurement process were also described. Key innovations included the use of a symmetric node-to-segment contact definition between tire and rim parts, and the introduction of a new quantity called rim-slip i_{rim}

for measuring the relative rate of tire-rim slip. Next, the modified FEA tire model was validated by comparing its performance to the original FEA tire model and physical test data from the manufacturer. Comparisons were done with static and dynamic tests, including footprint, vertical stiffness, drum-cleat, and cornering tests. The modified tire model was found to have very similar performance to the original tire model, with satisfactory agreement with the physical test data to the extent that it was available. Finally, the modified tire model's ability to estimate frictional torque was assessed, and it also had good agreement with the theoretical results. Therefore, the modified FEA tire model was considered valid and ready to be used in data-collecting rim-slip simulations.

Chapter 4. Soil Modelling and Calibration

This chapter describes the setup and calibration of the SPH particles modelling the upland sandy loam soil. Steps included are setting the SPH element parameters, researching the measured characteristics of upland sandy loam, creating simulated tests to characterize the SPH soil model, and calibrating the SPH material parameters. Once fully calibrated, the SPH particles were used to represent the upland sandy loam soil during the tire-rim slip simulations presented in Chapter 5.

4.1 SPH Particle Parameters

The SPH particles were created by converting cube-shaped FEA hexahedral elements measuring 25 mm a side into SPH elements (element is the term used in FEA algorithms) using a tool built into PAM-CRASH. This operation gave each SPH particle a starting volume of $(25\ \text{mm})^3$ or $15{,}625\ \text{mm}^3$, from which the particle radius was computed. The SPH element formulation also had several required and optional parameters that needed to be specified, such as those controlling the smoothing length h (see section 2.4.4) [80]. The smoothing length h is initially specified as a multiple ($RATIO$) of the SPH particle radius and changes dynamically within specified bounds ($Hmin$ and $Hmax$) during the simulation to reflect the changing spatial density of the SPH particles. ETA is an additional parameter reflecting the strength of a corrective equation added to the SPH element formulation to improve the particle stability and prevent interpenetration [80]. The $RATIO$ parameter was set to the minimum allowed by the solver, while the others were set based on Lescoe's recommendations [81]. All of the parameter values used are listed in Table 4.1.

Table 4.1: SPH element parameters

Parameter	**Value**	**Description**
Volume	$15{,}625\ \text{mm}^3$	SPH particle volume
$RATIO$	1.2001	Ratio of particle smoothing length to radius
$Hmin$	1	Minimum smoothing length
$Hmax$	100	Maximum smoothing length
ETA	0.1	Anti-crossing force parameter

4.2 Determination of Soil Characteristics

Research was initially done to locate pressure-sinkage and shear characteristics for a soft soil with a high moisture content, and Bekker equation parameters (Eqs. 4.1, and 4.2) were found for a silty clay with 62.29% moisture [59]. Unfortunately, the SPH model of this soil proved too soft to support the RHD tire with vertical load of 41 kN typical for a tire-rim slip test. The source paper also used a very small range of pressures (0.1 to 0.9 kPa) to derive the Bekker pressure-sinkage equation, and the authors acknowledged that the accuracy of the results was questionable due to a negative k_ϕ coefficient [59]. These deficiencies resulted in the decision to use a slightly firmer soil from a more reliable source.

$$p_{soil} = (\frac{k_c}{b} + k_\phi)z^n \tag{4.1}$$

$$\tau_{max} = c + p_{soil} \tan \phi \tag{4.2}$$

The second soil found was an upland sandy loam, selected based on its high moisture content (51%) and soft pressure-sinkage behaviour compared to the other soils in a table compiled by Wong [27]. The Bekker equation parameters for this soil are summarized in Table 4.2. Plotting the soil sinkage (z) and maximum shear stress (τ_{max}) as a function of the applied pressure (p_{soil}) using Eqs. 4.1 and 4.2 created a pair of curves (see Figures 4.3-4.6) that characterized the upland sandy loam's behaviour at different pressure or loading conditions.

Table 4.2: Measured Bekker equation parameters for upland sandy loam [27]

Parameter	**Units**	**Value**
n	none	1.10
k_c	kN/m^{n+1}	74.6
k_ϕ	kN/m^{n+2}	2080
c	kPa	3.3
ϕ	deg	33.7

In addition, the SPH material formulation also required density information. This was estimated by surveying multiple field research sources for the properties of upland sandy loam [61]-[63], [114], and comparing them with the moisture content

of 51% reported by Wong. The moisture content was high compared to the other soils listed by Wong, which means it is likely that the upland sandy loam was oversaturated with water. The oversaturation is supported by an agricultural engineering experiment that found a sandy loam with a much lower moisture content of 14.7% by mass [61]. Since the upland sandy loam was oversaturated, water filled all the voids between the soil particles and forced them further apart. Therefore, we would expect a density lower than the 1.51 g/cm^3 measured at 14.7% moisture, and likely also lower than the dry density of sandy loam, because water is less dense than the soil particles. Since a representative density value given for dry sandy loam was 1.44 g/cm^3 [114], a lower density of 1.40 g/cm^3 was assumed for the upland sandy loam with 51% moisture. This is a reasonable value considering that it is denser than a more highly saturated silty clay (1.2 g/cm^3) [59] and less dense than a saturated clay (2.01 g/cm^3) [37]. Once all the properties and characteristics of the upland sandy loam were determined, the next step was to characterize and calibrate the SPH soil model.

4.3 SPH Soil Model Characterization

As discussed in Chapter 2.4, several key parameters are used to describe the terramechanics characteristics of a soil. In particular, Bekker developed the bevameter to measure both the pressure-sinkage and shear stress characteristics of a soil [65]. This machine applied a range of pressures to two test devices and measured the resulting pressure-sinkage and shear force-displacement curves. A similar method using two simulated tests was previously developed in PAM-CRASH to determine the pressure-sinkage and shear stress characteristics of the SPH soil [81].

The simulated pressure-sinkage test consisted of a set of 800 mm by 800 mm by 600 mm boxes filled with SPH particles, with a 150 mm-radius thin rigid disk positioned in the center above the SPH particles (Figure 4.1). Contact definitions governed the interactions between the SPH particles, box, and disk similar to the tire-road contact discussed in Chapter 3. The disks were loaded at 6 different constant pressures of 0, 10, 50, 100, 150, and 200 kPa, and the sinkage z corresponding to each pressure was taken as the steady-state vertical displacement of the disk after 0.4 seconds.

Subsequently, the resulting pressure-sinkage data points were combined into a curve representing the pressure-sinkage characteristics of the SPH soil (Figure 4.3).

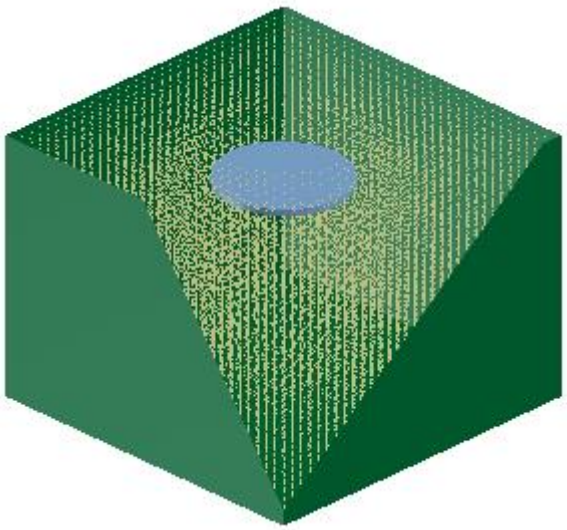

Figure 4.1: Cutaway of a soil box for the simulated pressure-sinkage test [115].

The direct shear test, on the other hand, was simulated with a more complicated setup (Figure 4.2). There were two boxes filled with SPH particles, a fixed lower box and an upper sliding box. The total volume containing the SPH particles measured 388 mm by 388 mm by 177 mm with extensions attached to the boxes to enable sliding, as shown in Figure 4.2. As with the pressure-sinkage tests, a specified constant pressure was applied to the upper plate (0, 10, 50, 100, 150, and 200 kPa). However, instead of remaining stationary, the upper box and sliding plate were moved at a constant rate of 5 mm/s to generate shear forces between the SPH particles at the junction between the upper and lower plates. The simulation was run for 10 seconds and the maximum shear stress averaged across the junction during that time period was taken as τ_{max} in Eq. 2.6. Combing the pressure-τ_{max} data points resulted in a curve describing the shear stress characteristics of the SPH soil (Figure 4.4).

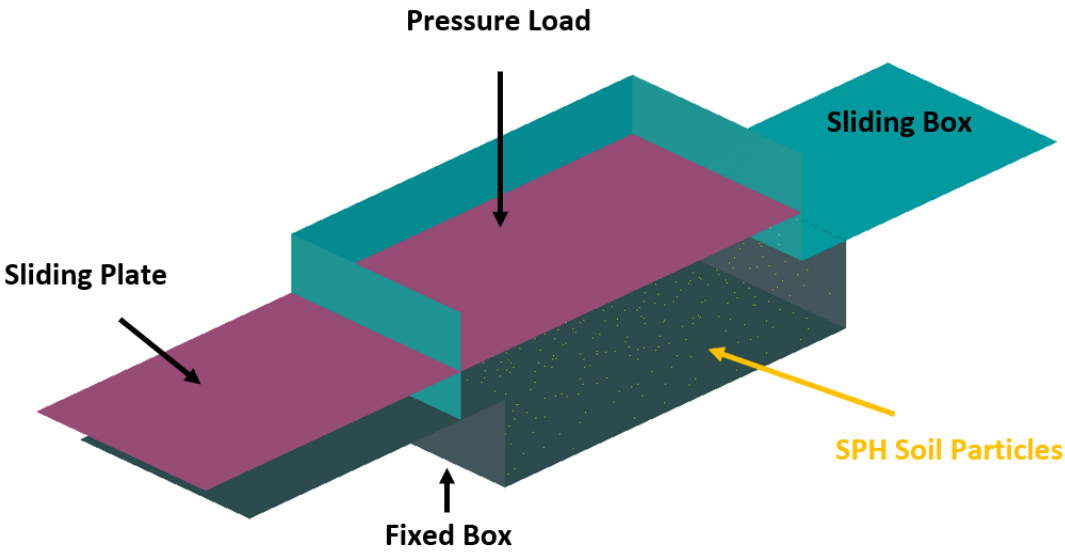

Figure 4.2: Cross-section of soil boxes for a simulated direct shear test [115].

4.4 SPH Soil Calibration

The SPH soil was calibrated iteratively by modifying the SPH material parameters shown in Table 4.3, then performing the simulated pressure-sinkage and direct shear tests. The results of each trial were compared with the curves based on the measured Bekker equation parameters for the upland sandy loam from Table 4.2. A key part of this process was using the same SPH material parameters for both types of tests.

Table 4.3: SPH material parameters

Parameter	Density*	Shear modulus	Yield strength	Elastic modulus	Bulk modulus
Symbol	ρ	G	σ_y	E_t	C_1
Units	g/cm^3	MPa	MPa	MPa	MPa
Trial #					
1	1.32	6	0.002	0.2	2
2	1.32	6	0.002	0.25	2
3	1.32	6	0.002	0.25	10
4	1.32	6	0.001	0.25	10
5	1.32	6	0.002	0.25	15
6	1.32	6	0.002	0.25	20
7	1.40	6	0.002	0.2	20
8	1.40	6	0.007	0.2	20
9	1.40	6	0.012	0.2	20
10	1.40	6	0.012	0.2	25
11	1.40	12	0.012	0.2	25
12	1.40	6	0.012	0.25	25
13	1.40	6	0.012	0.3	25
14	1.40	6	0.012	0.27	25

*The density parameter was not calibrated but instead estimated from measurements in the literature.

SPH material parameters for Trial 1 were chosen similar to those for other soil models, and the pressure-sinkage and shear stress curves were then compared with the curves calculated from the measured Bekker equation parameters in Table 4.2 (see Figures 4.3 and 4.5). Subsequently, the SPH material parameters were changed one or two at a time, in order to match the measured and simulated curves. The density was re-estimated during the simulations and changed from 1.32 g/cm^3 to 1.40 g/cm^3 as per the previous discussion in section 4.2. This small change had no impact on the pressure-sinkage and shear stress curves. The shear modulus G was hardly changed since it also had minimal effect on the shape of the curves. On the other hand, the yield strength σ_y was frequently changed in concert with the elastic modulus E_t, and bulk modulus C_1, until a value of 0.012 MPa was settled on. Figures 4.3-4.6 visualize the effects of changing the SPH material parameters of the simulated soil from one trial to another. Varying the parameters from the initial values chosen for Trial 1 brought the slope, position, and curvature of the simulated curves (dashed lines) closer to the target or measured curve (solid line).

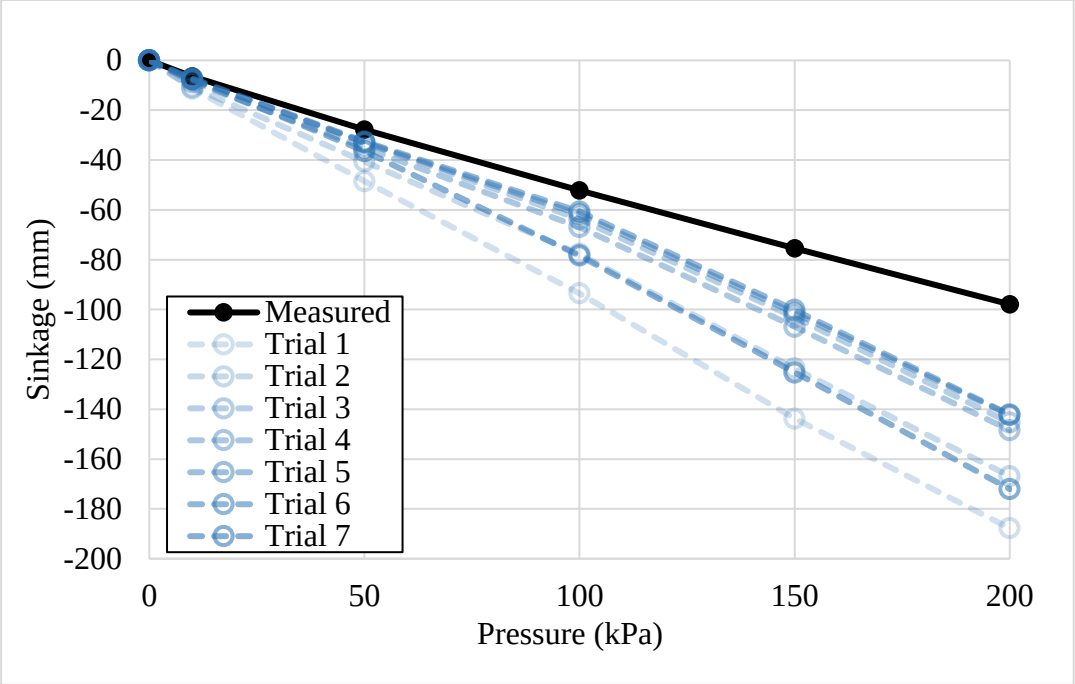

Figure 4.3: Pressure-sinkage curves for Trials 1-7. The black solid line is based on the measured Bekker equation parameters.

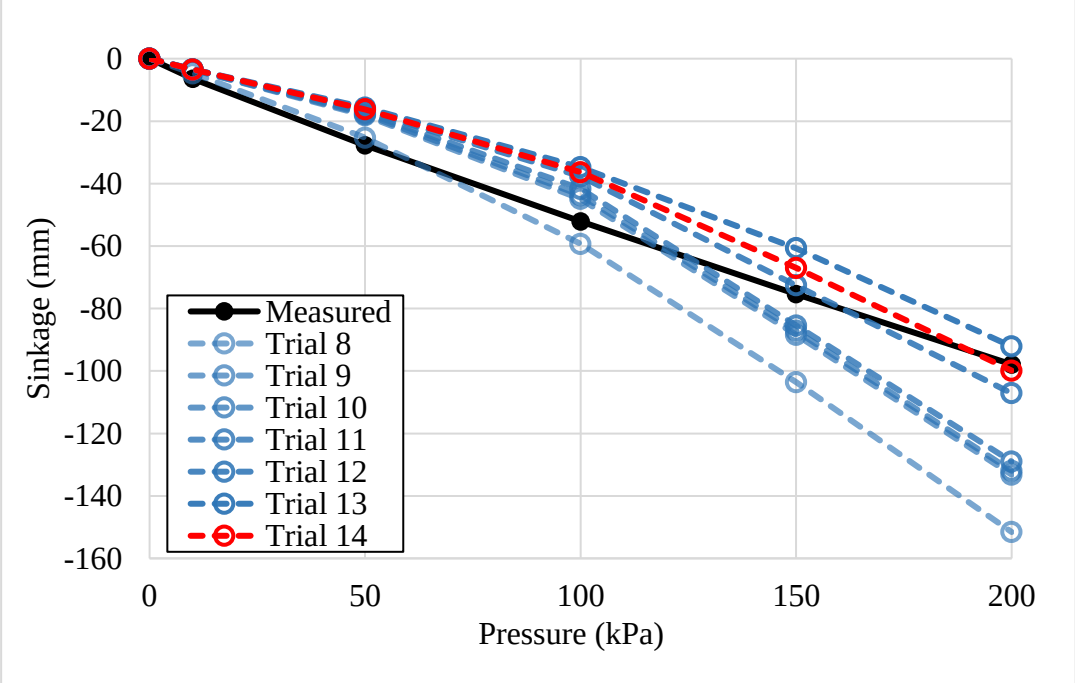

Figure 4.4: Pressure-sinkage curves for Trials 8-14. The red line is the best simulated soil.

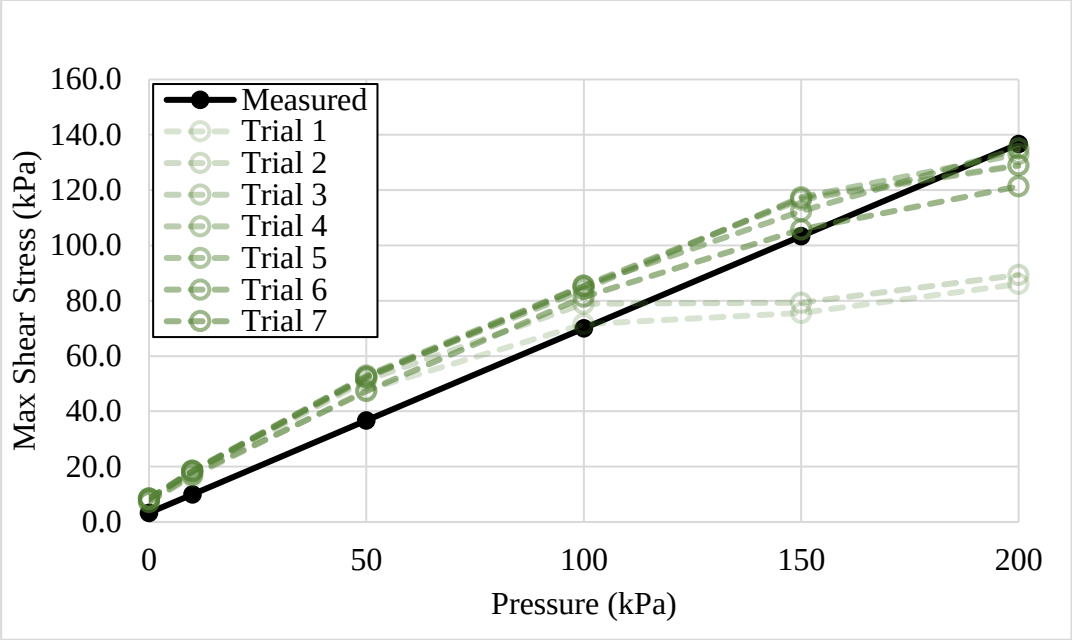

Figure 4.5: Shear stress curves for Trials 1-7. The black solid line is based on the measured Bekker equation parameters.

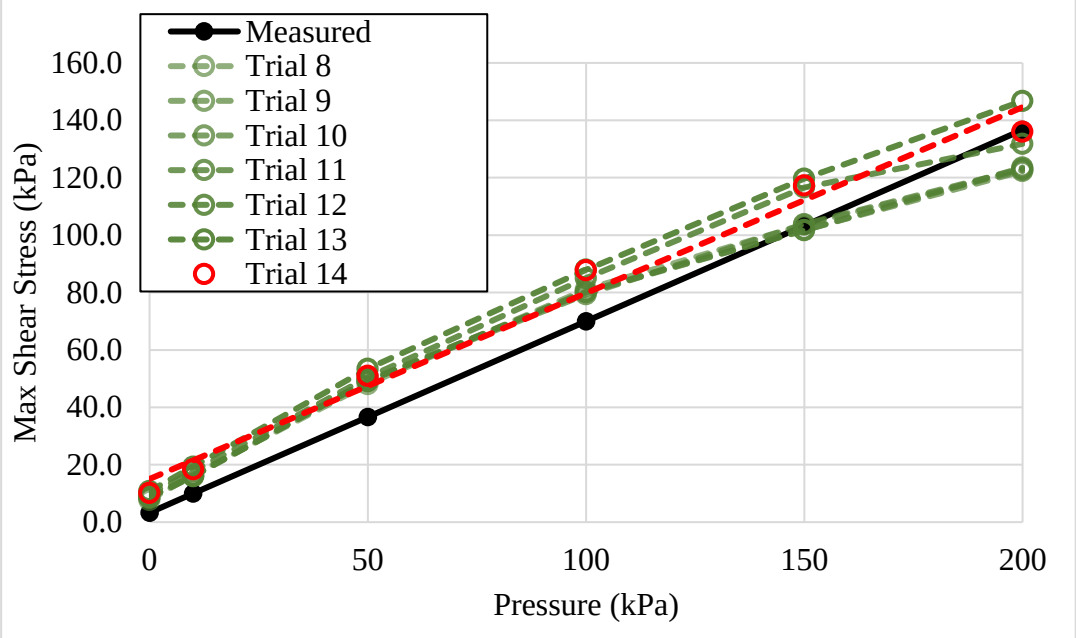

Figure 4.6: Shear stress curves for Trials 8-14. The red line is the best simulated soil.

During the calibration process, the effect of each of the parameters in Table 4.3 on the pressure-sinkage and shear stress characteristics of the SPH soil was discovered by trial and error. The tensile modulus E_t had a very large effect on the slope of the

two characteristic curves. A smaller E_t resulted in a softer soil with larger magnitude slopes for both the pressure-sinkage and shear stress. E_t had to be balanced carefully since it could not match both of the measured curves well at the same time. The bulk modulus C_1 had a significant effect on the curvature of the simulated curves. Increasing C_1 led to a more linear shape, while decreasing C_1 made the curvature more negative. The yield strength of the SPH material σ_y had a significant effect as well. Increasing the yield strength shifted the entire shear stress curve upwards by a slight amount, and increased the stiffness of the initial portion of the pressure-sinkage curve. To understand this behaviour, it can be connected to the idea of yielding. Increasing the yield strength increases the minimum stress at which the soil yields and shear occurs, thereby shifting the shear stress curve upwards. Increasing the yield strength also increases the initial pressure before the soil yields vertically, causing the first portion of the pressure-sinkage curve to have a shallow angle before the soil yields and the sinkage is more rapid and governed by the elastic modulus. Finally, the shear modulus G, had little impact, shifting both curves upwards slightly, but with a much lower effect than the other parameters, unless the yield strength was very low, less than 0.01 MPa. These effects are based on observations made during the calibration process, and other effects may occur at different values of the SPH material parameters due to nonlinearities in the material behaviour.

In addition to graphical comparison, the curves resulting from the different trials were compared quantitatively with the measured curve using the mean squared error (MSE) and R^2 goodness of fit metrics. In general, a lower MSE indicated the average position of the points was closer to the measured curve, while an R^2 closer to 1 indicated the overall shape and curvature was closer to that of the measured curve. All of the trials are compared using these metrics in Table 4.4.

Table 4.4 MSE and R^2 values for select trials

	Pressure-Sinkage		**Shear Stress**	
Trial Number	MSE	R^2	MSE	R^2
1	2485.8	0.999	586.7	0.895
2	1321.1	0.995	533.2	0.869
3	532.4	0.991	137.9	0.973
4	637.8	0.993	140.3	0.973
5	465.1	0.990	126.4	0.981
6	445.2	0.989	109.1	0.986
7	1459.8	0.993	91.5	0.977
8	622.7	0.977	85.6	0.980
9	261.3	0.959	89.3	0.981
10	246.3	0.957	82.8	0.982
11	216.0	0.954	84.1	0.982
12	72.4	0.966	119.8	0.981
13	117.3	0.972	186.5	0.994
14	77.4	0.969	138.7	0.985

As seen in Table 4.4, varying a given SPH material parameter often improved the accuracy of one curve at the expense of another, therefore the trials were used to discover the effect of each parameter on the critical features of each curve. For the shear stress curve, having a linear shape (high R^2) was more important than having the closest average values (low MSE), while for the pressure-sinkage curve, the most important feature was having a shallow slope. This last factor is why Trial 14 was chosen over other trials that had higher R^2 values. If, for example, Trial 6 had been used, the SPH soil would have sunk substantially more than the measured curve at pressures above 200 kPa, which would occur when simulating the RHD tire on the soil. Therefore Trial 14 was chosen to avoid the problems experienced with the first very soft soil.

In addition, another accuracy check was made making use of the almost-linear shape of the shear stress curve. For constant values of coefficients c and ϕ, Eq. 4.2 [66] relates τ_{max} to p_{soil} using a straight line with slope $\tan\phi$ and intercept c. Therefore, linearly interpolating the simulated shear stress datapoints from Trial 14 allowed coefficients c and ϕ to be calculated for the SPH soil from the equation of the line of

best fit (Figure 4.6). To one decimal place, the coefficients c and ϕ were found to be 15.0 kPa and 32.9°, respectively. These values explain the vertical shift due to c and the similar slope due to ϕ of the simulated soil, when compared to the measured upland sandy loam c and ϕ coefficients of 3.3 kPa and 33.7°. Performing the linear interpolation thus demonstrated that the SPH soil accurately modelled the effect of the upland sandy loam ϕ coefficient.

4.5 Chapter Summary

The calibration process described in this chapter resulted in a set of SPH material parameters that produced an SPH soil with acceptable pressure-sinkage and shear stress characteristics. The simulated characteristic curves were sufficiently close to both measured curves in terms of MSE (77.4, 138.7) and R^2 (0.969, 0.985), and had a desirable overall shape. Figures 4.4 and 4.6 show the simulated characteristics of the final calibrated SPH soil (Trial 14) compared with the measured characteristics for the modelled upland sandy loam. The SPH element and material parameters shown in Tables 4.1 and 4.3 characterized the SPH soil model, which was used to represent the soft uplands sandy loam soil for the tire-rim slip tests on soil described subsequently in Chapter 5.

Chapter 5. Tire-Rim Slip Results and Analysis

This chapter describes the design and results of the simulated tire-rim slip tests on the hard surface mentioned in Chapter 3, and on the SPH soil calibrated in Chapter 4. Included are the simulation design and parameters, the independent effects of the tire-rim friction coefficient, drawbar load, inflation pressure, vertical load and longitudinal wheel speed, and a comparison between the hard surface and soil results.

5.1 Tire-Rim Slip on Hard Surface

Once the tire FEA model was modified and validated for simulating tire-rim slip, the next step was to investigate which operating conditions and simulation parameters had a significant effect on the amount of tire-rim slip. Tire-rim slip on a dry hard surface like concrete or asphalt was investigated first before moving to the more complex off-road terrain covered in section 5.2. The use of a hard surface with a high coefficient of friction also reflects the procedure in ASTM F2803 [55].

5.1.1 Hard Surface Rim-Slip Test Design

Each hard surface simulation had 5 tires running in parallel with different operating conditions in order to reduce the total number of simulations required (Figure 5.1). The tire-road coefficient was kept at a constant value of 1.0 in order to minimize the potential for slip at the tire-road interface, again following ASTM F2803 where any such slip would invalidate the test. The details of the tire-road and tire-rim contacts are listed in Table 5.2 in section 5.2.1. All of the other simulation parameters were the same as described in Chapter 3.

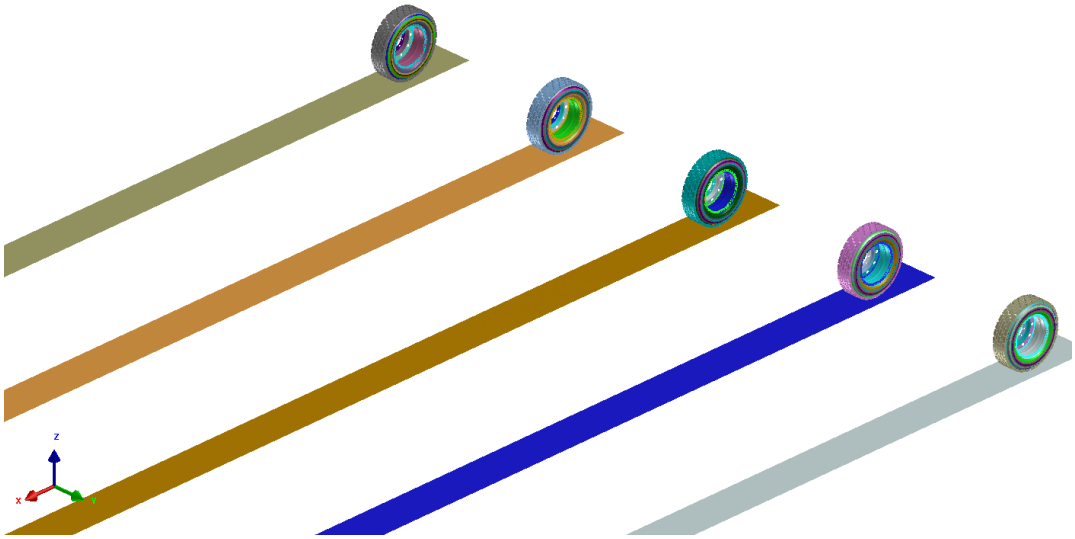

Figure 5.1: Tire-rim slip test on a hard surface.

Since tire-rim slip is a phenomenon where the drive torque transmitted through the tire-rim interface exceeds the frictional torque, simulation parameters were investigated that affected the drive torque and the frictional torque. Specifically, these were the tire-rim friction coefficient, drawbar load, vertical load, inflation pressure, and longitudinal wheel speed, as listed in Table 5.1 below. A large range of values was used for each parameter, with the default conditions chosen to have a high-load and low-pressure, in which the most interesting effects on tire-rim slip were expected to occur. The five parameters were varied two at a time, with the other three parameters remaining at their default values, since the goal was to assess the independent effects of each parameter, and some simple interactions, as opposed to a full variational study. The steady-state values of rim-slip for each combination of parameters were extracted following the procedure described in Chapter 3, and were plotted against the varied parameters in Figures 5.2-5.4.

Table 5.1: Parameters varied for tire-rim slip simulations on a hard surface

Parameter	**Symbol**	**Unit**	**Range**	**Default Value**
Tire-Rim Friction Coefficient	μ	none	0.05 – 0.9	0.2
Drawbar Load	F_D	%	30 – 90	90
Inflation Pressure	p_{inf}	kPa	276 – 896	379
Vertical Load	F_z	kN	13 – 41	41
Longitudinal Wheel Speed	V_x	km/h	5 – 60	10

5.1.2 Effects of Tire-Rim Friction Coefficient and Drawbar Load

Figure 5.2 shows the effects of the tire-rim friction coefficient and drawbar load on the rim-slip. Increasing the tire-rim friction coefficient decreased the rim-slip, with a small effect on the tails of the curves in Figure 5.2, and a very rapid change between 0.1 and 0.3. This threshold effect, where the rim-slip was close to 0% until the tire-rim friction coefficient dropped below a particular value, was consistent across all three drawbar loads tested. The threshold effect can be explained using the concept of frictional torque from Chapter 3. Once the drive torque exceeds the frictional torque, either because of an increased drawbar load or a decreased tire-rim friction coefficient, the excess torque rapidly accelerates the rim relative to the tire until its relative rotation is fast enough for 100% rim-slip to occur.

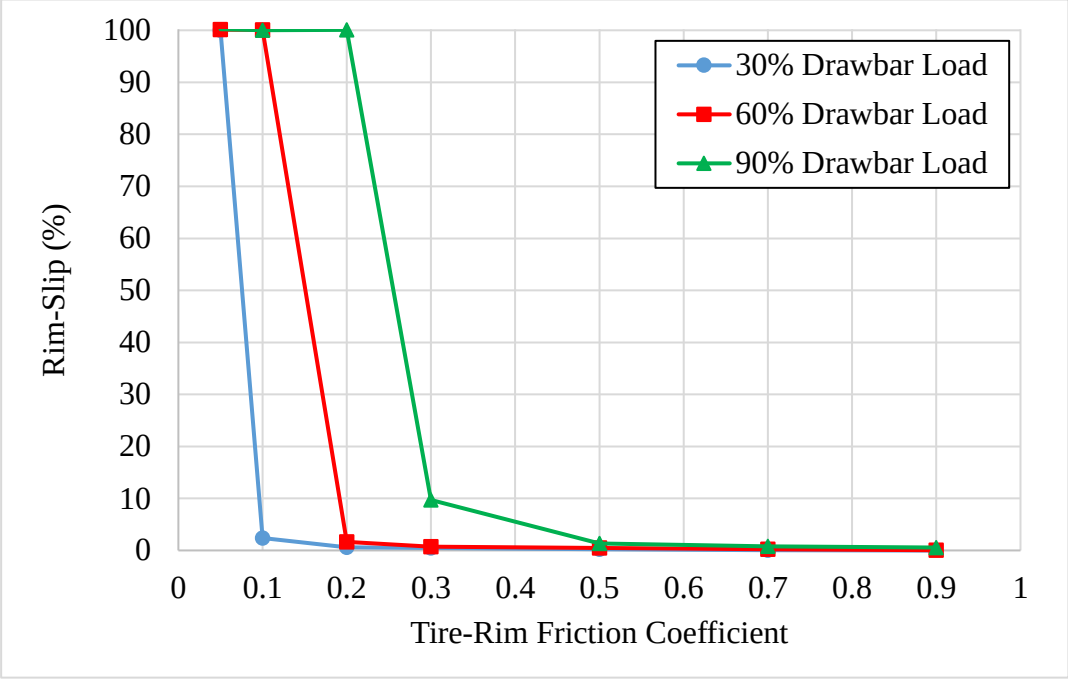

Figure 5.2: Effects of tire-rim friction coefficient and drawbar load on rim-slip [107]. The other parameter settings were 379 kPa inflation pressure, 41 kN vertical load, and 10 km/h longitudinal wheel speed.

Increasing the drawbar load, on the other hand, lead to a larger rim-slip. For example, at a friction coefficient of 0.2, the rim-slip is 1.67% for the 60% drawbar load, but 100% for the 90% drawbar load. All three of the curves in Figure 5.2 show the same trend for the rim-slip with respect to the tire-rim friction coefficient, however the

curve shifts right with each increase in drawbar load. This happens because the threshold value for the tire-rim friction coefficient increases with the drawbar load. For example, at a 30% drawbar load the threshold is at 0.1, while for the 90% drawbar load the threshold increases to 0.3. It is clear from Figure 5.2 that rim-slip only occurs at very low coefficients of friction, and that a high drawbar load is a significant factor in causing rim-slip.

5.1.3 Effects of Inflation Pressure and Vertical Load

The inflation pressure has an adverse effect on rim-slip, since Figure 5.3 shows that increasing the inflation pressure results in less rim-slip. Once again, there is a threshold effect, in that the rim-slip rapidly goes from close to 0% to 100% between two consecutive tested inflation pressures. For example, with a 41 kN vertical load the rim-slip was 1.48% at 586 kPa but changed to 100% when the inflation pressure dropped to 482 kPa. The threshold effect can be explained by the influence the tire inflation pressure has on the average tire-rim contact pressure, and thus on the frictional torque of the tire-rim contact. Once lowering the inflation pressure lowers that frictional torque below the drive torque applied to the rim, the rim quickly accelerates until it reaches 100% slip. The inflation pressure also had negligible effect on the rim-slip at the lowest tested load of 13 kN.

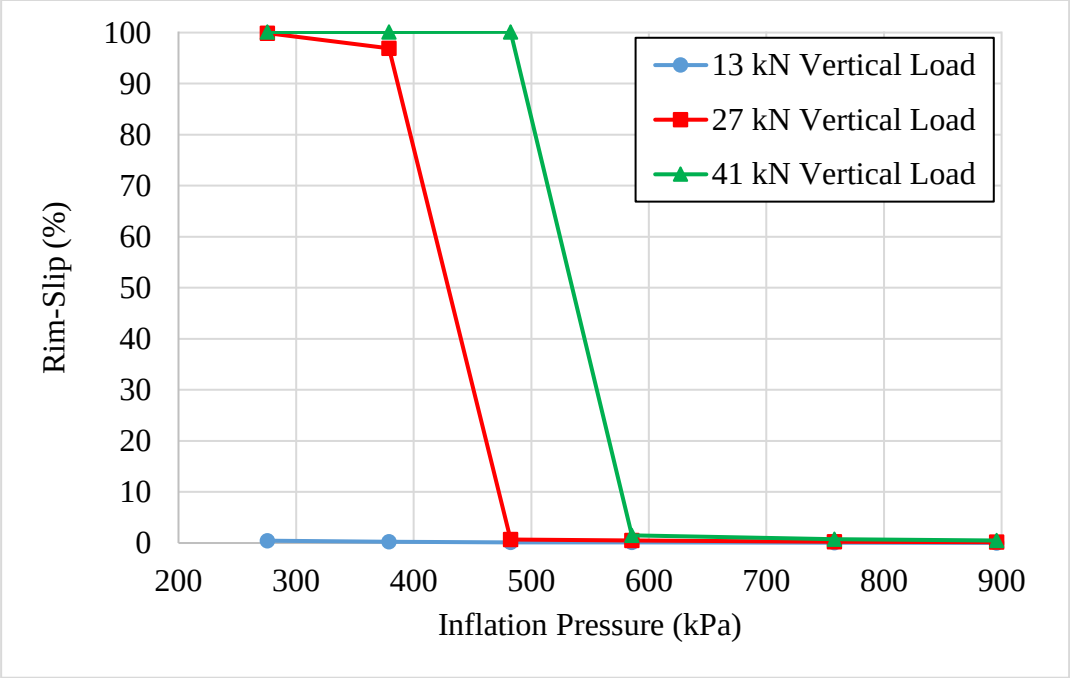

Figure 5.3: Effects of inflation pressure and vertical load on rim-slip [107]. The other parameter settings were 0.2 tire-rim friction coefficient, 90% drawbar load, and 10 km/h longitudinal wheel speed.

The vertical load had a clear effect on the rim-slip curves in Figure 5.3, with a higher vertical load resulting in more rim-slip. For example, at 379 kPa the 13 kN vertical load had only 0.27% rim-slip, while the 27 kN vertical load had 96.94% and the 41 kN vertical load had 100% rim-slip. The vertical load affects the rim-slip since, with the constant tire-road friction coefficient of 1.0, the vertical load determines the amount of tractive force available at the tire-road contact. That tractive force, in turn, controls how much drive torque can be applied through the tire-rim interface and thus whether the frictional torque will be exceeded. There was a similar trend between the 27 kN and 41 kN curves, but the 13 kN curve was different as it was too small to have any rim-slip. Furthermore, increasing the vertical load increased the threshold inflation pressure at which the transition from 0% to 100% rim-slip took place. For example, the threshold value for the 27 kN curve was 482 kPa, while for the 41 kN curve it was 586 kPa. In summary, high vertical loads combined with low inflation pressures significantly increase the chance of rim-slip occurring.

5.1.4 Effect of Longitudinal Wheel Speed

There was almost no effect of the longitudinal wheel speed on the rim-slip, as shown by the flat lines in Figure 5.4, especially when compared to the large change in rim-slip from a drawbar load of 40% to a drawbar load of 90%. This lack of effect was partially due to the way that rim-slip was defined in Eqs. 3.5 and 3.6. It was defined as a relative rate based on the ratio of the tire and rim angular velocities, therefore it was independent of the angular and longitudinal wheel speeds.

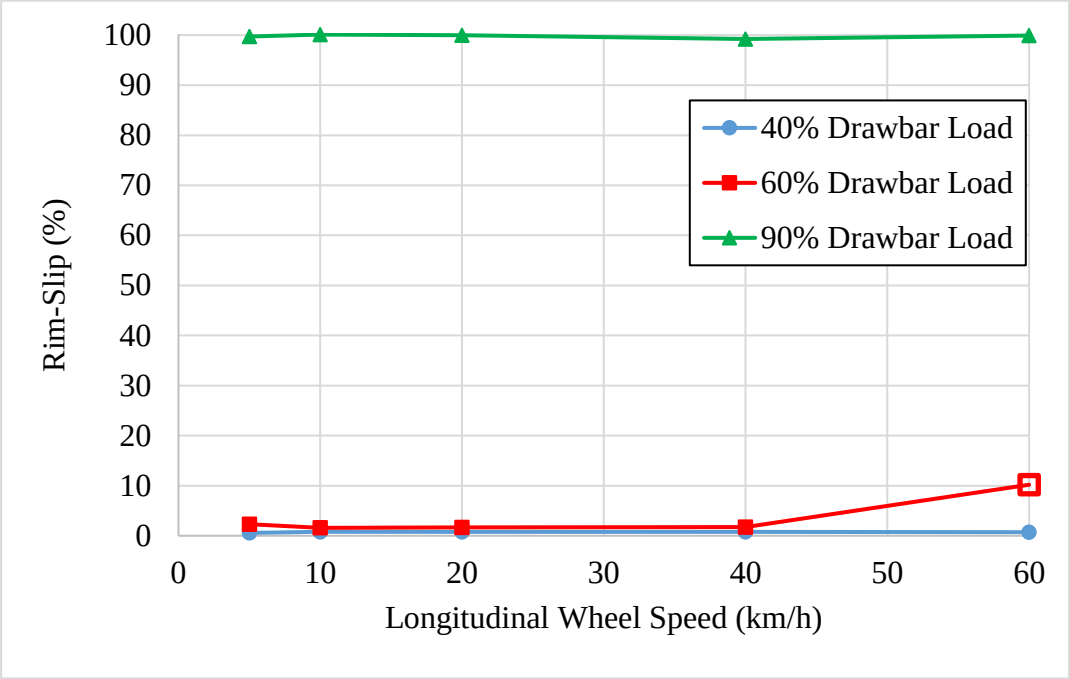

Figure 5.4: Effects of longitudinal wheel speed and drawbar load on rim-slip [107]. The other parameter settings were 379 kPa inflation pressure, 41 kN vertical load, and 0.2 tire-rim friction coefficient.

The exception to this overall lack of effect was an outlier data point at 60 km/h and 60% drawbar load, represented by a hollow square in Figure 5.4. In this simulation, the rim-slip varied continuously, not reaching a steady-state value, and is instead represented by an average value. This only occurred close to 60 km/h, an additional simulation at 70 km/h had a steady-state rim-slip value of 1.47%. Observation of the simulation results showed a significant amount of vibration in the tire model, therefore it is possible that at 60 km/h the tire was rotating close to a natural frequency, causing vibrations in the tire-rim contact that prevented it from reaching

a steady-state. In summary, the longitudinal wheel speed had negligible effect on the relative rim-slip, however, in a given time frame a slipping rim will still experience a greater total rotation relative to the tire when it is rotating at a higher speed.

5.2 Tire-Rim Slip on Soil

Since the low-pressure and high-drive torque conditions conducive to tire-rim slip often occur during off-road driving, the tire-rim slip tests done on the hard surface were conducted again on a soft soil terrain to discover if varying the same parameters resulted in the same or different effects. The particular results in this section apply only to the upland sandy loam modelled in Chapter 4, however, general trends and the relationship to the rim-slip results from the hard surface tests should apply to other soils as well.

5.2.1 Soil Rim-Slip Test Design

The tire FEA model and general simulation parameters were the same as those used for the hard surface tire-rim slip simulations described in Chapters 3. However, some changes were made to accommodate the SPH soil. The main change was replacing the rigid shell element road in the hard surface simulations with a rigid shell element box containing SPH elements (Figure 5.5). The box was created using the following procedure. First, the required length of the box was estimated based on the longitudinal wheel speed, the simulation time (1.5 s), and some extra space for soil compression. A round number close to the estimate (e.g. 5100 mm for 10 km/h) was chosen that was an even multiple of the calibrated SPH element size of 25 mm. Similarly, the width and depth of the soil box were set at 800 mm and 600 mm, respectively, to accommodate the width of the tire and allow for 24 vertical layers of SPH particles.

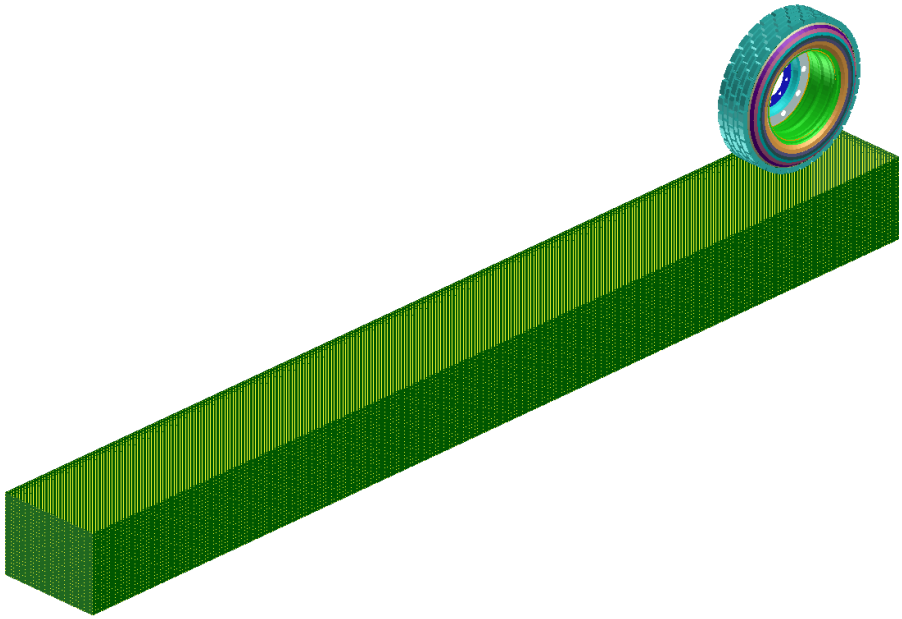

Figure 5.5: Perspective view of the FEA truck tire and shell element box containing soil SPH elements. The box is sized for a 10 km/h run.

Once the basic dimensions of the soil box were set, the sides and bottom were meshed with shell elements, leaving the top open. Then, 3D hexahedral elements measuring 25 mm a side were created inside the box and converted into SPH elements. This was repeated to create five boxes of appropriate sizes for the 5 km/h to 60 km/h range of speeds. Finally, the SPH material parameters calibrated for upland sandy loam in Chapter 4 were applied to the newly created SPH elements and the soil boxes were completed.

To connect the different parts in the simulation (rim, tire, soil, and soil box), three contact definitions were created, as shown in Figure 5.6. The tire-rim contact definition was identical to that described in Chapter 3 [107]. The tire-soil contact was a non-symmetric node-to-segment (Type 34 in PAM-CRASH) with the tire as the master and the soil SPH particles as the slave. All of the parts on the outside surface of the tire were included in the tire side of this contact, to account for the possibility of the tire sinking into the soil, but the rim was excluded. This contact had a thickness of 5.0 mm and a friction coefficient of 0.6. Finally, a second non-symmetric contact definition was added between the soil SPH particles and the soil box, this time with

a thickness of 2.0 mm and a friction coefficient of 0.6. Table 5.2 compares the contact definitions for the hard surface and soil simulations.

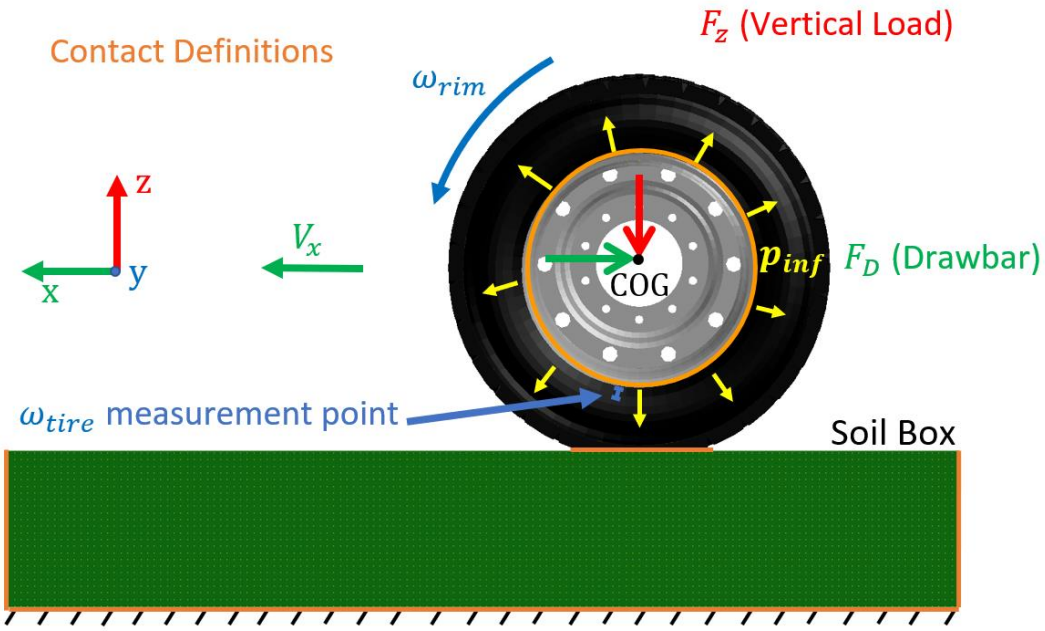

Figure 5.6: Tire-rim slip simulation setup on soil with key parameters, soil box, and contact definitions in orange [115].

Table 5.2: Comparison of contact definitions in soil and hard surface simulations

Contact Definition	**Soil**		**Hard Surface**	
Tire-rim	Type	symmetric (Type 33)	Type	symmetric (Type 33)
	Thickness	0.5 mm	Thickness	0.5 mm
	Friction coefficient	0.05 – 0.9	Friction coefficient	0.05 – 0.9
Tire-road/ tire-soil particles	Type	non-symmetric (Type 34)	Type	non-symmetric (Type 34)
	Thickness	5.0 mm	Thickness	5.0 mm
	Friction coefficient	0.6	Friction coefficient	1.0
	Master	outside of tire	Master	road
	Slave	soil SPH particles	Slave	tread
Soil box-soil particles	Type	non-symmetric (Type 34)		
	Thickness	2.0 mm		
	Friction coefficient	0.6		
	Master	soil box		
	Slave	soil SPH particles		

Another significant change was reducing the initial solver timestep from 0.001 s down to 1e-6 s. This allowed the small-scale motion of the soil particles to be accurately simulated, and greatly increased the runtime as well as the density of the datapoints in the results (about 50x).

The same five simulation parameters varied for the hard surface tests (tire-rim friction coefficient, drawbar load, inflation pressure, vertical load, and longitudinal wheel speed) were again varied for the soil to determine their independent effects on the amount of tire-rim slip, which was measured by the rim-slip quantity i_{rim}. i_{rim} was determined using Eq. 3.5 the exact same way as described in Chapter 3 for the hard surface tests. There were, however, two small changes made to the test order and the drawbar load due to discovered effects of the soil. The first change was to investigate the effect of the longitudinal wheel speed on i_{rim} first, since the

longitudinal wheel speed had a significant impact on the size of the soil boxes and number of SPH particles, and therefore the runtime of the simulations. No significant effect on i_{rim} was found, therefore small soil boxes with a default longitudinal wheel speed of 10 km/h were used. The second change was using 60% as the default drawbar load value on the soil. Preliminary simulations and the longitudinal wheel speed results showed that tire-rim slip occurred at a lower drawbar load of 60% on the soil compared to 90% for the hard surface tests, when all the other conditions were the same. Therefore, the lower drawbar load of 60% was more likely to yield interesting results since it was closer to the 0% to 100% rim-slip transition point. Simulations at 896 kPa were also not done because they were expected to have 0% rim-slip based on the hard surface results.

In order to investigate the independent effects of the parameters, two parameters at a time were varied through a particular range, while the other three parameters were kept at their default value. Table 5.3 lists all five simulation parameters varied for the soil tests, as well as their symbols, units, ranges, and default values. Only a limited sample of the possible combinations of parameter values were tested due to the time required to run each simulation, as the goal was to determine independent effects.

Table 5.3: Parameters varied for tire-rim slip simulation on soil

Parameter	**Symbol**	**Unit**	**Range**	**Default Value**
Tire-Rim Friction Coefficient	μ	none	0.05 – 0.9	0.2
Drawbar Load	F_D	%	20 – 90	60
Inflation Pressure	p_{inf}	kPa	276 – 758	379
Vertical Load	F_z	kN	13 – 41	41
Longitudinal Wheel Speed	V_x	km/h	5 – 60	10

5.2.2 Effect of Longitudinal Wheel Speed

The first parameter varied was the longitudinal wheel speed, V_x. The amount of rim-slip was determined at five discrete longitudinal wheel speed values between 5 and 60 km/h, representing slower off-road driving speeds. Three different drawbar loads of 20%, 40%, and 60% were also tested to demonstrate the relative effect of the

longitudinal wheel speed compared to the other parameters. Results from the longitudinal wheel speed variation tests are shown in Figure 5.7 below.

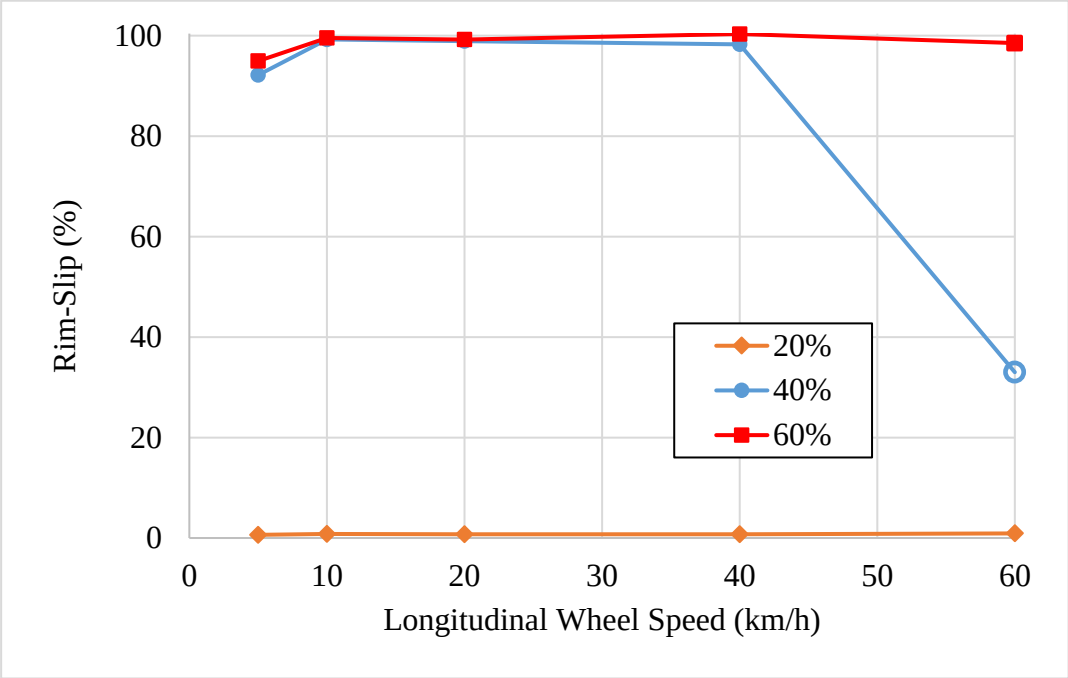

Figure 5.7: Effects of longitudinal wheel speed and drawbar load on rim-slip for soil [115]. The other parameter settings were 379 kPa inflation pressure, 0.2 tire-rim friction coefficient, and 41 kN vertical load.

First, it is obvious from the generally flat lines in Figure 5.7 that varying the longitudinal wheel speed had minimal effect on the amount of rim-slip. This was partly due to the way that i_{rim} was defined, as mentioned previously in section 5.1. However, it appears that changing the longitudinal wheel speed at very low speeds (5 km/h to 10 km/h) for the 40% and 60% drawbar loads did result in a small increase in the rim-slip from approximately 92% to 100%.

The other standout feature of Figure 5.7 is the outlier datapoint with the hollow circle, occurring at 60 km/h with a 40% drawbar load. In this particular simulation, the tire did not reach a steady-state rim-slip condition. Instead, the angular velocity of the rim varied continuously for a short period of time, before the tire bead elements entangled with the rim and they continued to rotate together at the same angular velocity. Due to this unusual and unstable behaviour, this simulation was treated as

an outlier, and it was represented in Figure 5.7 with an average rim-slip value from a selected range of time-steps. A likely reason for this unsteady behaviour is that the rotational frequency of the model at 60 km/h was close to a vibration mode, and thus there was too much oscillation in the tire bead for the tire-rim contact to be stable.

The drawbar load noticeably had a much larger effect on the rim-slip than the longitudinal wheel speed, because changing the drawbar load from 20% to 40% resulted in the rim-slip changing from 0% to about 100%. A lower range of drawbar loads (20% to 60%) was used for the longitudinal wheel speed tests on soil compared to the hard surface tests in section 5.1 (40% to 90%), since it was apparent early on that rim-slip occurred on the soil at lower drawbar loads. A range of 40% to 90% was therefore anticipated to result in 100% rim-slip for all of the drawbar loads, which would have added little information to Figure 5.7. Finally, the drawbar load also contributed to the unsteady outlier, since it only occurred at the intermediate drawbar load of 40%.

5.2.3 Effects of Tire-Rim Friction Coefficient and Drawbar Load

The next parameters varied were the tire-rim friction coefficient and the drawbar load. The same parameter ranges (0.05 to 0.9 and 30% to 90%) were used as for the hard surface tests in section 5.1. The effects on rim-slip of varying these parameters together are shown in Figure 5.8.

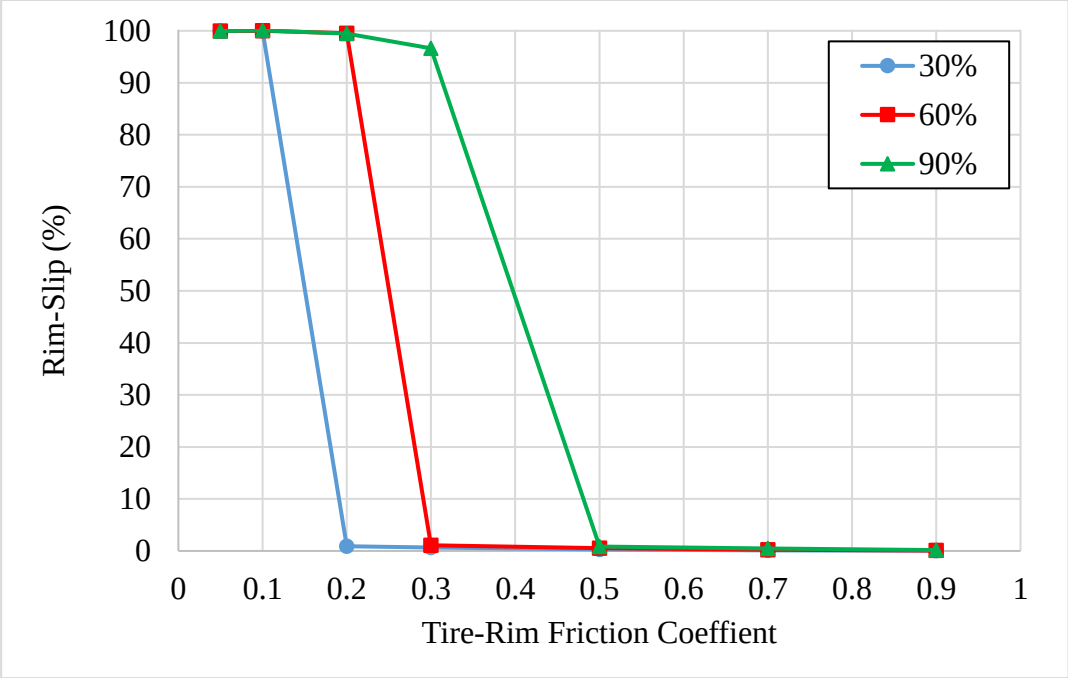

Figure 5.8: Effects of tire-rim friction coefficient and drawbar load on rim-slip for soil [115]. The other parameter settings were 379 kPa inflation pressure, 10 km/h longitudinal wheel speed, and 41 kN vertical load.

There is a clear and consistent trend across all three drawbar loads where increasing the tire-rim friction coefficient decreases the rim-slip. This decrease also happens abruptly, around a particular threshold value of the tire-rim friction coefficient that depends on the drawbar load. For example, for the 60% drawbar load, increasing the friction coefficient from 0.2 to 0.3 decreases the rim-slip from 100% to 0%, therefore the threshold value would be between 0.2 and 0.3.

In addition, increasing the drawbar load increases the rim-slip, or more specifically, increases the friction coefficient threshold value. For example, for the 60% drawbar load, the rim-slip drops to 0% after the friction coefficient reaches a threshold value of 0.3. On the other hand, for the 90% drawbar load, a larger friction coefficient threshold value of 0.5 is required to prevent rim-slip. Similar physical mechanisms to those described in section 5.1, namely the concept of a frictional torque threshold, can explain the effects of the tire-rim friction coefficient and drawbar load on rim-slip shown in Figure 5.8.

5.2.4 Effects of Vertical Load and Inflation Pressure

The last two parameters varied were the vertical load and the inflation pressure. The same range of vertical loads (13 kN to 41 kN) was used as for the hard surface tests in section 5.1. However, the range of inflation pressures was truncated slightly to 276 kPa to 758 kPa, since it was assumed there would continue to be 0% rim-slip at the higher inflation pressure of 896 kPa and no new information would be gained by doing at simulation at this inflation pressure. Figure 5.9 shows the combined effects of varying the vertical load and inflation pressure on the rim-slip.

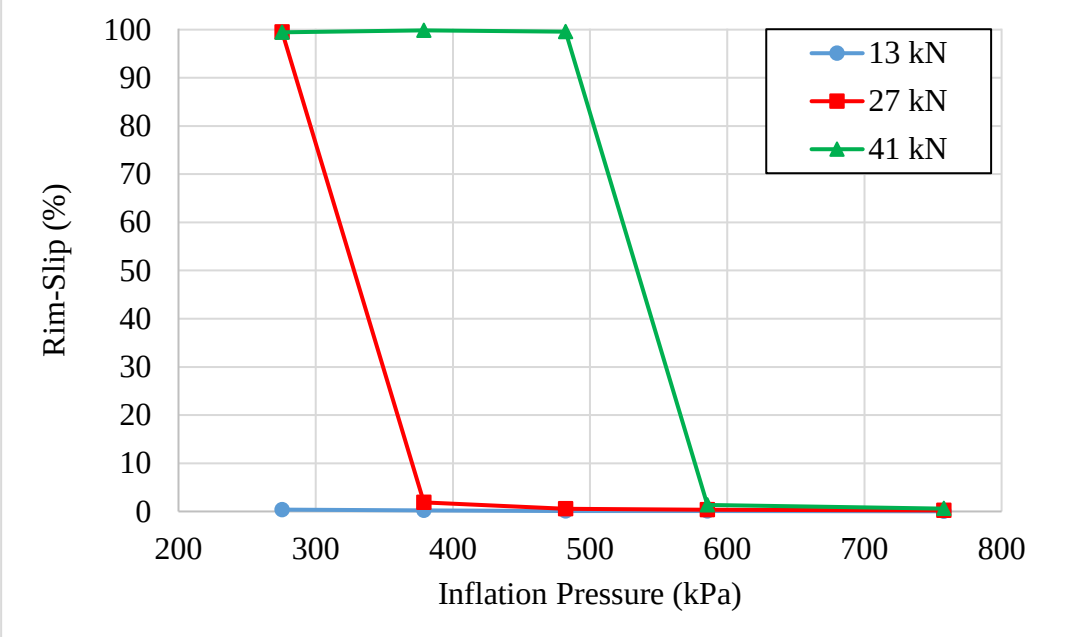

Figure 5.9: Effects of vertical load and inflation pressure on rim-slip for soil [115]. The other parameter settings were 60% drawbar load, 0.2 tire-rim friction coefficient, and 10 km/h longitudinal wheel speed.

The main effect of the vertical load on rim-slip was that a larger vertical load resulted in more rim-slip. This effect is visible in Figure 5.9, as at a given pressure of 482 kPa, the 13 kN and 27 kN vertical loads have 0% rim-slip, while the larger 41 kN load has 100% rim-slip. The intermediate 27 kN vertical load also reached 100% rim-slip once the inflation pressure was lowered to 276 kPa, while the smallest 13 kN vertical load never experienced any rim-slip.

The opposite trend for the inflation pressure is visible in Figure 5.9, as a higher inflation pressure resulted in less rim-slip. This trend was not contradicted by any of the three tested vertical loads, although a higher vertical load did result in a higher threshold value for the inflation pressure where the rim-slip transitions rapidly from 0% to 100%. Similar explanations to those in section 5.1 can explain these trends, based on the concept of a frictional torque threshold. It is important to note that tire-rim slip only occurred in the tested conditions at low inflation pressures of around 482 kPa or lower, which is substantially lower than the RHD tire's rated inflation pressure of 896 kPa. Thus, tire-rim slip on soil is a phenomenon associated with low tire pressures and high vertical loads.

5.3 Comparison of Tire-Rim Slip on Hard Surface and Soil

To have a better idea of how the different soil terrain affected the tire-rim slip, it was instructive to do a direct comparison. The appropriate parameter variation figures from the previous sections are shown again side-by-side for convenience.

5.3.1 Effect of Longitudinal Wheel Speed

The first results compared were for the longitudinal wheel speed variation, shown in Figure 5.10. It is clear that the longitudinal wheel speed had negligible effect for both the soil and hard surface, due to the horizontal lines in Figure 5.10. What is interesting is that the 40% and 60% drawbar loads had 0% rim-slip the hard surface (Figure 5.10b), but 100% rim-slip on the soil. This pattern strongly indicates that tire-rim slip is more likely and occurs at lower loads on the soil than on the hard surface.

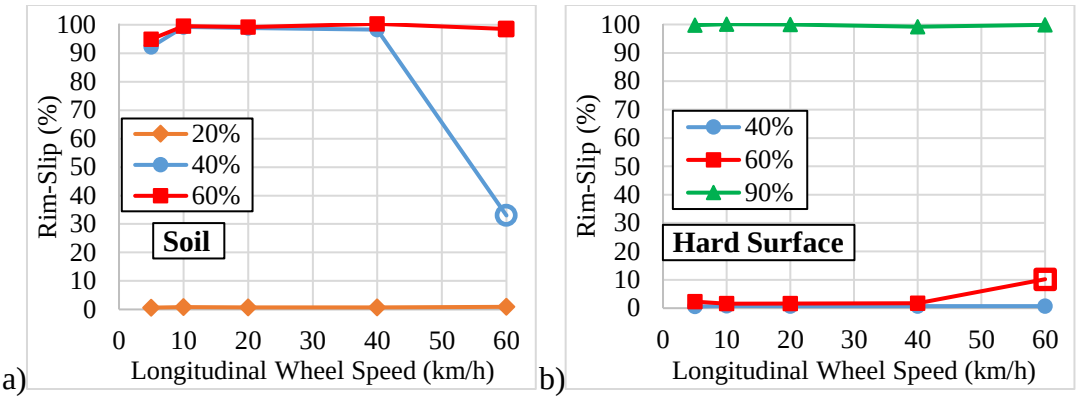

Figure 5.10: Effects of longitudinal wheel speed and drawbar load on rim-slip for a) soil [115] and b) hard surface [107]. The other parameter settings were 379 kPa inflation pressure, 0.2 tire-rim friction coefficient, and 41 kN vertical load.

There was also an unsteady outlier simulation occurring at 60 km/h for both the soil and the hard surface, which suggests it was not a one-off occurrence, but instead was a phenomenon tied to the 60 km/h longitudinal wheel speed. The outlier also occurred at a 60% drawbar load for the hard surface, compared to only a 40% drawbar load for the soil, which further supports the idea that equivalent rim-slip behaviour occurs at a lower drawbar load on the soil. In summary, comparing the longitudinal wheel speed variation results indicates that it has the same effect for both terrains, and that tire-rim slip occurs at a lower drawbar load for the soil.

5.3.2 Effects of Tire-Rim Friction Coefficient and Drawbar Load

The next results compared were for the tire-rim friction coefficient and drawbar load variation, as shown in Figure 5.11. For both the soil and hard surface, increasing the tire-rim friction coefficient decreased the rim-slip, with a noticeable threshold effect. In contrast, increasing the drawbar load for both terrains increased the rim-slip, as shown by the 90% drawbar load (green line) always reaching 100% rim-slip first as the tire-rim friction coefficient decreased.

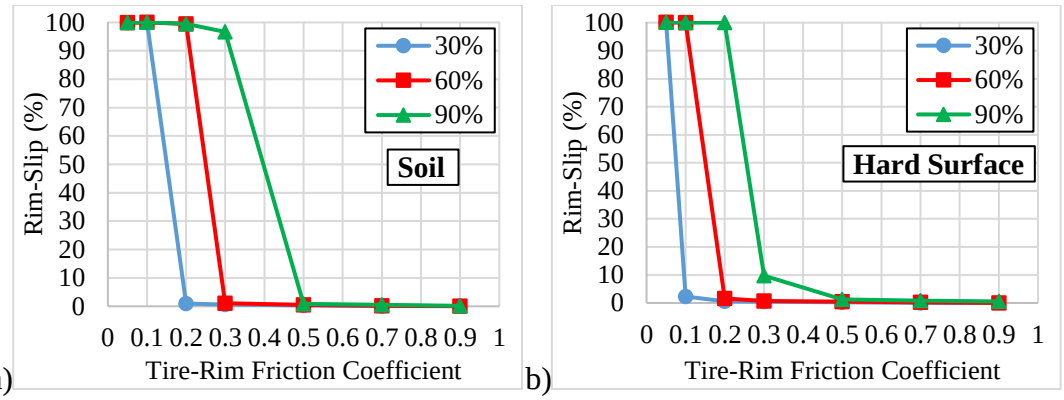

Figure 5.11: Effect of tire-rim friction coefficient and drawbar load on rim-slip for a) soil [115] and b) hard surface [107]. The other parameter settings were 379 kPa inflation pressure, 10 km/h longitudinal wheel speed, and 41 kN vertical load.

The main difference between the soil and hard surface results was not so much the shape of the curves, but their position. The curves for the rim-slip on soil in Figure 5.11a are shifted to the right compared to the hard surface curves in Figure 5.11b. For example, on the soil at 90% drawbar load and 0.3 friction coefficient, there is 97% rim-slip, while for the same point on the hard surface there is only 10% rim-slip. This difference indicates that for a given drawbar load, the friction coefficient threshold value is higher on soil compared to the hard surface. In practical terms, this means that while the trends are the same, more tire-rim slip will occur on the soil for a given set of conditions.

5.3.3 Effects of Vertical Load and Inflation Pressure

In Figure 5.12 the effects of the vertical load and inflation pressure are compared for the two terrains. At first glance, the two graphs appear almost identical, with the only difference that the 27 kN, 379 kPa data point has 97% rim-slip on the hard surface and 2% on the soil. The trends and shapes are the same: rim-slip increases with increasing vertical load and decreases with increasing inflation pressure. However, there is an important difference in that the hard surface results were done at a 90% drawbar load, while the soil results were done at only a 60% drawbar load. This difference means that a significantly lower drawbar load on the soil yielded the same amount of rim-slip as on the hard surface, supporting the conclusion that tire-rim slip occurs at lower loading conditions on the soil.

a) 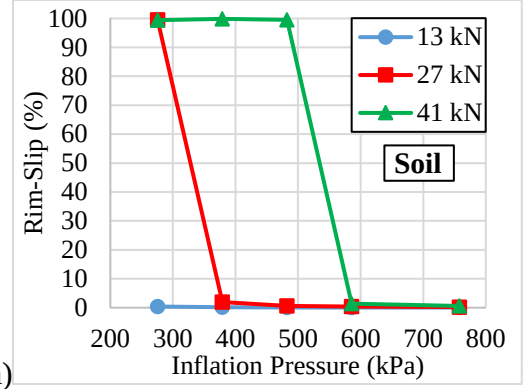

b) 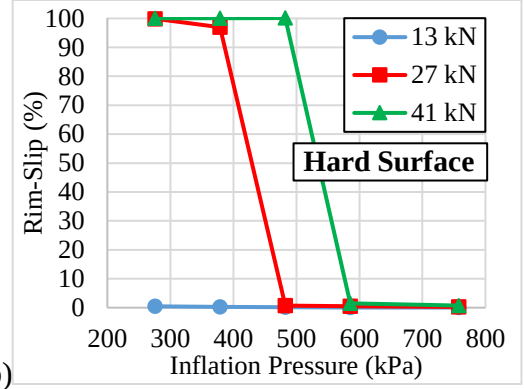

Figure 5.12: Effect of vertical load and inflation pressure on rim-slip for a) soil [115] and b) hard surface [107]. The other parameter settings were 60% drawbar load (soil), 90% drawbar load (hard surface), 0.2 tire-rim friction coefficient, and 10 km/h longitudinal wheel speed.

5.4 Chapter Summary

In this chapter, tire-rim slip tests were designed and simulated on a hard surface and an upland sandy loam soil. The same five parameters (tire-rim friction coefficient, drawbar load, inflation pressure, vertical load, and longitudinal wheel speed) were varied for both terrains and their independent effects were described. The main insights from these simulations were:

1. Increasing the vertical and drawbar loads increased the rim-slip.
2. Increasing the inflation pressure and tire-rim friction coefficient decreased the rim-slip.
3. There was a threshold effect where the rim-slip quickly changed from 0% to 100% at a particular parameter value.
4. The longitudinal wheel speed had negligible effect, except for an unstable outlier occurring at 60 km/h and the default drawbar load.
5. The trends and independent effects of the five parameters varied were the same for both terrains.
6. The rim-slip behaviour was very similar for both terrains, with both a threshold effect observed for each parameter and an unstable outlier result.

7. Tire-rim slip generally occurred at a lower drawbar load on the soil compared to the hard surface (e.g. 60% vs. 90%).

The results of the tire-rim slip simulations suggested that vibration and natural frequencies played an important role in the simulation of tire-rim slip for a driven tire. Specifically, a certain longitudinal wheel speed or rotation frequency and a change in the damping of the system due to the addition of soil SPH particles were observed to have significant effects on the tire-rim slip behaviour. This connection between tire-rim slip and damping was corroborated by a hard surface test where the sidewall nodal damping factor was artificially increased from 2.90 to 100, which resulted in 100% rim-slip. These insights can be used to guide future investigation into tire-rim interaction phenomena, especially with regards to the effect of different terrains. The rim-slip data collected will also be useful for training tire-rim slip prediction models, such as the neural network described in Chapter 6.

Chapter 6. Tire-Rim Slip Prediction

This chapter will cover the design and training of a neural network-based virtual sensor for the prediction of tire-rim slip. Included is the collection of training and testing data, the network design and hyperparameter selection, a comparison of the trained networks' performance, and finally a discussion of insights gained and future work.

6.1 Data Collection

Part of the rim-slip dataset used for training and testing the neural network came from the tire-rim slip simulations conducted in Chapter 5. The speed variation results were not included since the longitudinal wheel speed was found to have negligible effect on the amount of rim-slip [107], [115]. After removing duplicated conditions, there were 92 usable data points, 47 on the upland sandy loam soil and 45 on the hard surface. In order to obtain a larger dataset for training, an additional set of 80 simulations was run with parameters varied according to Table 6.1. In order to maximize the range of training data available, the pressure variation simulations were re-run for both the hard surface and the soil, this time using non-default values for the tire-rim friction coefficient, drawbar load, and vertical load. The simulations were evenly divided between the different possible combinations of parameters (inflation pressure, tire-rim friction coefficient, drawbar load, vertical load, and terrain) for a total of $5 \times 2 \times 2 \times 2 \times 2 = 80$ data points. The longitudinal wheel speed remained constant a 10 km/h because it had negligible effect. With the additional simulations, there were now a total of 172 data points available, to ensure good training of the proposed neural network. Finally, in order to provide a fair test of the trained network's performance in predicting tire-rim slip, another set of 20 simulations were run with particular combinations of parameters and parameter values that did not appear in the training dataset. For example, several simulations were done with an extra high vertical load of 44 kN, or an intermediate drawbar load of 50%. Table 6.1 lists the parameters varied for the testing dataset simulations.

Table 6.1: Parameters varied for additional training and testing simulations

Parameter	Symbol	Unit	Training Sim Values	Testing Sim Values
Tire-Rim Friction Coefficient	μ	none	0.05, 0.9	0.05 – 0.9
Drawbar Load	F_D	%	30, 60 (hard surface), 90 (soil)	20 – 90
Inflation Pressure	p_{inf}	kPa	276 – 896	276 – 896
Vertical Load	F_z	kN	13, 27	13 – 44
Longitudinal Wheel Speed	V_x	km/h	10	10
Terrain	none	none	hard surface (1), soil (2)	hard surface (1), soil (2)

Out of the 6 parameters shown in Table 6.1, 5 were chosen as input variables for the neural network: terrain type, tire-rim friction coefficient, inflation pressure (kPa), drawbar load (%), and vertical load (kN). The longitudinal wheel speed was excluded due to its negligible effect. Several assumptions were made about using these parameters as input variables for the proposed virtual sensor. First, it was assumed that the tire inflation pressure, vertical load, and drawbar load would be known a priori from loading the truck in question. The tire-rim friction coefficient would also be estimated in advance based on the bead lubrication and mounting quality of the tire. An advanced commercial truck could also include sensors for predicting the terrain type [116]. These assumptions represent the ideal case where an advanced commercial truck would have all of the necessary information available to make use of the proposed virtual sensor for tire-rim slip. Practical implementation would require additional effort to ensure that the virtual senor has the required quantity and quality of sensor data as well as appropriate computer hardware.

As seen in Table 6.1, the terrains were coded as 1 (hard surface) or 2 (soil) in order to facilitate processing by the neural network. This allows for the possibility of adding more terrains to the rim-slip training dataset in the future. No scaling or normalizing was applied to the data, since the parameter values were in reasonable proximity to one another. The output or target variable in all cases was the rim-slip

as a percentage between 0 and 100. The complete parameter variation and additional training and testing datasets are included in Appendix A.

6.2 Neural Network Design

There are many possible virtual sensor designs, as described in Chapter 2. A neural network was chosen for the present research due to the type of data available, and the broad relevance of neural network design techniques to multiple fields. The data available from the tire-rim slip simulations consisted of 192 data points, each with 5 input variables and 1 output variable, and all of the data were from steady-state simulations with no time dependencies between them. Therefore, the proposed neural network would serve as a black box virtual sensor relating the 5 input variables to the rim-slip output, as an average value for steady-state conditions or an approximate value under transient conditions. Data collection from experiments or simulations under transient conditions is a possibility for future research, but was considered too labour intensive for the scope of the current research.

The amount of data available also limited the depth of the neural network. Contemporary deep neural networks (DNNs) typically consist of 100s of neurons with 1000s of weights, which require 1000s of data points to train properly [83], [117]. Therefore, it was decided to use a shallow neural network appropriate to the size of the available data. Such a shallow network would have additional benefits of a rapid training time and minimal computational requirements for online output calculation.

The software of choice for designing the shallow neural network was MATLAB's Deep Learning Toolbox™ [118]. A custom script was written to create shallow feedforward neural networks of varying sizes, train them on the rim-slip dataset, and save the training records and regression performance results. The training was done in 3 phases: phase 1 tested multiple combinations of hyperparameters, phase 2 tested the top combinations from phase 1 on a reduced dataset, and phase 3 validated the performance of the top networks from phase 2.

6.2.1 Hyperparameters

In phase 1, the script trained 9 different neural networks in a row with 1, 2, or 3 hidden layers containing 10, 20, or 30 neurons each. All of the hidden layers were the same size and contained the same type of neuron. This meant that the smallest network included only 10 neurons, while the largest included 90. Figure 6.1 shows a schematic of the proposed neural network with the inputs, output, and hidden layers.

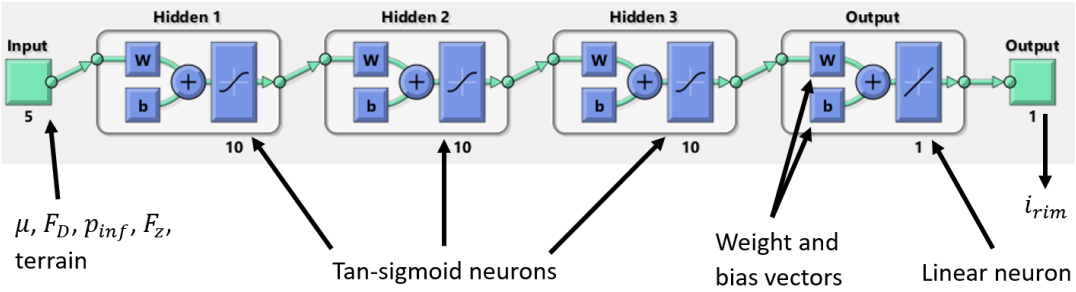

Figure 6.1: Schematic of example shallow neural network for rim-slip prediction with 3 hidden layers and 10 neurons per layer.

6.2.2 Neuron Type and Initialization

All of the neurons in the hidden layers used a tan-sigmoid activation function while the single neuron in the output layer used a linear activation function [118]. Each layer was fully connected, with each neuron connected to each output from the preceding layer with a single weight. There was also a bias vector for each layer, with one bias value per neuron. All of the neural network's weights, biases, and equations are detailed in Appendix B. The weights and biases were initialized with the Nguyen-Widrow algorithm [119], [120]. This algorithm trains networks faster and more efficiently than purely random initialization by spreading the values out across the input range of the activation function. Essentially, the input range is randomly and approximately evenly divided into intervals, one per neuron, by randomly choosing the weights and biases within specific ranges. This ensures that none of the neurons are wasted, since they each contribute to modelling part of the activation function's range, and speeds up training by reducing the movement of each neuron's effective interval required to reach its optimum position [120]. The Nguyen-Widrow algorithm only works for activation functions with a finite input

range, therefore purely random initialization was used for the weights and bias for the output layer neuron with the pure linear activation function [119].

6.2.3 Training Method

Each network was trained with both the Levenberg-Marquardt (L-M) and Bayesian Regularization (BR) training functions. These two methods are explained in detail below. Most neural network training methods use a backpropagation approach, where the error for the current outputs is fed backwards through the layers, and the weights are updated based on some function of the error corresponding to that part of the network. For continuous, differentiable transfer functions this reduces to a multidimensional gradient descent problem, that is, finding which values of the weights and biases minimize the MSE, or are at a minimum of the performance surface. The L-M training method was progressively developed from insights on gradient descent heuristics from Levenberg in 1944 [121] and Marquardt in 1963 [122]. Essentially, it combines the benefits of basic gradient descent and Newton's method by scaling the gradient according to the curvature to ensure that the algorithm takes small steps when the gradient is large, and large steps when the gradient is small. One downside of L-M is that the matrix calculations involved require very large quantities of memory for training larger networks with thousands of weights [123], [124].

In MATLAB, both the L-M and BR training functions use the L-M gradient descent method during the backpropagation calculation, but have different methods for generalization. For L-M, early stopping is used, whereby the training stops after the MSE on the validation data set increases for a set number of consecutive epochs, and the network returned is from the epoch with the minimum validation MSE [124]. Early stopping is sensitive to the selection of the validation dataset, since a non-representative validation dataset will artificially increase the validation error. The default stopping point of 6 epochs of validation MSE increase was used for this research.

The BR training method improves generalization by adding an extra term representing the mean squared sum of the weights and biases (MSW) to the

performance function (Eq. 6.1). Normally, the training algorithm minimizes only the MSE of the network's output, but including the additional term results in a corresponding minimization of the weight and bias values, which improves smoothness and generalization [124], [125]. The difficult part of this regularization approach is weighing the importance of minimizing the weights and biases versus minimizing the MSE by selecting an appropriate weighing parameter λ. Bayesian methods are thus used to estimate the variance of the unknown weights and biases in order to optimize λ [125], [126]. BR training has better performance on small datasets, since there is no need to separate out a validation subset. However, the more complex performance function also requires more epochs for convergence to occur [124].

$$perf = \lambda \times MSW + (1 - \lambda) \times MSE \tag{6.1}$$

6.2.4 Data Division

The data division was different for different phases and training algorithms. Generally, the rim-slip dataset was divided into three subsets: training, validation, and testing. For phase 1, the rim-slip training dataset with 172 data points was randomly sorted and the first 30 data points were chosen for validation, with the remaining 142 used for training. The additional 20 data points with new combinations of operating conditions comprised the testing dataset. This resulted in a final 75%/15%/10% training/validation/testing split. The testing data was not seen by the network until after the training was complete. In phase 2, a reduced dataset was used, and the 172-point dataset was randomly divided with a 70%/15%/15% training/validation/testing split. Thus, when the trained networks were tested again on the 20-point testing dataset, there was no way that the testing data could have influenced the training. The threefold data division applied only to the L-M trained networks, for the BR trained networks the validation dataset was added to the training dataset, since the BR training algorithm does not have a validation step.

6.2.5 Results Metrics

The results metrics used for network performance evaluation included MATLAB's performance function, the best validation/training MSE, and Pearson's correlation coefficients (R's) for the different datasets data. MSE histories, error histograms, and regression plots provided supplementary visualizations of performance. Indicators of good performance were low performance functions, low validation/training MSE's, a histogram with mostly zero error, and regression plots with correlation coefficients as close to 1.0 as possible. The main metrics used for comparison were the correlation coefficients for the testing and overall datasets, since they represented the real-world performance of the network. The other performance metrics, such as low performance functions, tended to cluster together with high testing and overall correlation coefficients.

6.3 Neural Network Performance Comparison

Due to the randomization present in the weight and bias initialization and the data division, the performance of the trained networks was not always the same, even for the same set of hyperparameters. Therefore, in phase 1, each hyperparameter combination was trained 5 times in order to mitigate the effect of the random data division and provide a better comparison of the different hyperparameter combinations. Table 6.2 below shows the performance metrics of the different networks trained in phase 1, averaged over the 5 runs.

Table 6.2: Phase 1 neural network performance

Training Method	# of Hidden Layers	Neurons per Layer	MATLAB Performance Function	Best Validation /Training MSE	Correlation Coefficient (R)				
					Training	Validation	Testing	Overall	Rank
L-M	1	10	250.201	324.482	0.94640	0.90925	0.90702	0.93873	good
L-M	1	20	413.934	532.261	0.95599	0.86324	0.61589	0.90158	poor
L-M	1	30	420.027	569.205	0.95019	0.84772	0.55810	0.89679	poor
L-M	2	10	192.284	470.389	0.98472	0.86736	0.82069	0.95359	**best**
L-M	2	20	380.898	599.691	0.94551	0.83556	0.67963	0.90616	average
L-M	2	30	710.684	926.627	0.91195	0.77259	0.43460	0.82743	worst
L-M	3	10	307.909	563.458	0.97206	0.84598	0.67246	0.92609	average
L-M	3	20	347.251	567.210	0.95865	0.84995	0.65748	0.91563	average
L-M	3	30	437.289	850.314	0.95798	0.79888	0.50841	0.89314	poor
BR	1	10	234.021	126.345	0.96998	n/a	0.80589	0.94572	poor
BR	1	20	191.130	89.006	0.97901	n/a	0.79572	0.95502	poor
BR	1	30	213.013	120.890	0.97136	n/a	0.80033	0.94934	poor
BR	2	10	58.274	3.02E-05	1.00000	n/a	0.90917	0.98749	average
BR	2	20	4.499	1.99E-11	1.00000	n/a	0.98923	0.99895	average
BR	2	30	4.546	4.73E-08	1.00000	n/a	0.98706	0.99892	average
BR	3	10	0.209	6.52E-06	1.00000	n/a	0.99948	0.99995	**best**
BR	3	20	0.925	2.94E-08	1.00000	n/a	0.99770	0.99978	good
BR	3	30	0.580	1.43E-07	1.00000	n/a	0.99834	0.99986	good

The colour coding in Table 6.2 indicates the best performance metrics with green, and the worst with red. Based on this comparison, the top performing networks on average were the 2x10 (2 hidden layers, 10 neurons per layer) network for the L-M training method, and the 3x10 network for the BR training method. The 2x10 network was chosen as the top L-M trained network because it had the highest average overall correlation coefficient, and it also had the best single run, with testing and overall correlation coefficients of 0.99981 and 0.98654. For the BR training method, additional layers consistently increased the network's performance, with the 3-layer networks having the highest correlation coefficients. The 3x10 network was considered as the best BR trained network, since having more than 10 neurons per layer increased the complexity with minimal change in performance. Even though the BR trained 3x10 network had higher correlation coefficients, the 2x10 L-M trained network was also included in phase 2 to determine if comparable performance could be obtained with a smaller network.

In phase 2, a slightly different method was used to train and validate the 2x10 and 3x10 networks, to ensure there was no possible way for the network to see the testing dataset during training. The 172-point training dataset was randomly divided

70%/15%/15% into training, validation, and testing subsets, which allowed the trained network to be checked separately on the 20-point test dataset in phase 3. Again, because of the random selection of the subsets, each of the 2x10 and 3x10 networks was trained 10 different times in order to obtain a network with a high performance. Table 6.3 shows the performance results from phase 2.

Table 6.3: Phase 2 neural network performance

Training Method	# of Hidden Layers	Neurons per Layer	Run #	MATLAB Performance Function	Best Validation /Training MSE	Correlation Coefficient (R)				
						Training	Validation	Testing	Overall	Rank
L-M	2	10	1	1069.983	1303.368	0.73472	0.70840	0.57147	0.70677	worst
L-M	2	10	2	155.152	91.461	0.99972	0.98249	0.79778	0.96468	good
L-M	2	10	3	784.919	953.770	0.86269	0.70668	0.70868	0.81373	poor
L-M	2	10	4	457.653	1038.118	0.94485	0.68578	0.73204	0.88763	average
L-M	2	10	5	60.058	20.429	1.00000	0.99510	0.92315	0.98593	**best**
L-M	2	10	6	445.763	375.350	0.94876	0.89058	0.62792	0.89077	average
L-M	2	10	7	303.014	981.110	0.96533	0.78418	0.91002	0.92681	average
L-M	2	10	8	468.360	513.918	0.91599	0.88910	0.70845	0.88476	average
L-M	2	10	9	529.862	1258.505	0.90712	0.70407	0.91141	0.87050	poor
L-M	2	10	10	260.066	695.130	0.97649	0.80862	0.93008	0.94562	good
BR	3	10	1	51.151	2.71E-10	1.00000	n/a	0.91359	0.98808	good
BR	3	10	2	61.682	4.17E-06	1.00000	n/a	0.91326	0.98551	good
BR	3	10	3	26.384	4.99E-06	1.00000	n/a	0.96369	0.99383	good
BR	3	10	4	243.918	6.62E-12	1.00000	n/a	0.65665	0.94396	poor
BR	3	10	5	72.745	1.50E-06	1.00000	n/a	0.89040	0.98295	good
BR	3	10	6	100.976	2.78E-26	1.00000	n/a	0.86388	0.97694	average
BR	3	10	7	118.783	5.14E-12	1.00000	n/a	0.83794	0.97242	average
BR	3	10	8	146.978	1.26E-11	1.00000	n/a	0.78461	0.96536	average
BR	3	10	9	121.286	7.40E-06	1.00000	n/a	0.84123	0.97182	average
BR	3	10	10	0.234	4.71E-06	1.00000	n/a	0.99972	0.99995	**best**

In phase 3, the top 3 networks from each training method in phase 2 were tested against the 20-point testing dataset (phase 3 testing). The 3x10 networks did much better, as the best phase 2 2x10 network (run 5) had a phase 3 testing correlation coefficient of 0.90678, while the best phase 2 3x10 network (run 10) had a correlation coefficient of 0.92343 (Table 6.4). However, the next-best 3x10 network according to the phase 2 results had a higher correlation coefficient of 0.99956 on the phase 3 testing dataset, despite only having a correlation coefficient of 0.96369 on the phase 2 testing dataset. This network (BR trained 3x10 run 3) was chosen as the final best network, with a total correlation coefficient of 0.99431 (Figure 6.2). The weights and biases for this network are listed in Appendix B. Additional training and performance results for this network are shown in Figures 6.3-6.5.

Table 6.4: Phase 3 neural network performance

Training Method	# of Hidden Layers	Neurons per Layer	Run #	MATLAB Performance Function	Best Validation /Training MSE	Correlation Coefficient (R)				
						Training	Validation	Phase 3 Testing	Total	Rank
L-M	2	10	2	155.152	91.461	0.99972	0.98249	0.89045	0.95711	poor
L-M	2	10	5	60.058	20.429	1.00000	0.99510	0.90678	0.97973	average
L-M	2	10	10	260.066	695.130	0.97649	0.80862	0.77912	0.93124	worst
BR	3	10	1	51.151	2.71E-10	1.00000	n/a	0.99953	0.98905	good
BR	3	10	3	26.384	4.99E-06	1.00000	n/a	0.99956	0.99431	**best**
BR	3	10	10	0.234	4.71E-06	1.00000	n/a	0.92343	0.99392	good

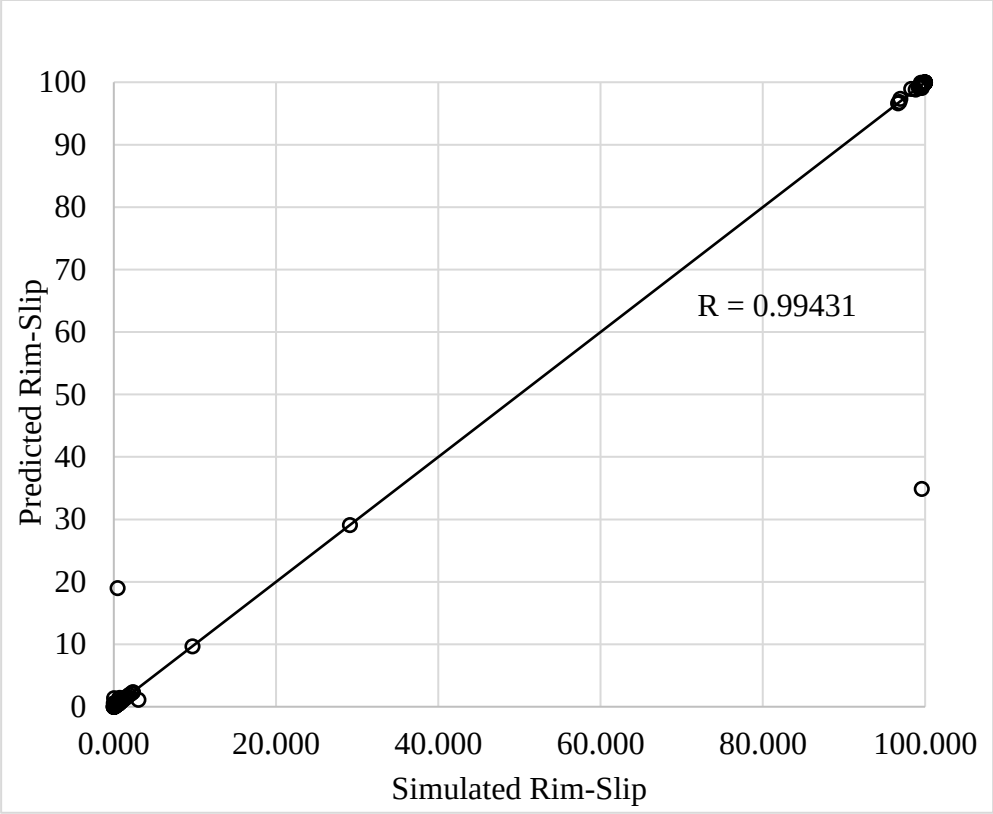

Figure 6.2: Regression plot showing correlation between simulated and predicted rim-slip values on the total dataset for the final neural network.

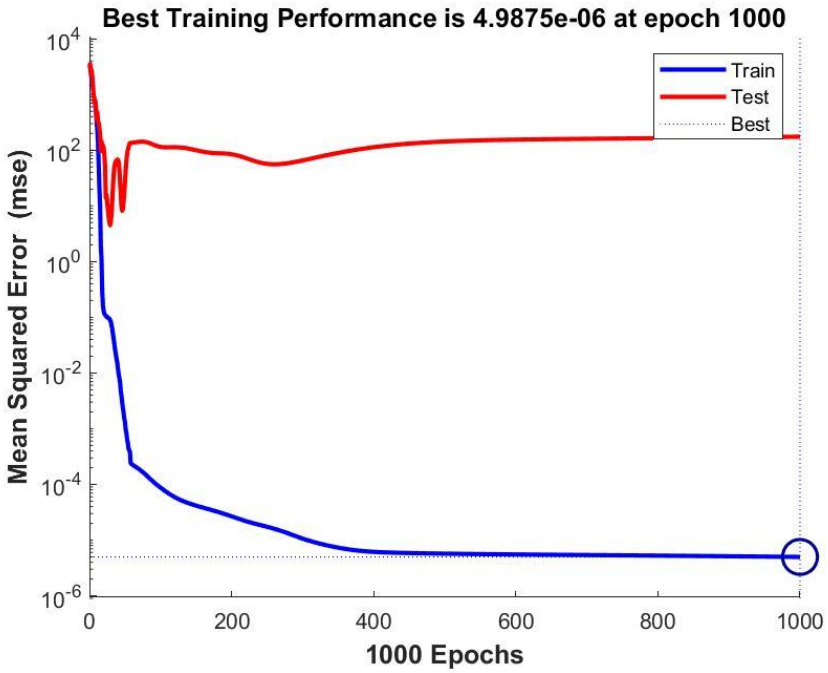

Figure 6.3: MSE performance during training of the final neural network.

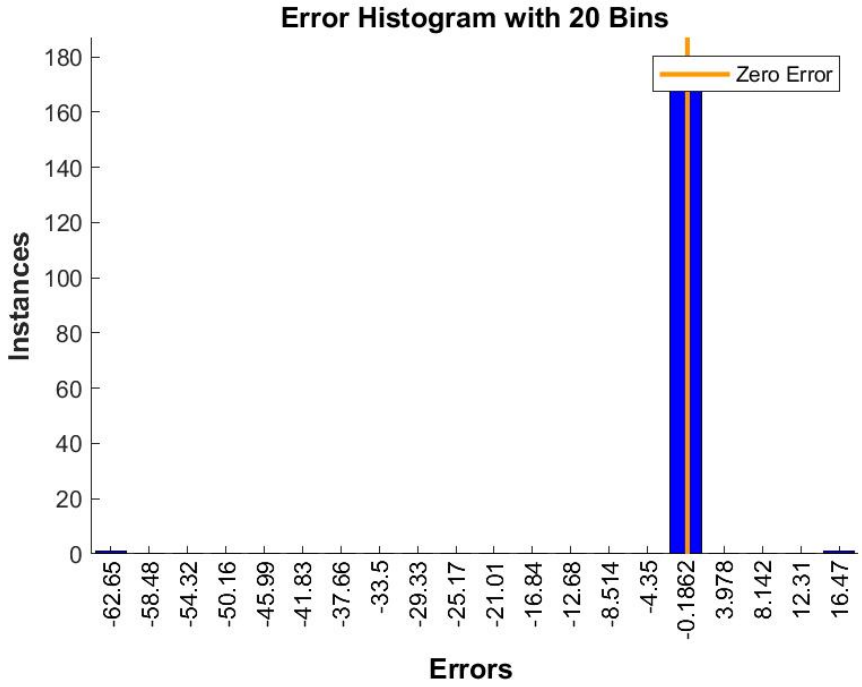

Figure 6.4: Error histogram for the final neural network.

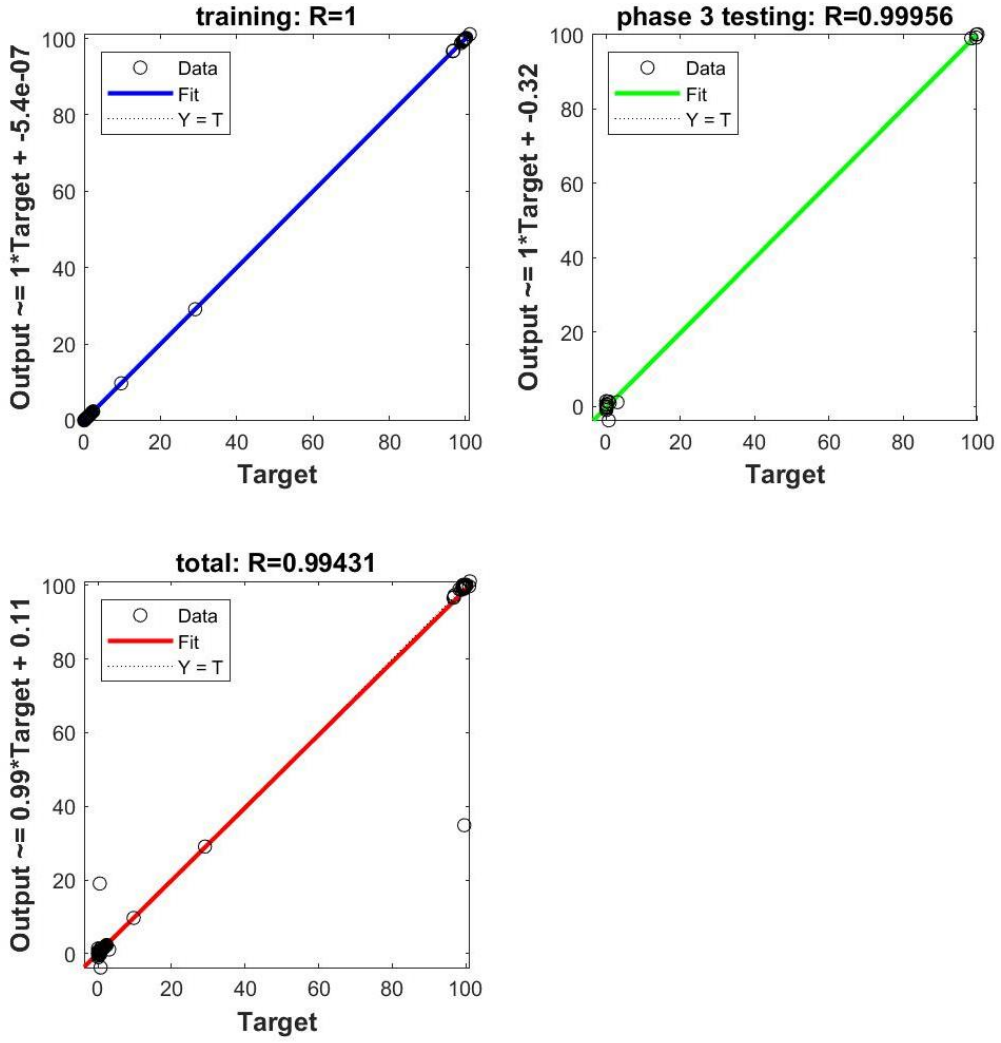

Figure 6.5: Regression plots for the training, phase 3 testing, and total datasets for the final neural network.

6.4 Results and Discussion

The neural network performance comparison demonstrated the substantial impact that random data division and weight and bias initialization has on the training of shallow neural networks. The limited rim-slip training dataset was unable to completely explore the full 5-dimensional input variable space, therefore the selection of which data points were used for training and which were used for validation or testing had a significant impact on the performance of the trained

network. This random selection effect is why multiple training runs were necessary. The effect was especially noticeable in phase 2, where the MSE of the 2x10 network varied widely from 20.429 for run 5 to 1303.368 for run 1.

In addition, the importance of input variable selection was highlighted. Originally, it was expected from theory that the drive torque variable would include all the variation of the drawbar load variable. However, that was likely not the case, since initial attempts showed that networks trained using the drive torque as the fifth input variable performed substantially worse than the ones trained using the drawbar load. For example, out of 5 training runs for a 2x10 network using the L-M training method, the best overall correlation coefficient obtained with the drive torque was 0.8984, while the same size network using the drawbar load had a 5-run average overall correlation coefficient of 0.95359 (Table 6.2). Therefore, theoretical considerations cannot be relied on perfectly when choosing which variables to include as inputs to a neural network, trial and error needs to be done as well.

The consequences of using different training methods were also apparent. The BR training method took a lot longer than the L-M method, requiring 579 s to train a 3x10 network compared to 5.2 s for the L-M method. The longer training time was because the BR training method used a performance function value of 0 as the stopping criteria, and often this high level of performance was not reached, thus the training continued until the maximum number of 1000 epochs was reached. The L-M stopping criteria of the validation error increasing for 6 epochs was much easier to reach in a small number of epochs, therefore the L-M training method was a lot faster. In contrast, the BR method took longer, due to the regularization process and higher performance goal, but achieved a much lower MSE on the training dataset, such as 10^{-6} or lower, compared to a minimum of 84.6 for the L-M method. The L-M and BR training methods had different ways of achieving good generalization, but neither one was consistently superior, as their performances on the testing dataset varied depending on the random division of the input data, as explained previously.

In general, it appeared that a midsize shallow neural network was best for modelling the rim-slip dataset. A network with a single hidden layer had trouble consistently

capturing the nonlinear relationships between the input and output variables, while the networks with over 30 neurons had the added costs of increased complexity and training time with minimal change in performance. Increasing the number of neurons in each layer did not appear to directly and consistently improve the performance. On the other hand, using the BR training method improved the correlation with both the training and testing datasets over the L-M method.

This research demonstrated that a BR-trained shallow neural network with 3 hidden layers, 10 neurons per layer, and 5 inputs was the most effective at predicting the amount of rim-slip simulated for the RHD truck tire. However, due to the significant effects of random data distribution, multiple training attempts would likely be required to obtain a network with satisfactory performance. This is not a major drawback, though, since the training times and processing requirements are very low for such a small neural network and dataset.

The final trained network, with only 30 neurons and 291 weights and biases, would likely be effective for use as a real-time virtual sensor for tire-rim slip, with the potential to be retrained to include additional terrain types. One drawback is that due to the use of a steady-state training dataset, the accuracy of the prediction would likely be limited during transient conditions. Another weakness is that implementation of the virtual sensor would require all 5 of the input variables to be measured with physical sensors in order to be available for the neural network. Some vehicle parameters, like the inflation pressure, would be easier to measure than others, like the drawbar load, and experimental work would need to be done to determine which parameters are feasible to measure. Modifications to the virtual sensor may then be required to maximize the tire-rim slip information extracted from the available physical sensors. These weaknesses provide opportunities for future research and improvement of the proposed virtual sensor.

6.5 Chapter Summary

This chapter presented the design, training, and performance comparison of a shallow neural network for predicting the rim-slip of an RHD truck tire based on various operating conditions. Additional rim-slip simulations were also performed to acquire

sufficient training and testing data. The best-performing network was BR trained with 3 hidden layers of 10 neurons each and 5 inputs. This network achieved a testing correlation coefficient of 0.96369-0.99956 and a total correlation coefficient of 0.99431. Three major influences on the network performance were discovered: the random division of training/validation/testing data, the selection of appropriate input variables, and the training method. Increased network depth also resulted in improved performance, while having larger hidden layers did not. The final trained neural network is ready for future development as a virtual sensor for tire-rim slip.

Chapter 7. Conclusions and Future Work

In this thesis, a variety of research tasks were performed in different areas including tire modelling with FEA, simulating tire-rim slip and the tire-rim interaction, terramechanics and terrain modelling, and training a neural network for virtual sensing. This section will conclude the work done in these different areas, the major contributions, limitations and lessons learned, opportunities for future work, and list the papers published.

7.1 Conclusions and Contributions

During the process of investigating and predicting tire-rim slip on different terrains using FEA, the following objectives were completed:

1. Modified an existing RHD truck tire FEA model in order to allow for the simulation of tire-rim slip.
2. Calibrated an SPH soil model for a new type of soft soil.
3. Investigated the effects of different operating conditions and terrains on tire-rim slip to determine which parameters are significant, what their effects are, and the underlying mechanisms.
4. Designed and trained a simple NN-based virtual sensor to predict the tire-rim slip based on the parameters found to have a significant effect.

Completing the above objectives resulted in the following major contributions:

1. Developed a method of simulating, measuring, and quantifying relative tire-rim slip for a rolling tire using FEA.
2. Demonstrated the qualitative effects of different operating conditions and terrains on tire-rim slip using the concept of a frictional torque threshold.
3. Designed and trained an accurate prototype neural network-based virtual sensor for predicting tire-rim slip.

The first contribution involved modifying an existing FEA truck tire model to have an additional tire-rim contact definition, and then performing multiple simulations such as drum-cleat and vertical stiffness tests to ensure that the modifications did not significantly affect the validity of the tire model. Further modifications to the simulation boundary conditions were then made to properly apply a drawbar load and induce tire-rim slip, based on the conditions for physical tests. A new quantity, called rim-slip (Eqs. 3.5 and 3.6), was also defined in order to measure the rotation of the rim relative to the tire over a large number of tire rotations, which was necessary in order to study tire-rim slip for a rolling tire.

The most interesting results were obtained from the investigation into the operating conditions affecting tire-rim slip. It was found that four of the parameters studied (tire-rim friction coefficient, drawbar load, vertical load, and inflation pressure) had a threshold effect, where the rim-slip would remain at almost zero until, for example, the inflation pressure dropped beneath a certain threshold value, after which the rim-slip rapidly increased to 100%. The fifth parameter, longitudinal wheel speed, did not have a significant effect on the rim-slip, but varying it did suggest an influence of vibration and natural frequencies on tire-rim slip. Finally, while the same rim-slip trends were observed for both the hard surface and the upland sandy loam, the threshold values were lower for the upland sandy loam, making rim-slip more likely.

The design and training of a neural network-based virtual sensor for predicting tire-rim slip demonstrated that accurate prediction with a correlation coefficient greater than 0.99 can be obtained for steady-state tire-rim slip situations. It was also shown that this accurate prediction can be achieved with a computationally efficient shallow network, as long as the correct input variables are used and the random factors in the training process are accounted for. This virtual sensor was not developed as far as other parts of the research, but it provides a solid foundation for expansion to a wider range of operating conditions and transient situations.

7.2 Limitations

The main limitations of the present research were the limited manufacturer test data available for modelling and validating the FEA tire model, the steady-state nature of

the simulations, and the limited number of factors studied for their effect on tire-rim slip. First, the FEA tire model was only validated based on a few simple tests such as the vertical stiffness and cornering force tests. There was no manufacturer data available for the tire deflections and forces at a wide range of operating conditions, such as different speeds and slip angles, other than the handful of curves shown in Chapter 3. In addition, there were no detailed material properties, or bead geometry information available to build into the model. Therefore, the simulation results provided mainly qualitative insights, as there was also no physical rim-slip test data available for quantitative comparison.

Second, fewer than 200 different combinations of operating conditions were simulated and provided as training and testing data for the neural network, due to the amount of time required to run each FEA simulation, especially the ones that included the SPH soil. This meant that a complete description of the operating condition parameter space was not possible, and could only be inferred from the limited regions for which simulations were done. Also, all of the simulations were performed under steady-state conditions, and transient effects were not considered. This restriction limits the trained virtual sensor to estimation rather than data-based prediction of rim-slip behavior under transient operating conditions.

Finally, there were a number of factors that were not considered in the simulations, such as the tire slip angle, thermal effects, road grade, longitudinal slip, and tire parameters. The limitation of the parameters studied was in some ways intentional, in order to have a manageable and useful set of results. Also, it is a common practice to limit the number of variables taken into account in standard tests. For example, according to the ASTM F2803 rim-slip test standard, the road grade should be less than 2% and the ambient temperature above 0°C, thus the effects of grade and temperature are not considered in this rim-slip test standard [55]. Additionally, in ASTM F2803 any longitudinal tire-road slip invalidates the test. A few of the simulations with high tire-rim friction, inflation pressure, vertical load, and drawbar load had longitudinal slip, but this was ignored, with only the slip between the tire

and rim being considered. All of these factors listed could be investigated in future work.

7.3 Future Work

There are multiple opportunities for future work based on the research in this thesis. First, the FEA tire model could be improved with a more detailed tire-rim contact region, and by using more advanced friction models which take into account the effects of sliding speed and temperature. This FEA model improvement could be done in parallel with physical rim-slip tests leading to quantitative comparisons. Second, the rim-slip database could be expanded by performing simulations for a larger number of different operating conditions and on additional terrains, such as a firmer soil or gravelly terrain. This would improve the knowledge of the combined effects of different operating conditions on tire-rim slip as well as provide more data for training the virtual sensor. Specific areas that could be studied are the real-world interaction effect of a simultaneous change in terrain and inflation pressure, or the complex interaction between tire temperature, tire-rim friction, and the heat generated by tire-rim slip. A final area of future work is developing and validating the prototype virtual sensor, by using physical tests to determine the type and number of sensors required to provide sufficient information for accurate tire-rim slip prediction under realistic operating conditions. Each of these areas of future work would further contribute to the tire-rim interaction knowledge base, the effects of different terrains and operating conditions on tire-rim slip, and the design and development of intelligent vehicle systems for managing tire-rim slip.

7.4 List of Publications

The following papers were published or produced during the course of this thesis:

W. Collings, Z. El-Sayegh, J. Ren, and M. El-Gindy, "Modelling of Off-Road Truck Tire-Rim Slip Using Finite Element Analysis," *SAE Int. J. Adv. & Curr. Prac. in Mobility*, vol. 4, no. 6, pp. 2335-2341, 2022, https://doi.org/10.4271/2022-01-0882.

W. Collings, Z. El-Sayegh, J. Ren, and M. El-Gindy, "Modelling of FEA Truck Tire-Rim Slip on SPH Sandy Loam," *Automotive Innovation*, 2023 (to be submitted).

W. Collings, Z. El-Sayegh, J. Ren, and M. El-Gindy, “Literature survey for the development of a virtual tire-rim slip sensor," *Int. J. Vehicle Systems Modelling and Testing*, 2023 (to be submitted).

Reference List

[1] F. Gheshlaghi, "Modeling and analysis of off-road tire cornering characteristics," MASc thesis, AMME Dept., FEAS, Ontario Tech Univ., Oshawa, Ontario, Canada, 2022.

[2] Z. El-Sayegh, "Modelling and analysis of truck tire-terrain interaction," Ph.D. dissertation, AMME Dept., FEAS, Ontario Tech Univ., Oshawa, Ontario, Canada, 2020.

[3] R. S. Dhillon, "Development of truck tire terrain finite element analysis models," MASc thesis, AMME Dept., FEAS, Ontario Tech Univ., Oshawa, Ontario, Canada, 2013.

[4] F. Farroni, N. Mancinelli, and F. Timpone, "A real-time thermal model for the analysis of tire/road interaction in motorcycle applications," *Applied Sciences*, vol. 10, no. 5, pp. 1604, Feb. 2020. [Online]. Available at: https://doi.org/10.3390/app10051604. Accessed on Apr. 22, 2023.

[5] R. Moisescu and G. Anghelache, "Study on the modal behaviour of contactless 11R22.5 truck tyre," in *IOP Conf. Series.: Material Sci. and Eng*., vol. 400, no. 4, 042040, presented at *ModTech Int. Conf. - Modern Technologies in Industrial Engineering VI*, Constanta, Romania, 2018. [Online]. Available: https://iopscience.iop.org/article/10.1088/1757-899X/400/4/042040. Accessed on Nov. 21, 2021.

[6] Y.T. Wei, E.C. Qiu, and L. Nasdala, "Analysis of tire shoulder endurance for a heavy-duty radial tire by FEA and material characterizations," in *Constitutive Models for Rubber IV*, P. E. Austrell, Ed. London, England: Routledge, 2005, pp. 576-570.

[7] C. Lee. "Rim slip and bead fitment of tires: analysis and design." *Tire Science and Technology*, vol. 34, no. 1, pp. 38-63, Jan. 2006. [Online]. Available: https://meridian.allenpress.com/tst/article-abstract/34/1/38/187037/Rim-Slip-and-Bead-Fitment-of-Tires-Analysis. Accessed on: May 10, 2021.

[8] S. Reina, "A study of layered contact problems with particular application to tyre-wheel interfaces," Ph. D. dissertation, Mech. Engineering Dept., Imperial College, London, UK, 2010.

[9] "Vibration Shortly After Tires are Mounted/Preventing Vibration from Wheel Slip (Tire Sliding on Wheel)," General Motors, 12-03-10-001B, 2014. [Online]. Available: https://static.nhtsa.gov/odi/tsbs/2014/MC-10137841-9999.pdf.

[10] "Consumer Complaints for Vibration - Tire/Rim Slip," Nitto Tire, Cypress, CA, NTSD-12-015, 2014. [Online]. Available: https://www.nittotire.com/media/55ibthri/techbulletin_ntsd_12-015-rev-3.pdf.

[11] J. Yunta, D. Garcia-Pozuelo, V. Diaz, and O. Olatunbosun, "A strain-based method to detect tires' loss of grip and estimate lateral friction coefficient from experimental data by fuzzy logic for intelligent tire development," *Sensors*, vol. 18, no. 2, pp. 490, Feb. 2018. [Online]. Available: https://doi.org/10.3390/s18020490. Accessed Mar. 3, 2021.

[12] K. B. Singh, M. A. Arat, and S. Taheri, "Literature review and fundamental approaches for vehicle and tire state estimation," *Vehicle System Dynamics*, vol. 57, no. 11, pp. 1643-1665, Nov. 2018. [Online]. Available: https://doi.org/10.1080/00423114.2018.1544373. Accessed on May 19, 2022.

[13] K. Nam, Y. Hori, and C. Lee, "Wheel slip control for improving traction-ability and energy efficiency of a personal electric vehicle," *Energies*, vol. 8, no. 7, pp. 6820-6840, July 2015. [Online]. Available: https://doi.org/10.3390/en8076820. Accessed on Apr. 23, 2021.

[14] Y.P. Chang, M. El-Gindy, and D. A. Streit, "Literature survey of transient dynamic response tyre models," *International Journal of Vehicle Design*, vol. 34, no. 4, pp. 354-386. 2004. [Online]. Available: https://www.inderscienceonline.com/doi/pdf/10.1504/IJVD.2004.004063.

[15] Y.-S. Wang, Z.-B. Cui, and J. Wu., "A review of the models for pneumatic tire stress analysis," unpublished. Available: https://www.researchgate.net/publication/295252501_A_REVIEW_OF_THE_MODELS_FOR_PNEUMATIC_TIRE_STRESS_ANSLYSIS.

[16] P.W.A. Zegelaar and H.B. Pacejka, "Dynamic tyre responses to brake torque variations," *Vehicle System Dynamics*, vol. 27, no. sup001, pp. 65-79, 1997. Available: https://doi.org/10.1080/00423119708969645.

[17] F. Orengo, M. H. Ray, and C. A. Plaxico, "Modelling tire blow-out in roadside hardware simulations using LS-DYNA," presented at *2003 ASME IMECE*. [Online]. Available: https://doi.org/10.1115/IMECE2003-55057.

[18] J. D. Reid, D. A. Boesch, and R. W. Bielenberg, "Detailed tire modeling for crash applications," *International Journal of Crashworthiness*, vol. 12, no. 5, pp. 521-529, Oct. 2007. [Online]. Available: https://doi.org/10.1080/13588260701483813.

[19] D. Barbani, M. Pierini, and N. Baldanzini, "FE modelling of a motorcycle tyre for full-scale crash simulations," *International Journal of Crashworthiness*, vol. 17, no. 3, pp. 309-318, Jun. 2012. [Online]. Available: https://doi.org/10.1080/13588265.2012.661212.

[20] Y. Cai, M. Zang, and F. Duan, "Modeling and simulation of vehicle responses to tire blowout," *Tire Science and Technology*, vol. 43, no. 3. pp. 242-258, Jul. 2015. [Online]. Available: https://doi.org/10.2346/tire.15.430301.

[21] S. Chae, “Nonlinear finite element modeling and analysis of a truck tire,” Ph.D. dissertation, Penn. State Univ., Pennsylvania, 2006.

[22] M. Selig, B. Lorenz, D. Henrichmöller, K. Schmidt, A. Ball, and B. N. J. Persson, ‘‘Rubber friction and tire dynamics: a comparison of theory with experimental data,’’ *Tire Science and Technology*, vol. 42, no. 4, pp. 216–262, Oct. 2014.

[23] K. Lardner, M. El-Gindy, F. Oijer, I. Johansson, and D. Philipps, "Determining the vertical and longitudinal first mode of vibration of a wide base FEA truck tire," SAE Technical Paper 2016-01-1308, 2016. [Online]. Available: https://doi.org/10.4271/2016-01-1308.

[24] A. A. Popov, and Z. Geng, “Modelling of vibration damping in pneumatic tyres,” *Vehicle System Dynamics*, vol. 43, supplement, pp. 145-155, Jan. 2005. [Online]. Available: https://doi.org/10.1080/00423110500140765.

[25] G. Previati, F. Ballo, M. Gobbi, and G. Mastinu, “Radial impact test of aluminium wheels—Numerical simulation and experimental validation,” *Int. J. of Impact Engineering*, vol. 126, pp. 117-134, Jan. 2019. [Online]. Available: https://www.sciencedirect.com/science/article/abs/pii/S0734743X18303907?via%3Dihub. Accessed on Oct. 23, 2020.

[26] L. Gagnon, M.J. Richard, P. Masarati, M. Morandini, and G. Doré, “An implicit ring tire model for multibody simulation with energy dissipation,” *Tire Science and Technology*, vol. 42, no. 2, p. 62-84, Apr. 2014. Available: https://doi.org/10.2346/tire.14.420203.

[27] J. Y. Wong, *Theory of Ground Vehicles*, 3rd ed. New York: John Wiley and Sons, 2001.

[28] M. Rafei, M. H. R. Ghoreishy, and G. Naderi, “Thermo-mechanical coupled finite element simulation of tire cornering characteristics—Effect of complex material models and friction law,” *Mathematics and Computers in Simulation*, vol. 144, pp. 35-51, Feb. 2018. [Online]. Available: https://www.sciencedirect.com/science/article/abs/pii/S0378475417302094?via%3Dihub. Accessed on May. 18, 2021.

[29] H. B. Pacejka, *Tyre and Vehicle Dynamics*, 1st ed. Oxford, UK: Butterworth-Heinemann, 2002.

[30] A. Brantin and O. Grunden, “Implementation of the rigid ring tyre model and accompanying soil model in a complete vehicle simulation tool for trucks,” MS thesis, Dept. of Applied Mechanics, Chalmers, Goteborg, Sweden, 2016.

[31] C. Wei and O. A. Olatunbosun, “The effects of tyre material and structure properties on relaxation length using finite element method,” *Materials & Design*, vol. 102, pp. 14-20, Jul. 2016. Available: https://doi.org/10.1016/j.matdes.2016.04.014.

[32] K. T. Danielson, A. K. Noor, J. S. Green, “Computational strategies for tire modeling and analysis,” *Computers & Structures*, vol. 61, no. 4, pp. 673-693, 1996.

[33] H. Zhou, G. Wang, Y. Ding, J. Yang, C. Liang, and J. Fu, "Effect of friction model and tire maneuvering on tire-pavement contact stress," *Advances in Materials Science and Engineering*, vol. 2015, Article ID 632647, 11 pages, Jun. 2015. [Online]. Available: https://doi.org/10.1155/2015/632647.

[34] C. Zhu, J. Yan, Y. Zhuang, et al., “A novel evaluation on rolling resistance characteristics of truck tire through the simplified experimental modal analysis,” *Proc. Inst. Mech. Eng. Part D: J. Automobile Engineering*, vol. 234, no. 12, pp. 2771-2782, Jul. 2020. Available: https://doi.org/10.1177/0954407020920032.

[35] A. A. Popov, D. J. Cole, C. B. Winkler, and D. Cebon, “Laboratory measurement of rolling resistance in truck tyres under dynamic vertical load,” *Proc. Inst. Mech. Eng. Part D: J. Automobile Engineering*, vol 217, no. 12, pp. 1071-1079, Dec. 2003. Available: https://journals.sagepub.com/doi/abs/10.1243/09544070360729419.

[36] A. C. Reid, “Development and optimization of a wide base FEA truck tire model for prediction of tire-road interactions,” MASc thesis, AMME Dept., FEAS, Ontario Tech University, Oshawa, Ontario, Canada, 2015.

[37] Z. El-Sayegh, M. El-Gindy, I. Johansson, and F. Öijer, “Off-road soft terrain modelling using smoothed particle hydrodynamics technique,” presented at the *ASME IDETC/CIE*, Quebec City, Canada, 2018.

[38] W. Smith, D. Melanz, C. Senatore, K. Iagnemma, and H. Peng, “Comparison of discrete element method and traditional modeling methods for steady-state wheel-terrain interaction of small vehicles,” *J. of Terramechanics*, vol. 56, pp. 61-75, Dec. 2014. [Online]. Available: https://www.sciencedirect.com/science/article/abs/pii/S0022489814000676. Accessed on April 11, 2022.

[39] M. H. R. Ghoreishy, M. Malekzadeh, and H. Rahimi, “A parametric study on the steady state rolling behaviour of a steel-belted radial tyre,” *Iranian Polymer Journal*, vol. 16, no. 8, pp. 539-548, Aug. 2007. Available: https://www.sid.ir/en/journal/ViewPaper.aspx?id=93304.

[40] H. Li and C. Schindler, “Analysis of soil compaction and tire mobility with finite element method,” *Proc. I. Mech. E. Part K: J. Multi-body Dynamics*, vol. 227, no. 3, pp. 275-291, May 2013. [Online]. Available: https://journals.sagepub.com/doi/10.1177/1464419313486627. Accessed on May 24, 2021.

[41] C.W. Fervers, “Improved FEM simulation model for tire-soil interaction,” *J. Terramechanics*, vol. 41, no. 2, pp. 87-100, Apr. 2004. [Online]. Available: https://doi.org/10.1016/j.jterra.2004.02.012. Accessed on Nov. 11, 2022.

[42] J. A. Sherwood, J. M. Ayres, T. S. Gross, and D. Watt, “An investigation of tire-wheel interface loads using ADINA,” *Computers and Structures*, vol. 56, No. 2/3, pp. 377-387, Jul. 1995. [Online]. Available: https://www.sciencedirect.com/science/article/abs/pii/004579499500030K.

[43] J. L. Slade, “Development of a new off-road rigid ring model for truck tires using finite element analysis techniques,” MS thesis, Dept. of Mech. Eng., Penn. State Univ., Pennsylvania, 2009.

[44] F. Gheshlaghi, Z. El-Sayegh, M. El-Gindy, F. Oijer, et al., “Advanced analytical truck tires-terrain interaction model,” SAE Technical Paper 2021-01-0329, 2021. [Online]. Available: https://doi.org/10.4271/2021-01-0329.

[45] F. Ballo, M. Gobbi, G. Mastinu, and G. Previati, "Motorcycle tire modeling for the study of tire–rim interaction," *ASME. J. Mechanical Design*, vol. 138, no. 5, article 0514041-13, May 2016. [Online]. Available: https://asmedigitalcollection.asme.org/mechanicaldesign/article-abstract/138/5/051404/473024/Motorcycle-Tire-Modeling-for-the-Study-of-Tire-Rim. Accessed on Oct. 23, 2020.

[46] X. Yan, “Non-linear three-dimensional finite element modeling of radial tires,” *Mathematics and Computers in Simulation*, vol. 58, no. 1, pp. 51-70, Dec. 2001. [Online]. Available: https://doi.org/10.1016/S0378-4754(01)00320-2.

[47] A. R. Johnson, J. A. Tanner, and A. J. Mason, “A kinematically driven anisotropic viscoelastic constitutive model applied to tires,” in *Workshop on Computational Modeling of Tires*, Virginia Consortium of Engineering and Science Universities, Hampton, Virginia, 1994, pp. 41-51.

[48] G. Anghelache and R. Moisescu, “Analysis of rubber elastic behaviour and its influence on modal properties,” *Materiale Plastice*, vol. 45, no. 2, pp. 143-148, Jun. 2008. Available: https://www.revmaterialeplastice.ro/pdf/ANGHELACHE%20G..pdf.

[49] Y.-P. Chang, “Nonlinear FEA rotating tire modeling for transient response simulations,” Ph.D. dissertation, Penn. State Univ., Pennsylvania, 2002.

[50] N. K. Jha, U. Nackenhorst, V. S. Pawar, R. Nadella, and P.J. Guruprasad, “On the constitutive modelling of fatigue damage in rubber-like materials,” *International Journal of Solids and Structures*, vol. 159, pp. 77-89, Mar. 2019. [Online]. Available: https://doi.org/10.1016/j.ijsolstr.2018.09.022.

[51] J. Stearns, “An investigation of stress and displacement distribution in a aluminum alloy automobile rim,” Ph.D. dissertation, University of Akron, Ohio, 2000.

[52] X. Wan, Y. Shan, X. Liu, T. He, et al., “Tire–rim interface pressure of a commercial vehicle wheel under radial loads: theory and experiment,” *Measurement Science*

and Technology, vol. 28, no. 11, pp. 5008-5017, 2017. [Online]. Available: https://doi.org/10.1088/1361-6501/aa8895.

[53] J. Muelaner. (2020, Apr. 30). *Finite Element Analysis of Pneumatic Tire Loading on Wheel*. [Online]. Available: https://www.engineersrule.com/finite-element-analysis-of-pneumatic-tire-loading-on-wheel/.

[54] S. Bishel, "Land vehicle tire qualification," U.S. Army DEVCOM Ground Vehicle Systems Center, Dec. 2019.

[55] *Standard Test Method for Evaluating Rim Slip Performance of Tires and Wheels*, ASTM F2803, 2015. Available: https://www.astm.org/f2803-21.html.

[56] A. R. Reece. "Problems of soil vehicle mechanics," U.S. Army Tank-Automotive Center, Warren, MI, Rep. no. 8470, Mar. 1964. [Online]. Available: https://apps.dtic.mil/sti/citations/AD0450151.

[57] J. A. Okello, "A Review of Soil Strength Measurement Techniques for Prediction of Terrain Vehicle Performance," *J. Agricultural Eng. Research*, vol. 50, pp. 129-155, Sept. 1991.

[58] USDA Soil Survey Division Staff, "Soil Texture Triangle," Public domain, via Wikimedia Commons [Online]. Available: https://commons.wikimedia.org/wiki/File:SoilTextureTriangle.jpg. Accessed on May. 7, 2023.

[59] H. Chuan, G. Feng, X. Xiaolin, Z. Wen, and J. Hui, "The sinkage characteristics and the supporting capacity of a submerged floating vehicle driving in deep soft terrains," *Proc. I. Mech. E. Part D: J. Automobile Engineering*, vol. 232, no. 6, pp. 725–737, May 2018. [Online]. Available: https://journals.sagepub.com/doi/10.1177/0954407017706843. Accessed on Jan. 16, 2021.

[60] Geoengineering Research Group, "Shear strength properties of a construction sand under different water contents," Carleton University, Ottawa, April 2019.

[61] F. Pollard and R. Webster, "The persistence of the effects of simulated tractor wheeling on sandy loam subsoil," *J. Agricultural Eng. Res.*, vol. 23, no. 2, pp. 217-220, June 1978. [Online]. Available: https://www.sciencedirect.com/science/article/abs/pii/0021863478900501. Accessed on: May, 12, 2021.

[62] B. D. Meek, E. R. Rachel, L. M. Carter, and W. R. DeTar, "Bulk density of a sandy loam soil: traffic, tillage, and irrigation-method effects," *Soil Science Soc. of America J.* vol. 56, no. 2, pp. 562-565, Mar. 1992.

[63] F. Pollard and J. G. Elliott, "The effect of soil compaction and method of fertilizer placement on the growth of barley using a concrete track technique," *J. Agric. Eng.*

Research, vol. 23, no. 2, pp. 203-216, June 1978. [Online]. Available: https://www.sciencedirect.com/science/article/abs/pii/0021863478900495. Accessed on May 12, 2021.

[64] American Society of Agricultural and Biological Engineers. (2009). Typical Soil Properties. [Online]. Available: https://elibrary.asabe.org/data/pdf/7/sd2009/chap3_cdfiles/Guidelines_for_spreadsheets.pdf. Accessed on May 12, 2021.

[65] M. G. Bekker et al., "Land locomotion research report no. 5," Detroit Arsenal, 1958.

[66] C. A. Coulomb, "Essai sur une application des regles des maximis et minimis a quelquels problemes de statique relatifs, a la architecture," *Mem. Acad. Roy. Div. Sav.*, vol. 7, pp. 343–387, 1776.

[67] M. G. Bekker, *Introduction to terrain-vehicle systems*, Ann Arbor, Michigan: University of Michigan Press, 1969.

[68] S. Shokouhfar, "A virtual test platform for analyses of rolling tyres on rigid and deformable terrains," Ph.D. dissertation, Mech. and Industrial Eng. Dept., Concordia University, Montreal, Quebec, Canada, 2017.

[69] R. Dhillon, M. El-Gindy, R. Ali, D. Philipps, F. Öijer, and I. Johansson, "Sensitivity analysis of smoothed particle hydrodynamics in PAM-CRASH for modeling of soft soils," presented at the *ASME IDETC/CIE*, Portland, Oregon, USA, 2013.

[70] P. Cundall and O. Strack, "A discrete numerical model for granular assemblies," *Géotechnique*, vol. 29, no. 1, pp. 47-65, Mar. 1979. [Online]. Available: https://doi.org/10.1680/geot.1979.29.1.47. Accessed on: Apr. 28, 2022.

[71] T. Tsuji, Y. Nakagawa, N. Matsumoto, Y. Kadono, T. Takayama, and T. Tanaka, "3-D DEM simulation of cohesive soil-pushing behavior by bulldozer blade," *J. of Terramechanics*, vol. 49, no. 1, pp. 37-47, Feb. 2012. [Online]. Available: https://www.sciencedirect.com/science/article/abs/pii/S0022489811001017. Accessed on May 13, 2022.

[72] Project Chrono. (2018). *Project Chrono: An Open Source Multi-physics Simulation Engine*. [Online]. Available: https://projectchrono.org/.

[73] D. Melanz, P. Jayakumar, and D. Negrut, "Experimental validation of a differential variational inequality-based approach for handling friction and contact in vehicle/granular-terrain interaction," *J. of Terramechanics*, vol. 65, pp. 1-13, June 2016. [Online]. Available: https://www.sciencedirect.com/science/article/abs/pii/S0022489816000069. Accessed on April 11, 2022.

[74] K. Iwashita and M. Oda, “Rolling resistance at contacts in simulation of shear band development by DEM,” *J. of Eng. Mechanics*, vol. 124, no. 3, pp. 285-292, Mar. 1998.

[75] D. Melanz, H. Mazhar, and D. Negrut, "A multibody dynamics-enabled mobility analysis tool for military applications," presented at *SAE WCX 2014*, SAE Technical Paper 2014-01-0873, 2014, https://doi.org/10.4271/2014-01-0873.

[76] J. B. Johnson, A. V. Kulchitsky, P. Duvoy, K. Iagnemma, C. Senatore, R. E. Arvidson, and J. Moore, “Discrete element method simulations of Mars Exploration Rover wheel performance,” *J. of Terramechanics*, vol. 62, pp. 31-40, Dec. 2015. [Online]. Available: https://www.sciencedirect.com/science/article/abs/pii/S0022489811000619. Accessed on: May 13, 2022.

[77] R. A. Gingold and J. J. Monaghan, “Smoothed particle hydrodynamics: theory and application to non-spherical stars,” *Monthly Notices of the Royal Astr. Society*, vol. 181, no. 3, pp. 275-389, Dec. 1977. [Online]. Available: https://academic.oup.com/mnras/article/181/3/375/988212?login=true. Accessed on May 17, 2022.

[78] J. J. Monaghan, “Smoothed particle hydrodynamics,” *Annual Review of Astronomy and Astrophysics*, vol. 30, pp. 543-574, 1992. [Online]. Available: https://articles.adsabs.harvard.edu/full/1992ARA%26A..30..543M/0000543.000.html. Accessed on May 17, 2022.

[79] M. B. Liu and G. R. Liu, “Smoothed particle hydrodynamics (SPH): an overview and recent developments,” *Archives of Computational Methods in Engineering*, vol. 17, pp. 25-76, Feb. 2010. [Online]. Available: https://link.springer.com/article/10.1007/S11831-010-9040-7. Accessed on May 17, 2022.

[80] ESI Group. (2014). Virtual Performance Solution 2014: Solver Reference Manual Vol. 3.

[81] R. Lescoe, “Improvement of soil modeling in a tire-soil interaction using finite element analysis and smooth particle hydrodynamics,” Master's thesis, Dept. of Mech. Eng., Penn. State Univ., Pennsylvania, 2010.

[82] Z. El-Sayegh, M. El-Gindy, I. Johansson, and F. Öijer, “Development of in-plane truck tire-flooded surface interaction models using FEA-SPH techniques,” presented at the *ASME IDETC/CIE*, Quebec City, Canada, 2018.

[83] K. B. Singh and M. A. Arat, “Deep learning in the automotive industry: recent advances and application examples,” *arXiv preprints*, arXiv:1906.08834, Jun. 2019. [Online]. Available: https://doi.org/10.48550/arXiv.1906.08834. Accessed on Jan. 25, 2021.

[84] X. Jin, G. Yin, and N. Chen, "Advanced estimation techniques for vehicle system dynamic state: A survey," *Sensors*, vol. 19, no. 19, pp. 4289, Oct. 2019. [Online]. Available: https://doi.org/10.3390/s19194289. Accessed on Mar. 31, 2021.

[85] Y. Jiang, S. Yin, J. Dong, and O. Kaynak, "A review on soft sensors for monitoring, control, and optimization of industrial processes," *IEEE Sensors Journal*, vol. 21, no. 11, pp. 12868-12881, Jun. 2021. [Online]. Available: https://ieeexplore.ieee.org/document/9235582. Accessed on May 19, 2022.

[86] H. Y. Guo, D. P. Cao, H. Chen, C. Lv., H. J. Wang, and S. Q. Yang, "Vehicle dynamic state estimation: state of the art schemes and perspectives," *IEEE/CAA J. of Automotive Sinica*, vol. 5, no. 2, pp. 418-431, Mar. 2018. [Online]. Available: https://ieeexplore.ieee.org/abstract/document/8283969.

[87] M. Acosta, S. Kanaracho, and M. Blundell, "Virtual tyre force sensors: An overview of tyre model-based and tyre model-less state estimation techniques," *Proc. of the Inst. of Mech. Eng. Part D: J. of Automobile Engineering*. Vol. 232, no. 14, pp. 1883-1930, Dec. 2018. [Online]. Available: https://doi.org/10.1177/0954407017728198. Accessed on Oct. 15, 2020.

[88] L. Fortuna, S. Graziani, A. Rizzo, M. G. Xibilia, *Soft Sensors for Monitoring and Control of Industrial Processes*, London: Springer, 2007.

[89] P. Kadlec, B. Gabrys, and S. Strandt, "Data-driven soft sensors in the process industry," *Computers and Chemical Engineering*, vol. 33, no. 4, pp. 795-814, Apr. 2009. [Online]. Available: https://doi.org/10.1016/j.compchemeng.2008.12.012. Accessed on May 25, 2022.

[90] J. A. Hamonangan, and S. T. Pinindriya, "A review of soft sensor methods for mach number measurement at LAPAN supersonic wind tunnel," in *SENTER*, Bandung, Indonesia, 2020, pp. 241-247. Available: https://www.academia.edu/46879503/A_Review_of_Soft_Sensor_Methods_for_Mach_number_Measurement_at_LAPAN_Supersonic_Wind_Tunnel?from=cover_page.

[91] R. Rajamani, D. Piyabongkarn, V. Tsourapas and J. Y. Lew, "Parameter and state estimation in vehicle roll dynamics," in *IEEE Transactions on Intelligent Transportation Systems*, vol. 12, no. 4, pp. 1558-1567, Dec. 2011. Available: https://doi.org/10.1109/TITS.2011.2164246.

[92] M. Ribeiro, and I. Ribeiro, "Kalman and extended Kalman filters: concept, derivation and properties," 2004. [Online]. Available: https://www.researchgate.net/publication/2888846_Kalman_and_Extended_Kalman_Filters_Concept_Derivation_and_Properties. Accessed on Aug. 25, 2022.

[93] S. K. Spurgeon, "Sliding mode observers: a survey," *Int. J. of Systems Science*, vol. 39, no. 8, pp. 751-764, May 2008. [Online]. Available:

https://www.tandfonline.com/doi/abs/10.1080/00207720701847638. Accessed on Oct. 21, 2022.

[94] H. F. Grip, L. Imsland, T. A. Johansen, J. C. Kalkkuhl and A. Suissa, "Vehicle sideslip estimation," *IEEE Control Systems Magazine*, vol. 29, no. 5, pp. 36-52, Oct. 2009. Available: https://doi.org/10.1109/MCS.2009.934083.

[95] E.D. Sontag, "Input to state stability: basic concepts and results," in *Nonlinear and Optimal Control Theory*. *Lecture Notes in Mathematics*, vol 1932, P. Nistri & G. Stefani, Eds. Springer, Berlin, Heidelberg, 2008. https://doi.org/10.1007/978-3-540-77653-6_3.

[96] Lyapunov, A. M. *The general problem of the stability of motion*, trans. A. T. Fuller, Taylor & Francis, London, 1992.

[97] Y. Engel, S. Mannor and R. Meir, "The kernel recursive least-squares algorithm," *IEEE Transactions on Signal Processing*, vol. 52, no. 8, pp. 2275-2285, Aug. 2004. Available: https://doi.org/10.1109/TSP.2004.830985.

[98] S. Z. Zhang, Y. H. Wu and J. Chang, "Design of tire damage image recognition system based on deep learning," *J. Physics: Conf. Series*, vol. 1631, no. 012015, 2020. Available: https://doi.org/10.1088/1742-6596/1631/1/012015.

[99] A. Graves, A. Mohamed and G. Hinton, "Speech recognition with deep recurrent neural networks," in *2013 IEEE International Conference on Acoustics, Speech and Signal Processing*, Vancouver, BC, Canada, 2013, pp. 6645-6649. Available: https://doi.org/10.1109/ICASSP.2013.6638947.

[100] W. S. McCulloch and W. Pitts, "A logical calculus of the ideas immanent in nervous activity," Bulletin of Mathematical Biophysics, vol. 5, no. 4, pp. 115-133, Dec. 1943.

[101] J. Schmidhuber. "Deep learning in neural networks: an overview." *Neural Networks*, vol. 61, pp. 85-117, Jan. 2015. [Online]. Available: https://www.sciencedirect.com/science/article/abs/pii/S0893608014002135?via%3Dihub. Accessed on: Feb., 17, 2021.

[102] P. Kerlirzin and F. Vallet, "Robustness in multilayer perceptrons," *Neural Computation*, vol. 5, no. 3, pp. 473–482, May 1993. Available: https://doi.org/10.1162/neco.1993.5.3.473.

[103] J. Alexandersson and E. S. Lonegren, "Neural networks for modelling of a virtual sensor in an engine," Master's thesis, Electrical Engineering, Chalmers University, Gothenburg, Sweden, 2019.

[104] J. Ghosh, A. Tonoli, and N. Amati, "A deep learning based virtual sensor for vehicle sideslip angle estimation: experimental results," SAE Technical Paper 2018-01-1089, 2018, https://doi.org/10.4271/2018-01-1089.

[105] J. Svendenius, “Tire modelling and friction estimation,” Ph.D. dissertation, Dept. of Automatic Control, Lund Inst. of Tech., Lund University, Lund, Sweden, 2007.

[106] Goodyear Europe. *Truck Tire Technical Data Book*. Colmar-Berg, Luxembourg. [Online]. Available: www.eu.goodyear.com.

[107] W. Collings, Z. El-Sayegh, J. Ren, and M. El-Gindy, "Modelling of off-road truck tire-rim slip using finite element analysis," *SAE Int. J. Adv. & Curr. Prac. in Mobility*, vol. 4, no. 6, pp. 2335-2341, 2022. Available: https://doi.org/10.4271/2022-01-0882.

[108] COMSOL. (2019). Hyperelastic Material Models. [Online]. Available: https://doc.comsol.com/5.5/doc/com.comsol.help.sme/sme_ug_theory.06.28.html.

[109] K. L. Lardner, "Prediction of the off-road rigid-ring model parameters for truck tire and soft soil interactions," MASc thesis, AMME Dept., FEAS, Ontario Tech Univ., Oshawa, Ontario, Canada, 2017.

[110] ESI Group. (2014). Virtual Performance Solution 2014: Solver Reference Manual Vol. 2.

[111] G. Heinrich and M. Klüppel, “Rubber friction, tread deformation and tire traction,” *Wear*, vol. 265, pp. 1052-1060, April. 2008. [Online]. Available: https://www.sciencedirect.com/science/article/abs/pii/S0043164808000847. Accessed on: May 15, 2021.

[112] Taylor Dynamometer. (2019). *RS-40K Towing Dynamometer*. Milwaukee, Wisconsin. [Online]. Available: https://www.taylordyno.com/wp-content/uploads/pdfs/SMS4011-RS-40K.pdf.

[113] M. J. Stallmann, P. S. Els, and C. M. Bekker, "Parameterization and modelling of large off-road tyres for ride analyses: Part 1 – Obtaining parameterization data," *J. Terramechanics*, vol. 55, pp. 73-84, Oct. 2014. [Online]. Available: https://www.sciencedirect.com/science/article/abs/pii/S0022489814000378. Accessed Nov. 24, 2022.

[114] C. Yu, C. Loureiro, J.-J. Cheng, L.G. Jones, Y. Y. Wang, Y. P. Chia, and E. Faillace, *Data collection handbook to support modeling the impacts of radioactive material in soil*. Argonne National Laboratory, Environmental Assessment and Information Sciences Division. Argonne, Illinois, 1993. Available: https://www.osti.gov/biblio/10162250-8viMWW/.

[115] W. Collings, Z. El-Sayegh, J. Ren, and M. El-Gindy, "Modelling of FEA truck tire-rim slip on SPH sandy loam," presented at the *ISTVS Americas Symposium*, Oct. 5-7, 2022, Montréal, Québec, Canada.

[116] E. M. DuPont, C. A. Moore, M. F. Selekwa, R. G. Roberts and E. G. Collins, “Online terrain classification for mobile robots,” *Proceedings of the ASME 2005*

International Mechanical Engineering Congress and Exposition. *Dynamic Systems and Control, Parts A and B*. Orlando, Florida, USA. Nov. 5–11, 2005. pp. 1643-1648. Available: https://doi.org/10.1115/IMECE2005-81659.

[117] Z. Ziaukas, A. Busch, M. Weilitzka, T. Ortmaier, and J.-P. Kobler, "Classification of tire pressure in a semitrailer using a convolutional neural network," in *IEEE Int. Conf. on Mechatronics and Automation*, Beijing, China, pp.181-185, 2020.

[118] M. H. Beale, M. T. Hagan, and H. B. Demuth. (2020). *Deep Learning Toolbox™ Getting Started Guide*. The MathWorks, Inc. Natick, MA. [Online]. Available: https://www.mathworks.com/help/releases/R2020a/pdf_doc/deeplearning/nnet_gs.pdf.

[119] MathWorks. (2020). *R2020a Documentation – initnw function*. The MathWorks, Inc. Natick, MA. [Online]. Available: https://www.mathworks.com/help/releases/R2020a/deeplearning/ref/initnw.html.

[120] D. Nguyen and B. Widrow, "Improving the learning speed of 2-layer neural networks by choosing initial values of the adaptive weights," *1990 IJCNN International Joint Conference on Neural Networks*, San Diego, CA, USA, 1990, vol.3, pp. 21-26. Available: https://doi.org/10.1109/IJCNN.1990.137819.

[121] K. Levenberg, "A method for the solution of certain non-linear problems in least squares," *Quarterly of applied mathematics* vol. 2, no. 2, pp. 164-168, 1944. Available: https://www.ams.org/journals/qam/1944-02-02/S0033-569X-1944-10666-0/S0033-569X-1944-10666-0.pdf.

[122] D. W. Marquardt, "An algorithm for least-squares estimation of nonlinear parameters," *J. Soc. Indust. Appl. Math*, vol. 11, no. 2, pp. 431-441, June 1963. Available: https://doi.org/10.1137/0111030.

[123] A. Ranganathan, "The Levenberg-Marquardt Algorithm," Jun. 2004, lecture note for CS290I Multiple View Geometry in Computer Vision and Computer Graphics, Dr. Y-F. Wang, Spring 2012, Computer Science Department, UCSB. Available: https://sites.cs.ucsb.edu/~yfwang/courses/cs290i_mvg/pdf/LMA.pdf. Accessed on May 8, 2023.

[124] M. H. Beale, M. T. Hagan, and H. B. Demuth. (2020). *Deep Learning Toolbox™ User's Guide*. The MathWorks, Inc. Natick, MA. [Online]. Available: https://www.mathworks.com/help/releases/R2020a/pdf_doc/deeplearning/nnet_ug.pdf.

[125] F. Dan Foresee and M. T. Hagan, "Gauss-Newton approximation to Bayesian learning," *1997 IJCNN International Conference on Neural Networks*, Houston, TX, USA, 1997, vol. 3, pp. 1930-1935, Available: https://doi.org/10.1109/ICNN.1997.614194.

[126] D. MacKay, “Bayesian interpolation,” *Neural Computation*, vol. 4, no. 3, pp. 415–447, May 1992. [Online]. Available: https://doi.org/10.1162/neco.1992.4.3.415.

[127] MathWorks. (2020). *R2020a Documentation – tansig function.* The MathWorks, Inc. Natick, MA. [Online]. Available: https://www.mathworks.com/help/releases/R2020a/deeplearning/ref/tansig.html.

Appendices

Appendix A. Rim-Slip Simulation Data

Note: Rim-slip data in grayed-out rows was either a duplicated condition, an outlier, or part of the speed variation tests, and was not included in the training dataset for the neural network in Chapter 6. All of the longitudinal wheel speed (V_x) values were also removed from the training dataset, but are included here for completeness.

Table A1: Rim-slip simulation data for parameter variation on a hard surface

Terrain	F_z	p_{inf}	V_x	F_D	μ	i_{rim}
none	kN	kPa	km/h	%	none	%
1	40.034	379.2	10	30	0.05	100.028
1	40.034	379.2	10	30	0.1	2.357
1	40.034	379.2	10	30	0.2	0.612
1	40.034	379.2	10	30	0.3	0.484
1	40.034	379.2	10	30	0.5	0.237
1	40.034	379.2	10	30	0.7	0.032
1	40.034	379.2	10	30	0.9	-0.024
1	40.034	379.2	10	40	0.05	100.175
1	40.034	379.2	10	40	0.1	99.973
1	40.034	379.2	10	40	0.2	0.723
1	40.034	379.2	10	40	0.3	0.529
1	40.034	379.2	10	40	0.5	0.340
1	40.034	379.2	10	40	0.7	0.136
1	40.034	379.2	10	40	0.9	0.010
1	40.034	379.2	10	60	0.05	100.113
1	40.034	379.2	10	60	0.1	100.066
1	40.034	379.2	10	60	0.2	1.670
1	40.034	379.2	10	60	0.3	0.746
1	40.034	379.2	10	60	0.5	0.456
1	40.034	379.2	10	60	0.7	0.251
1	40.034	379.2	10	60	0.9	0.039
1	40.034	379.2	10	90	0.05	100.208
1	40.034	379.2	10	90	0.1	100.028
1	40.034	379.2	10	90	0.2	100.082
1	40.034	379.2	10	90	0.3	9.692
1	40.034	379.2	10	90	0.5	1.341
1	40.034	379.2	10	90	0.7	0.780
1	40.034	379.2	10	90	0.9	0.561
1	13.345	275.8	10	90	0.2	0.454

Terrain	F_z	p_{inf}	V_x	F_D	μ	i_{rim}
none	kN	kPa	km/h	%	none	%
1	13.345	379.2	10	90	0.2	0.268
1	13.345	482.6	10	90	0.2	0.128
1	13.345	586.1	10	90	0.2	0.103
1	13.345	758.4	10	90	0.2	0.051
1	13.345	896.3	10	90	0.2	0.022
1	26.689	275.8	10	90	0.2	99.887
1	26.689	379.2	10	90	0.2	96.937
1	26.689	482.6	10	90	0.2	0.707
1	26.689	586.1	10	90	0.2	0.509
1	26.689	758.4	10	90	0.2	0.255
1	26.689	896.3	10	90	0.2	0.156
1	40.034	275.8	10	90	0.2	100.102
1	40.034	379.2	10	90	0.2	100.129
1	40.034	482.6	10	90	0.2	100.141
1	40.034	586.1	10	90	0.2	1.480
1	40.034	758.4	10	90	0.2	0.728
1	40.034	896.3	10	90	0.2	0.489
1	40.034	379.2	5	40	0.2	0.571
1	40.034	379.2	10	40	0.2	0.798
1	40.034	379.2	20	40	0.2	0.768
1	40.034	379.2	40	40	0.2	0.748
1	40.034	379.2	60	40	0.2	0.708
1	40.034	379.2	5	60	0.2	2.296
1	40.034	379.2	10	60	0.2	1.581
1	40.034	379.2	20	60	0.2	1.674
1	40.034	379.2	40	60	0.2	1.737
1	40.034	379.2	60	60	0.2	10.196
1	40.034	379.2	70	60	0.2	1.478
1	40.034	379.2	5	90	0.2	99.730
1	40.034	379.2	10	90	0.2	100.107
1	40.034	379.2	20	90	0.2	99.998
1	40.034	379.2	40	90	0.2	99.223
1	40.034	379.2	60	90	0.2	99.910

Table A2: Rim-slip simulation data for parameter variation on soil

Terrain	F_z	p_{inf}	V_x	F_D	μ	i_{rim}
none	kN	kPa	km/h	%	none	%
2	40.034	379.2	10	20	0.05	99.965
2	40.034	379.2	10	20	0.1	100.028
2	40.034	379.2	10	20	0.2	0.778
2	40.034	379.2	10	20	0.3	0.570
2	40.034	379.2	10	20	0.5	0.263
2	40.034	379.2	10	20	0.7	0.085
2	40.034	379.2	10	30	0.05	99.963
2	40.034	379.2	10	30	0.1	99.988
2	40.034	379.2	10	30	0.2	0.926
2	40.034	379.2	10	30	0.3	0.670
2	40.034	379.2	10	30	0.5	0.316
2	40.034	379.2	10	30	0.7	0.110
2	40.034	379.2	10	30	0.9	0.053
2	40.034	379.2	10	40	0.05	99.974
2	40.034	379.2	10	40	0.1	100.063
2	40.034	379.2	10	40	0.2	99.245
2	40.034	379.2	10	40	0.3	0.755
2	40.034	379.2	10	40	0.5	0.360
2	40.034	379.2	10	40	0.7	0.112
2	40.034	379.2	10	60	0.05	99.971
2	40.034	379.2	10	60	0.1	100.012
2	40.034	379.2	10	60	0.2	99.518
2	40.034	379.2	10	60	0.3	1.101
2	40.034	379.2	10	60	0.5	0.537
2	40.034	379.2	10	60	0.7	0.212
2	40.034	379.2	10	60	0.9	0.083
2	40.034	379.2	10	90	0.05	99.971
2	40.034	379.2	10	90	0.1	100.073
2	40.034	379.2	10	90	0.2	99.483
2	40.034	379.2	10	90	0.3	96.662
2	40.034	379.2	10	90	0.5	0.818
2	40.034	379.2	10	90	0.7	0.489
2	40.034	379.2	10	90	0.9	0.171
2	13.345	275.8	10	60	0.2	0.379
2	13.345	379.2	10	60	0.2	0.193
2	13.345	482.6	10	60	0.2	0.104
2	13.345	586.1	10	60	0.2	0.057
2	13.345	758.4	10	60	0.2	0.029
2	26.689	275.8	10	60	0.2	99.487

Terrain	F_z	p_{inf}	V_x	F_D	μ	i_{rim}
none	kN	kPa	km/h	%	none	%
2	26.689	379.2	10	60	0.2	1.905
2	26.689	482.6	10	60	0.2	0.574
2	26.689	586.1	10	60	0.2	0.381
2	26.689	758.4	10	60	0.2	0.214
2	40.034	275.8	10	60	0.2	99.461
2	40.034	379.2	10	60	0.2	99.851
2	40.034	482.6	10	60	0.2	99.552
2	40.034	586.1	10	60	0.2	1.339
2	40.034	758.4	10	60	0.2	0.588
2	40.034	379.2	5	20	0.2	0.629
2	40.034	379.2	10	20	0.2	0.778
2	40.034	379.2	20	20	0.2	0.737
2	40.034	379.2	40	20	0.2	0.717
2	40.034	379.2	60	20	0.2	0.911
2	40.034	379.2	5	40	0.2	92.173
2	40.034	379.2	10	40	0.2	99.245
2	40.034	379.2	20	40	0.2	98.905
2	40.034	379.2	40	40	0.2	98.265
2	40.034	379.2	60	40	0.2	32.999
2	40.034	379.2	5	60	0.2	94.941
2	40.034	379.2	10	60	0.2	99.518
2	40.034	379.2	20	60	0.2	99.239
2	40.034	379.2	40	60	0.2	100.328
2	40.034	379.2	60	60	0.2	98.509

Table A3: Rim-slip simulation data for additional training simulations

Terrain	F_z	p_{inf}	V_x	F_D	μ	i_{rim}
none	kN	kPa	km/h	%	none	%
1	13.345	379.2	10	30	0.05	0.482
1	13.345	482.6	10	30	0.05	0.305
1	13.345	586.1	10	30	0.05	0.206
1	13.345	758.4	10	30	0.05	0.191
1	13.345	896.3	10	30	0.05	0.175
1	26.689	379.2	10	30	0.05	99.285
1	26.689	482.6	10	30	0.05	96.837
1	26.689	586.1	10	30	0.05	0.763
1	26.689	758.4	10	30	0.05	0.356
1	26.689	896.3	10	30	0.05	0.358
1	13.345	379.2	10	60	0.05	99.487
1	13.345	482.6	10	60	0.05	98.823
1	13.345	586.1	10	60	0.05	2.148
1	13.345	758.4	10	60	0.05	0.301
1	13.345	896.3	10	60	0.05	0.267
1	26.689	379.2	10	60	0.05	99.680
1	26.689	482.6	10	60	0.05	99.593
1	26.689	586.1	10	60	0.05	99.587
1	26.689	758.4	10	60	0.05	99.575
1	26.689	896.3	10	60	0.05	99.204
1	13.345	379.2	10	30	0.9	0.059
1	13.345	482.6	10	30	0.9	0.081
1	13.345	586.1	10	30	0.9	0.120
1	13.345	758.4	10	30	0.9	0.134
1	13.345	896.3	10	30	0.9	0.128
1	26.689	379.2	10	30	0.9	0.071
1	26.689	482.6	10	30	0.9	0.112
1	26.689	586.1	10	30	0.9	0.112
1	26.689	758.4	10	30	0.9	0.134
1	26.689	896.3	10	30	0.9	0.140
1	13.345	379.2	10	60	0.9	0.057
1	13.345	482.6	10	60	0.9	0.083
1	13.345	586.1	10	60	0.9	0.122
1	13.345	758.4	10	60	0.9	0.134
1	13.345	896.3	10	60	0.9	0.128
1	26.689	379.2	10	60	0.9	0.061
1	26.689	482.6	10	60	0.9	0.108
1	26.689	586.1	10	60	0.9	0.112
1	26.689	758.4	10	60	0.9	0.134

Terrain	F_z	p_{inf}	V_x	F_D	μ	i_{rim}
none	kN	kPa	km/h	%	none	%
1	26.689	896.3	10	60	0.9	0.140
2	13.345	275.8	10	30	0.05	101.120
2	13.345	379.2	10	30	0.05	99.393
2	13.345	482.6	10	30	0.05	29.093
2	13.345	586.1	10	30	0.05	0.346
2	13.345	758.4	10	30	0.05	0.299
2	26.689	275.8	10	30	0.05	99.925
2	26.689	379.2	10	30	0.05	99.957
2	26.689	482.6	10	30	0.05	100.006
2	26.689	586.1	10	30	0.05	100.106
2	26.689	758.4	10	30	0.05	99.605
2	13.345	275.8	10	90	0.05	100.932
2	13.345	379.2	10	90	0.05	99.646
2	13.345	482.6	10	90	0.05	99.644
2	13.345	586.1	10	90	0.05	99.619
2	13.345	758.4	10	90	0.05	99.611
2	26.689	275.8	10	90	0.05	99.951
2	26.689	379.2	10	90	0.05	99.996
2	26.689	482.6	10	90	0.05	99.969
2	26.689	586.1	10	90	0.05	100.006
2	26.689	758.4	10	90	0.05	99.656
2	13.345	275.8	10	30	0.9	0.018
2	13.345	379.2	10	30	0.9	0.049
2	13.345	482.6	10	30	0.9	0.051
2	13.345	586.1	10	30	0.9	0.067
2	13.345	758.4	10	30	0.9	0.124
2	26.689	275.8	10	30	0.9	0.010
2	26.689	379.2	10	30	0.9	0.073
2	26.689	482.6	10	30	0.9	0.077
2	26.689	586.1	10	30	0.9	0.098
2	26.689	758.4	10	30	0.9	0.120
2	13.345	275.8	10	90	0.9	0.028
2	13.345	379.2	10	90	0.9	0.049
2	13.345	482.6	10	90	0.9	0.031
2	13.345	586.1	10	90	0.9	0.073
2	13.345	758.4	10	90	0.9	0.124
2	26.689	275.8	10	90	0.9	0.041
2	26.689	379.2	10	90	0.9	0.102
2	26.689	482.6	10	90	0.9	0.079
2	26.689	586.1	10	90	0.9	0.092
2	26.689	758.4	10	90	0.9	0.114

Table A4: Rim-slip simulation data for additional testing simulations

Terrain	F_z	p_{inf}	V_x	F_D	μ	i_{rim}
none	kN	kPa	km/h	% Fz	none	%
1	13.345	482.6	10	50	0.2	0.122
1	17.793	379.2	10	90	0.1	99.597
1	26.689	758.4	10	30	0.4	0.071
1	40.034	586.1	10	20	0.7	0.067
1	44.482	896.3	10	70	0.5	0.083
1	13.345	275.8	10	60	0.9	0.059
1	17.793	427.5	10	40	0.05	98.280
1	26.689	689.5	10	30	0.5	0.067
1	40.034	379.2	10	90	0.4	3.035
1	44.482	586.1	10	70	0.2	0.963
2	13.345	896.3	10	60	0.9	0.128
2	17.793	482.6	10	30	0.7	0.010
2	26.689	427.5	10	90	0.4	0.271
2	40.034	379.2	10	50	0.1	99.969
2	44.482	482.6	10	40	0.3	0.625
2	13.345	275.8	10	20	0.5	0.020
2	17.793	758.4	10	70	0.05	99.607
2	26.689	275.8	10	20	0.9	0.016
2	40.034	586.1	10	50	0.2	0.715
2	44.482	689.5	10	60	0.7	0.067

Appendix B. Neural Network Weights and Equations

Figure 6.1 is repeated in Figure B1 below, showing the neurons in each of the layers of the neural network, with the connections to their corresponding weights and biases and the inputs and output of the network.

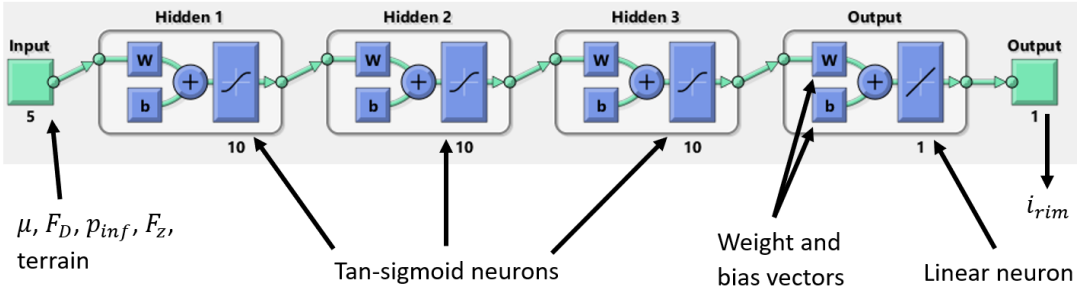

Figure B1: Schematic of final neural network from Chapter 6 with 3 hidden layers of 10 neurons each.

The numerical input m to the activation function of each neuron is calculated from the connected inputs x_i, weights w_i, and bias b of each neuron according to the summation equation Eq. B.1.

$$m = \sum_{i=1}^{n} w_i x_i + b \tag{B.1}$$

Two different activation functions were use for the shallow neural network, the $tansig$ function for the hidden layer neurons, and the $purelin$ function for the output layer neuron [118]. The $tansig$ function is mathematically equivalent to $tanh$, while the $purelin$ function is simply a line with a slope of 1 [124], [127]. These activation functions are shown in Eqs. B.2 and B.3. Successively feeding the 5 input parameters through the summation and activation equations of each layer of neurons allowed the predicted rim-slip value to be calculated. The weights and biases for each neuron in the best network from Chapter 6 are listed in Tables B1-B4.

$$tansig(m) = \tanh(m) = \frac{2}{1 + e^{-2m}} - 1 \tag{B.2}$$

$$purelin(m) = m \tag{B.3}$$

Table B1: Weights and biases for hidden layer 1

	Inputs					
Layer 1 Neuron #	Terrain	F_z	p_{inf}	μ	F_D	Bias
1	-0.31771	-0.591217	-0.00627	1.6597793	-1.10087	1.054726
2	0.120123	0.07625302	-1.10935	-1.258429	0.043363	-1.4752
3	0.567278	0.1487318	-0.51799	0.221818	-0.03959	-0.02897
4	0.02004	-0.1888479	0.26209	0.6593239	0.099175	0.510629
5	0.289167	0.7808803	-1.11243	1.0257865	0.724116	0.709954
6	-0.14827	-0.311537	-0.0179	0.7318435	-0.51851	0.444917
7	0.245262	-0.1934494	-0.20108	-0.223884	-0.60165	0.003082
8	0.303193	-0.1088238	-0.22722	0.3119034	0.60357	-0.56026
9	0.599609	-1.0691198	0.144107	0.6870788	0.243662	0.659351
10	0.387339	-0.4571513	-0.30761	-1.271264	0.506168	-0.29238

Table B2: Weights and biases for hidden layer 2

	Layer 1 Neuron #					
Layer 2 Neuron #	1	2	3	4	5	6
1	0.099515	-0.4916782	0.042616	-0.039445	0.216044	0.021558
2	0.310075	0.29403046	-0.08103	0.3908034	0.317628	0.020406
3	0.420766	-0.7029302	0.301754	0.1075578	0.175413	-0.10935
4	-0.35392	0.29294837	0.225468	-0.328556	-0.33527	0.041815
5	-0.8049	1.15022832	-0.06646	0.1666243	-0.62394	-0.24379
6	0.139765	-0.278762	0.083633	-0.135688	0.033128	0.128928
7	0.648296	-0.5966041	0.14789	0.303058	0.373987	0.333298
8	0.20714	-0.3119082	0.047159	0.0852476	-0.14823	0.197203
9	0.204617	0.08834717	0.213917	0.3921755	-0.10471	0.526238
10	-1.7707	1.64073131	0.235678	-0.690861	-1.66573	-0.83132
	Layer 1 Neuron #					
Layer 2 Neuron #	7	8	9	10	Bias	
1	-0.00972	-0.1749549	0.379144	-0.132716	0.414147	
2	0.154967	-0.1639551	0.265439	-0.306382	0.025875	
3	-0.02246	-0.303634	0.441102	-0.189808	0.194159	
4	0.323531	-0.0950348	0.151106	0.4340127	0.011352	
5	0.192139	-0.2475682	-0.37595	0.7508335	-0.53255	
6	-0.32085	-0.1020461	0.091119	0.0952869	0.049131	
7	0.231422	-0.1956909	0.202037	-0.279714	-0.12698	
8	0.184284	-0.1095142	-0.05976	-0.154048	0.104379	
9	-0.05205	-0.399173	0.091539	-0.160352	-0.0295	
10	0.261668	0.31583268	-1.15954	1.0737092	-0.66434	

Table B3: Weights and biases for hidden layer 3

	Layer 2 Neuron #					
Layer 3 Neuron #	1	2	3	4	5	6
1	0.235813	0.21553623	0.499113	-0.630938	0.44007	0.152088
2	0.105371	-0.0630751	-0.03922	-0.031968	0.030935	-0.04871
3	0.145658	-0.1743063	0.098021	0.2567869	-0.61491	0.1251
4	-0.29105	0.13875424	0.217289	0.142859	-0.04718	0.239732
5	0.090446	-0.0553251	-0.03115	-0.025067	0.021717	-0.03786
6	-0.26488	0.17831311	0.146776	0.0724304	-0.10343	0.144948
7	-0.03377	0.01961024	0.010016	0.0107748	-0.00692	0.013474
8	-0.46843	-0.4109013	-0.69517	0.4175108	1.239878	-0.13821
9	-0.14626	0.09314755	0.058074	0.0356908	-0.04364	0.065744
10	-0.11046	0.06850512	0.040001	0.0290889	-0.02874	0.047339
	Layer 2 Neuron #					
Layer 3 Neuron #	7	8	9	10	Bias	
1	0.68599	-0.0658008	-0.0894	-1.066429	0.17378	
2	0.043144	-0.0576229	0.082202	-0.093193	0.002672	
3	0.121338	0.01726829	0.400012	-0.352933	0.039986	
4	-0.12213	0.33389765	-0.19729	0.3129641	0.118011	
5	0.035841	-0.0465844	0.070748	-0.068018	0.00372	
6	-0.08165	0.17810914	-0.20385	0.1725057	0.012989	
7	-0.01443	0.01663943	-0.02621	0.0272948	-0.00184	
8	-0.80971	-0.031208	-0.27357	3.0542462	-0.26981	
9	-0.05343	0.07955061	-0.11458	0.1048248	-0.00269	
10	-0.04257	0.05791648	-0.08649	0.0816781	-0.00375	

Table B4: Weights and biases for output layer

	Layer 3 Neuron #					
	1	2	3	4	5	6
Output neuron	1.375287	-0.2067795	-0.62357	0.6975864	-0.16823	0.528041
	Layer 3 Neuron #					
	7	8	9	10	Bias	
Output neuron	0.062473	1.47867444	0.276522	0.2065161	-0.0385	